Forschungsbericht 2026-24

Experimental Study of Dusty Flow – Surface Interactions on Heat-Shield Materials at Martian Atmospheric Entry Conditions

Ciro Salvi

Deutsches Zentrum für Luft- und Raumfahrt
Institut für Aerodynamik und Strömungstechnik
Abteilung Über- und Hyperschalltechnologien
Köln

DLR Deutsches Zentrum für Luft- und Raumfahrt

Experimental Study of Dusty Flow–Surface Interactions on Heat-Shield Materials at Martian Atmospheric Entry Conditions

Experimentelle Untersuchung von Partikel-Strömungs-Oberflächen-Wechselwirkungen an Hitzeschutzmaterialien für Eintrittsbedingungen in der Marsatmosphäre

Von der Fakultät für Maschinenwesen
der Rheinisch-Westfälischen Technischen Hochschule Aachen
zur Erlangung des akademischen Grades eines Doktors der Ingenieurwissenschaften
genehmigte Dissertation

vorgelegt von

Ciro Salvi

Berichter: Univ.-Prof. Isaac Boxx, PhD
Hon.-Prof. Dr.-Ing. Ali Gülhan

Tag der mündlichen Prüfung: 21.07.2026

Diese Dissertation ist auf den Internetseiten der Universitätsbibliothek online verfügbar.

Forschungsbericht 2026-24

Experimental Study of Dusty Flow – Surface Interactions on Heat-Shield Materials at Martian Atmospheric Entry Conditions

Ciro Salvi

Deutsches Zentrum für Luft- und Raumfahrt
Institut für Aerodynamik und Strömungstechnik
Abteilung Über- und Hyperschalltechnologien
Köln

132 Seiten
53 Bilder
10 Tabellen
130 Literaturstellen

Deutsches Zentrum
DLR für Luft- und Raumfahrt

Herausgeber:

Deutsches Zentrum
für Luft- und Raumfahrt e. V.
Wissenschaftliche Information
Linder Höhe
D-51147 Köln

ISSN 1434-8454
ISRN DLR-FB-2026-24
Erscheinungsjahr 2026
DOI: 10.57676/5ndv-4t78

Erklärung des Herausgebers
Dieses Werk – ausgenommen anderweitig gekennzeichneter Teile – ist lizensiert unter den Bedingungen der Creative Commons Lizenz vom Typ Namensnennung 4.0 International (CC BY 4.0), abrufbar über https://creativecommons.org/licenses/by/4.0/legalcode

Lizenz



Creative Commons Attribution 4.0 International

Atmosphärischer Eintritt, Mars, Hyperschallströmung, Hochenthalpieströmung, Lichtbogenbeheizter Windkanal, Staubbeladene Strömung, Partikel, Korkablator, P50, Berührungslose Diagnostik, PIV, TDLAS, DLAS, LPT, SEM, EDX

Ciro SALVI
DLR, Institut für Aerodynamik und Strömungstechnik, Köln

Experimentelle Untersuchung von Partikel-Strömungs-Oberflächen-Wechselwirkungen an Hitzeschutzmaterialien für Eintrittsbedingungen in der Marsatmosphäre
RWTH Aachen Universität

Diese Arbeit präsentiert eine experimentelle Methodik zur Charakterisierung partikelbeladener Hochenthalpieströmungen und zur Untersuchung des Materialverhaltens bei Bedingungen, die den Eintritt in die Marsatmosphäre während Staubstürmen repräsentieren. Bei Experimenten im lichtbogenbeheizten Windkanal L2K des DLR wurden mikrometergroße MgO-Partikel in einer CO_2/N_2-Strömung verwendet, um staubige Eintrittsumgebungen nachzubilden. Diagnostikverfahren wie PIV, TDLAS und SEM/EDX, unterstützt durch CFD-Simulationen, ermöglichten die Charakterisierung der Partikeldynamik und der Zwei-Phasen-Strömungsphänomene, um zentrale Effekte wie Geschwindigkeitsverzug und Partikelagglomeration zu identifizieren.

Bei Materialtests an korkbasierten Ablatoren wurden Infrarot-Thermografie, eingebettete Thermoelemente, Röntgenbilder und in-situ Laser-Sheet-Profilverfolgung (LPT) genutzt, um partikelbedingte Effekte wie verstärkte Oberflächenabtragung, erhöhten Wärmetransfer und transiente, emissionsgradbedingte Messartefakte zu zeigen. Ein eindimensionales datenbasiertes Modell wurde entwickelt, um die Änderung der Dicke unter Berücksichtigung von Aufquellen, Abtragung und Erosion vorherzusagen, was die experimentellen Daten erfolgreich reproduziert. Diese Studie zeigt die Machbarkeit der Nachbildung und Quantifizierung komplexer Partikel–Material-Wechselwirkungen in Testanlagen und liefert wertvolle Erkenntnisse für das Design und die Qualifikation von Hitzeschutzsystemen für zukünftige Marsmissionen.

Hypersonic, High Enthalpy, Arc-Heated Wind Tunnel, Re-entry, Mars, Dust, Particles, Cork, P50, Non-Intrusive, Velocimetry, PIV, TDLAS, DLAS, LPT, SEM, EDX

(Published in English)

Ciro SALVI
German Aerospace Center (DLR), Institute of Aerodynamics and Flow Technologies, Cologne

Experimental Study of Dusty Flow--Surface Interactions on Heat-Shield Materials at Martian Atmospheric Entry Conditions
RWTH Aachen University

This work presents an experimental methodology for the characterization of particle-laden high-enthalpy flows and the investigation of material behaviour under conditions representing entry into the Martian atmosphere during dust storms. Experiments in the DLR L2K arc-heated wind tunnel used micrometric MgO particles in CO_2/N_2 flow to replicate dusty entry environments. Diagnostics including PIV, TDLAS, and SEM/EDX characterised particle dynamics and two-phase flow features, supported by CFD simulations identifying key phenomena such as velocity lag and particle agglomeration.

Material response tests on cork-based ablators employed infrared thermography, embedded thermocouples, X-ray imaging, and in-situ laser-sheet profile tracking (LPT), revealing particle-induced effects like enhanced surface recession, increased heat transfer, and transient emissivity artefacts. A one-dimensional model was developed to predict thickness evolution accounting for swelling, ablation, and erosion, successfully reproducing experimental data. The study demonstrates the feasibility of replicating and quantifying complex particle–material interactions in ground facilities, providing valuable insight for future Martian TPS design and qualification.

Abstract

This work presents an experimental methodology for the characterization of particle-laden high-enthalpy flows and the investigation of material behaviour under conditions representing entry into the Martian atmosphere during dust storms. Experiments in the DLR L2K arc-heated wind tunnel used micrometric MgO particles in CO_2/N_2 flow to replicate dusty entry environments. Diagnostics including PIV, TDLAS, and SEM/EDX characterised particle dynamics and two-phase flow features, supported by CFD simulations identifying key phenomena such as velocity lag and particle agglomeration.

Material response tests on cork-based ablators employed infrared thermography, embedded thermocouples, X-ray imaging, and in-situ laser-sheet profile tracking (LPT), revealing particle-induced effects like enhanced surface recession, increased heat transfer, and transient emissivity artefacts. A one-dimensional model was developed to predict thickness evolution accounting for swelling, ablation, and erosion, successfully reproducing experimental data. The study demonstrates the feasibility of replicating and quantifying complex particle–material interactions in ground facilities, providing valuable insight for future Martian TPS design and qualification.

Zusammenfassung

Diese Arbeit präsentiert eine experimentelle Methodik zur Charakterisierung partikelbeladener Hochenthalpieströmungen und zur Untersuchung des Materialverhaltens bei Bedingungen, die den Eintritt in die Marsatmosphäre während Staubstürmen repräsentieren. Bei Experimenten im lichtbogenbeheizten Windkanal L2K des DLR wurden mikrometergroße MgO-Partikel in einer CO_2/N_2-Strömung verwendet, um staubige Eintrittsumgebungen nachzubilden. Diagnostikverfahren wie PIV, TDLAS und SEM/EDX, unterstützt durch CFD-Simulationen, ermöglichten die Charakterisierung der Partikeldynamik und der Zwei-Phasen-Strömungsphänomene, um zentrale Effekte wie Geschwindigkeitsverzug und Partikelagglomeration zu identifizieren.

Bei Materialtests an korkbasierten Ablatoren wurden Infrarot-Thermografie, eingebettete Thermoelemente, Röntgenbilder und in-situ Laser-Sheet-Profilverfolgung (LPT) genutzt, um partikelbedingte Effekte wie verstärkte Oberflächenabtragung, erhöhten Wärmetransfer und transiente, emissionsgradbedingte Messartefakte zu zeigen. Ein eindimensionales datenbasiertes Modell wurde entwickelt, um die Änderung der Dicke unter Berücksichtigung von Aufquellen, Abtragung und Erosion vorherzusagen, was die experimentellen Daten erfolgreich reproduziert. Diese Studie zeigt die Machbarkeit der Nachbildung und Quantifizierung komplexer Partikel–Material-Wechselwirkungen in Testanlagen und liefert wertvolle Erkenntnisse für das Design und die Qualifikation von Hitzeschutzsystemen für zukünftige Marsmissionen.

"That's a good question"

on its own

is a pretty bad answer.

Preface

This doctoral thesis was written in Cologne at the Department of Supersonic and Hypersonic Technologies of the German Aerospace Center (DLR) between 2023 and 2026. The work was conducted under the supervision of Professor Isaac Boxx (*RWTH Aachen University*) and Professor Ali Gülhan (*DLR, RWTH Aachen University*). It addresses atmospheric entry on Mars, including conditions during global dust storms, with a focus on hypersonic aerothermodynamics and multiphase high-enthalpy flows interacting with ablative materials.

Atmospheric entry in the Martian environment constitutes a uniquely challenging regime. The simultaneous presence of rarefied hypersonic flow, suspended solid particles, extreme thermal loads, and ablating surfaces gives rise to complex physical interactions that remain only partially understood. While significant advances have been achieved in theoretical modelling and numerical simulation, the lack of experimental data under relevant conditions has long limited model validation and physical interpretation. Prior to this work, no ground-based facility worldwide was capable of reproducing, in a controlled manner, the coupled flow conditions encountered during Martian atmospheric entry.

This thesis presents an experimental study aimed at addressing this limitation. Its primary objective is the development of a dedicated test setup capable of simulating Martian-entry-relevant multiphase high-enthalpy flows on ground. In addition, the work provides experimental data and physical interpretation intended to support predictive modelling efforts in this field. The work presented in this thesis is based on original experimental research conducted at the DLR in Cologne.

Whether read on a monitor or held in hand, it is my hope that this thesis provides not only answers, but also perspective. More importantly, I hope that the work presented here stimulates new questions, encourages further investigation, and contributes, in a small but meaningful way, to our understanding of planetary atmospheric entry.

Acknowledgements

This thesis marks the conclusion of a wonderful three-year journey, a chapter of my life shaped by many people who contributed both to what I have achieved and to who I have become. *Thank you all. Grazie. Vielen Dank!*

This work would not have been possible without the invaluable supervision of Professor Isaac Boxx, whose scientific insight, comments, and reviews have been fundamental throughout this journey. The same heartfelt gratitude goes to Professor Ali Gülhan, who welcomed me into the department right after my master's graduation and continuously guided, supervised, and supported my work with all the necessary resources. I am deeply thankful to Professor Filippo Maggi, without whom I would not be here today, and to the scientists from NASA Ames, whose inspiring discussions enriched my experience and helped keep my motivation high: *to the stars*.

I am grateful to the DLR, a place that supports both personal and professional growth, providing all the resources needed for research while offering a peaceful setting in the midst of the forest. From my office, I could watch birds in the trees or spot hares in the undergrowth. The forest marks the passing of the seasons: summer with its hidden mushrooms, autumn when deer blend into the fallen leaves, winter and its silent blanket of snow, and spring with the first newborn foxes. This natural rhythm created a unique environment for focus, reflection, and inspiration throughout my doctoral work.

Special thanks to Marcus, for sweetening my working days with figs from his trees. To Matthias, for always being there, at work and under a climbing wall. To Dominik S., For All Ridiculous Times. To Ansgar, Pawel, and Patrick, best reviewers, game-night companions, and coffee enthusiasts. To Oliver H., Oliver G., and Alex, the best managers and executors of L2K activities. And to Dominik N., Pascal, Dirk, Lars, Viktor, Marco, Dr. Esser, and Thorn, for your constant support on endless fronts.

Thanks to Papà and Mamma, for always keeping a door open, a warm bed ready, and a table set, making me feel at home no matter how far I travel, and for your support through every step of this journey.

To Erika, for our true love unbroken by distance. You have been my constant Sun in these rainy German lands, always understanding, supportive, and patient, even though the choice to pursue this PhD kept us far apart. Your strength and encouragement made it possible for me to focus, grow, and realise my dreams while knowing our bond remains unshaken.

To Leo and Luli, for the quiet strength, and constant love of brotherhood that have anchored me through both challenges and celebrations.

To Pizzo, for our everlasting Lazzaro spirit, and your rabious *"there's no fish in Germany"* still echoing in my head.

To Lucia and the extended family, our circle of intertwined differences, shared exchange, and growth.

To Bonni, for our shared adventures, endless laughter, and the reminder in your motto *"adelante"* that we must always move forward, no matter what.

To my old friends, Didi, Lore, Spino, Fede, Ila, Mattia, Fabio, and Urbi, who remind me that true friendship endures no matter the distance.

To Beriedir, my band and all its members, still welcoming the noisiest of us all.

To Zia Adri and Zia Beba, for your love, support, and the ways you have shaped who I am today.

To the Apnea Academy family, and especially to Tova, for the fun, the challenges, the lessons learnt, and the goals we reached together. Thank you for inspiring me both in sport and in life.

Thanks to my new friends Male, Anju, Raj, and the entire Tutti and Spieleabend crews, for the warmth and laughter, that have made this new chapter feel like home.

To Tom, for your enthusiasm, your unwavering kindness, and the lightness you bring to every situation, no matter how hard.

To my Mitbewohner Monika and Tibi, for our shared home, the dinners together, and the quiet support during the most stressful days.

Thanks to the Mountains and the Sea, gentle giants with whom I feel a profound bond. They have taught me that *with humility, awareness, and attentive listening, one can reach the highest peaks, dive into the deepest oceans, and traverse the sharpest ridges.* Their solemn presence carries lessons of patience, endurance, and respect, and in their vastness, I have found both inspiration and a mirror for the inner journey.

And after all, thanks to Ryanair.

Moving abroad inevitably brought moments of sadness, for me, and for those who may have felt left behind. Yet we all grew by learning to understand and accept each other's choices. For that, I thank you: for keeping faith in our relationships and never letting go. In the end, the inner peace takes a different form for each of us. Inner peace means finding an identity, a purpose, a dream, and persevering in it. It is not easy. *I wish you, and I wish myself, the strength to always understand and accept your loved ones*, who, sometimes in silence, may still be searching for calm amidst their own storms.

Dedicato a tutti quelli che stanno scappando.
– Mediterraneo

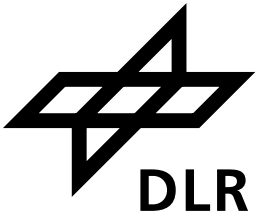
DLR

Contents

List of Figures ix

List of Tables xiii

Nomenclature xv
Abbreviations . . . xv
Latin Symbols . . . xvi
Greek Symbols . . . xvii
Subscripts and Superscripts . . . xviii

1 Introduction 1
1.1 Objectives and Research Questions . . . 3
1.2 Published Content . . . 4

2 Fundamentals and State of the Art 7
2.1 Physical Processes during Martian Entry . . . 7
2.1.1 Fundamentals of Two-Phase High-Enthalpy Flows . . . 8
2.1.2 Governing Parameters of Particle–Flow Interactions . . . 10
2.1.3 Thermal Protection Systems . . . 14
2.1.4 Ablative Materials . . . 14
2.1.5 Erosion Rate Modelling . . . 16
2.2 State of the Art . . . 17

3 Experimental Setup 25
3.1 L2K Wind Tunnel . . . 25
3.2 P50 Cork Samples . . . 27
3.3 Relevant Experimental Techniques . . . 30
3.3.1 Tunable Diode Laser Absorption Spectroscopy (TDLAS) . . . 30
3.3.2 Particle Image Velocimetry (PIV) . . . 32
3.3.3 Particle Count vs Erosion Rate . . . 44
3.3.4 Particle Collection . . . 46
3.3.5 Overall Thickness Evolution Measurements . . . 47
3.3.6 Laser-sheet Profile Tracking (LPT) . . . 48
3.3.7 Temperature Measurements . . . 51
3.3.8 X-rays . . . 51
3.3.9 Qualitative Observations . . . 52

3.4 CFD Setup . . . 53

4 Flow and Particle Characterisation 57
4.1 Particle Velocity in the Free-Stream . . . 57
4.1.1 Agglomeration Due to Melting (Agglo-Melting) . . . 62
4.1.2 Difference in Flow Properties for Different Flow Conditions . . . 65
4.1.3 Spatial Resolution . . . 66
4.1.4 Gravity Effect . . . 66
4.1.5 Change of Flow Features due to Injection . . . 67
4.2 Particle Velocity Across the Shock Layer . . . 68
4.3 CFD Results . . . 71
4.4 Particle Collection . . . 75
4.5 Summary and Future Steps . . . 78

5 Sample Behaviour 81
5.1 Qualitative Analysis . . . 81
5.2 Sample Temperatures . . . 86
5.2.1 Surface Temperature . . . 86
5.2.2 In-Depth Temperature . . . 91
5.3 Thickness Evolution Measurements . . . 94
5.4 Summary and Future Steps . . . 99

6 Data-Based Thickness Evolution Model 103
6.1 Mathematical Model . . . 103
6.2 Model Discussion . . . 107
6.3 Data Fit . . . 109
6.4 Summary and Future Steps . . . 113

7 Conclusions and Outlook 117

8 Bibliography 121

List of Figures

1.1 The L2K arc-heated wind tunnel with open test section 2

2.1 Different regimes characterising gas–particle interactions, in high Reynolds-number flows, in the continuum regime, from [21] 9
2.2 Drag coefficient C_D of a sphere, from [21] 13
2.3 Particle-laden flow test with sample in the L2K 19
2.4 Typical cork-based ablator evolution process, from [9] 22

3.1 L2K nozzle geometry, 200 mm exit diameter configuration. Sizes in mm . 26
3.2 Sample geometry and its cross section, highlighting the shallower thermocouple. The bottom thinner side is used to position the thermocouples, and to connect to the cooled support of the L2K 28
3.3 Sample before testing. The flow will come from the left 29
3.4 TDLAS setup and results, from [110] 31
3.5 Experimental setup for free-stream studies, FS. The reported axes originate on the flow axis, at the nozzle exit location. In practice, both the seeding generator and the sCMOS camera are positioned in the xz-plane 33
3.6 Experimental setup for shock-layer studies, SL. The reported axes originate on the flow axis, at the nozzle exit location. In practice, both the seeding generator and the sCMOS camera are positioned in the xz-plane 34
3.7 Randomly selected PIV frame (number 985) from FS1, FCI^P 38
3.8 Flow field features 39
3.9 Wind tunnel test frame from video monitoring (FS setup) 42
3.10 Generic PIV raw images of the two setups, showing first frame (left) and second frame (right). The flow comes from the left, as highlighted by the green arrow 43
3.11 Magnesium oxide particles before testing 47
3.12 Raw images at two different time instants, $t_0 = 0\,\mathrm{s}$ (left) and $t_{end} = 60\,\mathrm{s}$ (right): one can appreciate the evolution of the reflected laser profile . . . 48
3.13 Mid-plane profile evolution, colour-ordered over time. The two pictures present the same data, one with equal axes aspect ratio (left), and one with stretched x to better appreciate the profile evolution 50
3.14 X-rays of the sample before (above) and after (below) the test 52
3.15 Grids used for CFD computations (only nodes are displayed) 54

4.1 Free-stream PIV in FCI^P, (tests FS1, FS2) 58

4.2 Free-stream PIV in FCII^P, (tests FS1, FS2) . . . 58
4.3 Mean particles' velocity profiles along transversal direction, compared with flow velocities from CFD results (DLR-TAU flow solver) and TDLAS. CFD transversal profiles are reported only for $x = 50$ mm and $x = 100$ mm for visualisation ease. *In the legend, " * " refers to the axial position $x = 100$ mm, where the TDLAS velocity measurements were performed* . 59
4.4 Standard deviation σ_v, (test FS1) . . . 60
4.5 Mean velocity and standard deviation profiles along the transversal direction, averaged the along x-axis . . . 61
4.6 Averaged correlation maps of FCI^P (left) and FCII^P (right), at the position (x,y) = (0,40) mm . . . 63
4.7 Mean velocity of test *"Ex1-P1"*, from EMAP [100]. The nozzle flow is from bottom to top . . . 64
4.8 Stagnation point measurements at $x = 100$ mm . . . 67
4.9 SL-PIV result. The white region on the right is the cork sample. The flow comes from the left . . . 68
4.10 Velocity profiles . . . 69
4.11 Relative fluctuations . . . 70
4.12 Free-stream CFD results . . . 72
4.13 Shock-layer CFD results . . . 73
4.14 Numerical simulations with DLR-TAU flow solver. Note that the two sub-figures have differently scaled colour-bars . . . 74
4.15 Effects of particles and material response on shock stand-off distance δ . 75
4.16 SEM image of collected particles in FCI^P . . . 76
4.17 SEM image of collected particles in FCII^P . . . 77

5.1 Samples during testing in different flow conditions . . . 82
5.2 Sample surface after testing . . . 83
5.3 Samples' axial-symmetric sections. Pictures are translated vertically to match the location of the virgin material . . . 85
5.4 X-Rays of tested samples. Noise is marked in red, black and grey regions are virgin and non-virgin material respectively. The two pictures are translated vertically to match the location of the virgin material . . . 86
5.5 IR data . . . 87
5.6 Surface temperature measurements in FCI^{nP} and FCII^{nP}: one- and two-colour pyrometers (1cP, 2cP) and infrared camera (IR) . . . 88
5.7 Surface temperature measurements in FCI^P and FCII^P: one- and two-colour pyrometers (1cP, 2cP) and infrared camera (IR; the dotted lines represent peculiar spots in the IR camera frames that highlight an erosion event) . . . 89

5.8 In-depth temperature increase at the shallower thermocouple for all 10 tested probes. The thermocouple depth x_{TC} is measured with X-rays. Thermocouples whose depth differ more than 0.5 mm should not be compared 92
5.9 Final in-depth temperature increase at the shallower thermocouple for all 10 tested probes. The thermocouple depth x_{TC} is measured with X-rays. Thermocouples whose depth differ more than 0.5 mm should not be compared 93
5.10 Sample overall evolution from 3D surface scans 95
5.11 Time-resolved thickness evolution measurement (y/t space) 97
5.12 Time-resolved thickness evolution measurement in its central region, $|y| <$ 10 mm, (E/t space) 98

6.1 1D surface evolution model 104
6.2 Qualitative model response, influenced by the parameters a, b, and k, and depending on the presence of particles 108
6.3 Results at lower enthalpy, FCI$^{P/nP}$: blue colours indicate conditions without particles and red colours indicate conditions with particles. The particles counted within the light sheet are presented in green, through raw data, Gaussian-smoothed results, and burst regions 110
6.4 Results at higher enthalpy, FCII$^{P/nP}$: blue colours indicate conditions without particles and red colours indicate conditions with particles. The particles counted within the light sheet are presented in green, through raw data, Gaussian-smoothed results, and burst regions 111

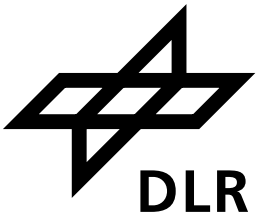
DLR

List of Tables

1.1 Published articles in first-quartile peer-reviewed journals 5
1.2 Conference and workshop items 5
1.3 Patent application 5

2.1 Flow regime classification by particle Knudsen number [84] 11

3.1 Flow conditions FCs. The superscripts ^{P} and ^{nP} indicate the FCs with and without particles respectively. The mass flow rates are equal for all FCs 26
3.2 Test parameters for different flow conditions 28
3.3 Test matrix 36

4.1 Relative uncertainty on the average velocity 60
4.2 Free-stream values computed with quasi-1D flow solver NATA [8] 65

6.1 Fitted model parameters for FCs^{nP} 109

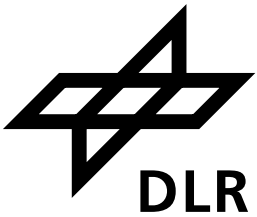
DLR

Nomenclature

Abbreviations

1D	one-dimensional
1cP	one-colour pyrometer
2C	two components
2D	bi-dimensional
2cP	two-colour pyrometer
3D	tri-dimensional
BP	bypass
CFD	computational fluid dynamics
DIC	digital image correlation
DLR	German Aerospace Center
EDL	entry, descent and landing
EDX	energy-dispersive X-ray spectroscopy
ESA	European Space Agency
EUCASS	European Conference for Aerospace Sciences
FC	flow condition
FS	free-stream
FTIR	Fourier transform infrared spectroscopy
FWHM	full-width at half-maximum
GBK	multiple-phase flow facility
IPPW	International Planetary Probe Workshop
IR	infrared
IVP	initial value problem
IW	interrogation window
L2F	laser-to-focus
L2K	arc-heated wind tunnel 2 Köln
LBK	arc-heated wind tunnel facility Köln
LDM	long-distance microscope
LIF	laser-induced fluorescence
LPT	laser-sheet profile tracking
MSL	Mars Science Laboratory
NASA	National Aeronautics and Space Administration
NaN	not-a-number

Nd:YAG	neodymium-doped yttrium aluminium garnet
ODE	ordinary differential equation
PDPA	phase-doppler particle analyser
PIV	particle image velocimetry
PTU	programmable timing unit
PTV	particle tracking velocimetry
RoI	region of interest
SEM	scanning electron microscope
SL	shock-layer
SNR	signal-to-noise ratio
TDLAS	tunable diode laser absorption spectroscopy
TPS	thermal protection systems
WS	workshop
sCMOS	scientific complementary metal–oxide–semiconductor

Latin Symbols

A	proportionality factor
a	recession rate
A_p	cross-sectional area
b	swelling coefficient
C	Cunningham correction factor
c	generic model coefficient
C_D	drag coefficient
c_p	specific heat capacity
d_p	particle diameter
E	thickness evolution
$\mathbf{F}$	force
$f_{/\#}$	f number
f	focal length
H	sample height with respect to a common reference surface
h	convective heat coefficient
$\bar{h}$	convolution kernel
H_v	material hardness
k	system stiffness
k_g	gas thermal conductivity
Kn_p	Knudsen number
M	magnification
Δm	mass loss

m_p	single particle mass
Ma_p	relative Mach number
N	number of valid samples
NA	numerical aperture
N_p	cumulative particle number
n_p	particle count
Nu	Nusselt number
p	(static) pressure
P_r	sample profile
q	heat transfer
R	gas constant
Re	Reynolds number
Re_p	particle Reynolds number
s	integration variable
St	Stokes number
T	(static) temperature
t	time
u_v	relative uncertainty
$\mathbf{v}_g$	gas velocity
$\mathbf{v}_p$	particle velocity
$\mathbf{v}_{slip}$	slip velocity
x	x-coordinate
x_{TC}	thermocouple depth
Y	surface position
y	y-coordinate
z	z-coordinate

Greek Symbols

α	angle of attack
γ	isentropic exponent
δ	shock stand-off distance
ε	emissivity
λ	wavelength
λ_g	mean free path
μ_g	dynamic viscosity
ν	frequency
ρ	density
ρ_g	gas density

ρ_p	particle density
σ_v	standard deviation of velocity
σ	standard deviation
σ_B	Stefan-Boltzmann constant
τ	integration variable
τ_g	gas characteristic time
τ_p	particle characteristic time
ϕ_v	particle volume fraction

Subscripts and Superscripts

$_0$	initial conditions
$_{end}$	final moment
$_{eq}$	equilibrium
$_m$	melting point
^{BP}	bypass flow
$_e$	erosion
$_{hot}$	heated flow
^{P}	with particles
^{nP}	without particles
$_r$	recession
$_s$	swelling

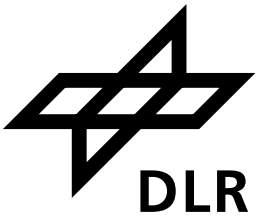
DLR

1 Introduction

Since the 1960s, Mars has been the target of several scientific missions: five successful flybys, eighteen orbiters, seven landers, six rovers, and one rotorcraft, have studied the atmosphere, the weather, the geology and morphology of the Red Planet until today [126]. Space agencies and private companies are increasingly investing in the idea that the first generation of interplanetary astronauts could soon be ready to set foot on the red dust of our rocky neighbour. When that moment comes, they may well echo the iconic words: *"that's one small step for man, one giant leap for mankind"*. Nearly six decades have passed since those words were first spoken, and perhaps only a few more remain until they are heard again.

A typical mission profile to Mars consists of several phases: launching from Earth, departure from its sphere of influence, interplanetary cruise, arrival within Mars' sphere of influence, orbital insertion around the Red Planet, and finally atmospheric entry and landing. The entry, descent and landing (EDL) modules need to reduce their velocity from several km/s to a few m/s, to safely land on the surface without crashing. Part of the speed reduction is typically attributed to thrusters, and another considerable fraction is provided by the atmosphere, that slows the EDL modules with drag. On the one hand, the presence of an atmosphere reduces mission costs associated with propellant and propulsion: manoeuvres such as aerocapture and aerobraking of the EDL module exploit atmospheric drag to decelerate the spacecraft (exploiting its blunt shape and parachute deployment), thereby lowering propellant requirements. On the other hand, atmospheric entry is a challenging manoeuvre, occurring in the hypersonic regime and involving high-temperature effects that necessitate the use of external thermal protection systems (TPS) to ensure spacecraft survivability. The presence of an atmosphere adds further mission complexity, as the descent and landing are strongly influenced by the vehicle's aerodynamic and flight-dynamic behaviour.

The complexity of entering Martian atmosphere is also given by the presence of suspended dust particles, which can vary depending on Martian weather [84]. In recent years, several major dust storms were observed, with dust reaching altitudes up to 80 km—relevant for atmospheric entry. Experiments have shown that the presence of particles during entry can significantly increase thermal loads on spacecraft TPS [53]. However, large uncertainties remain in predicting particle-enhanced heat flux and material response. In recent years, particle-laden high-enthalpy flows have attracted renewed scientific interest [85], leading to a collaboration between the German Aerospace Center (DLR) and the Ames Research Center of the National Aeronautics and Space Administration (NASA).

This joint effort aims to advance the modelling and simulation of dusty entry flows, through targeted experimental campaigns, ultimately improving numerical reconstruction and validation of two-phase high-enthalpy supersonic flows.

Experimental campaigns in long-duration high-enthalpy facilities provide both physical insight into extreme flow phenomena and validation for numerical models. On-ground simulations of Martian entry are essential for the optimisation of spacecraft heat shields, aimed at increasing reliability, minimising mass, thus reducing overall mission costs and increasing payloads. Yet, achieving these goals demands improvements in the operational modes and diagnostic capabilities of existing wind tunnels—an effort to which this work is dedicated. In particular, the present study employs an arc-heated wind tunnel, selected for its long test durations, flexible operating conditions, and ability to investigate both the thermal and mechanical response of TPS and the underlying physical mechanisms of high-enthalpy, particle-laden flows, features that are difficult to achieve in other types of hypersonic wind tunnels. Previous dusty-flow experiments at DLR were carried out in the supersonic multiple-phase flow facility (GBK) and in the arc-heated wind tunnel 2 Köln (L2K) [53], part of the arc-heated wind tunnel facility Köln (LBK) at the Supersonic and Hypersonic Technologies Department in Cologne. Building on this heritage, the present work focuses on upgrading the diagnostic capabilities of the L2K wind tunnel, whose open test section is shown in figure 1.1.

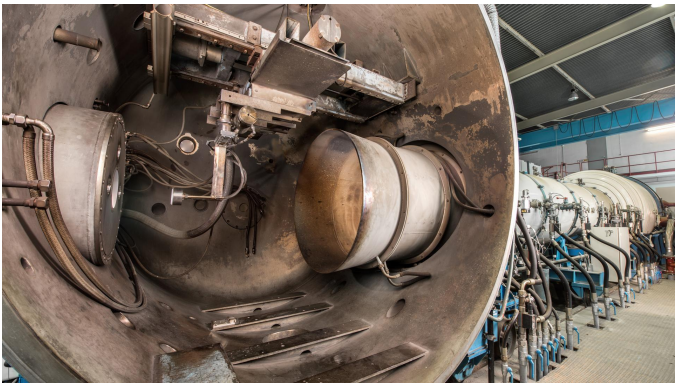

Figure 1.1: The L2K arc-heated wind tunnel with open test section

Four representative flow conditions, derived by DLR from post-flight data analysis of ExoMars 2016 [41], were selected for investigation, considering particle-laden flows in a Mars-like atmosphere (97% CO_2 and 3% N_2), suitable for material testing over several minutes. In this study, micrometric MgO particles were used as dust analogues.

1.1 Objectives and Research Questions

The primary objective of this research is to develop an experimental framework capable of precisely characterising both the particle-laden flow within the wind tunnel, and the material behaviour under Mars-entry conditions. This objective is divided into two *sub-goals*:

- The **characterisation of the particle-laden flow conditions**, by means of flow and particle velocity measurements, and by particle collection.
- The **analysis of material response** within those previously characterised conditions, through the development of an innovative technique for in-situ thickness evolution (or recession) measurements.

This effort ultimately led to the creation of a mathematical model enabling convenient prediction of material behaviour, based on experimental evidence.

Accordingly, the research questions underlying this thesis span several interconnected topics, including particle dynamics in dust-laden high-enthalpy flows (*dusty flows*), material response under dust-laden high-enthalpy conditions (*flow–surface interactions*), and the associated experimental challenges, all within the context of *Martian atmospheric entry*. This scope is reflected in the thesis title: "**Experimental Study of Dusty Flow–Surface Interactions on Heat-Shield Materials at Martian Atmospheric Entry Conditions**", which is guided by the following broad research questions:

(i) How can existing high-enthalpy wind tunnels be enhanced to meet the growing demand for increased accuracy in Martian atmospheric entry studies?

(ii) What are the characteristic flow–surface interaction phenomena in dust-laden high-enthalpy wind tunnels, and how do they influence material behaviour?

(iii) Can experimentally obtained correlations between particle flux and surface recession be used to develop a predictive, data-based model for material behaviour under Martian atmospheric entry conditions?

According to the stated objectives, research questions, and contents, this work is organised into seven chapters:

1. **Introduction**—the current chapter, which defines the objectives and presents the published content upon which the manuscript is based.
2. **Fundamentals and State of the Art**—provides the theoretical background relevant to high-enthalpy two-phase flows, TPS, and erosion models, and reviews the current state of the art.

3. **Experimental Setup**—describes the L2K wind tunnel and details the implementation of all experimental techniques used across the different campaigns, including both established and newly-developed methods, thus *addressing the first research question.*
4. **Flow and Particle Characterisation**—presents the results from the measurement campaigns aimed at characterising the target flow conditions in the L2K wind tunnel, thereby *addressing the second research question and achieving the first sub-goal.*
5. **Sample Behaviour**—reports the material response of the studied samples under the previously characterised flow conditions, *addressing the second research question and sub-goal.*
6. **Data-Based Thickness Evolution Model**—introduces a novel approach for correlating particle flux measured from particle image velocimetry (PIV) data with time-resolved thickness evolution measured by laser-sheet profile tracking (LPT), *answering the third research question.*
7. **Conclusions**—summarises the main findings and provides a general outlook. Note that chapters 4 to 6 conclude with a *"Summary and Future Steps"* section, where the specific results are discussed in detail, and the subsequent actions required to address remaining research questions or enhance the current work are outlined.

This experimental investigation is unique in exploring high-enthalpy, particle-laden flows within an arc-heated wind tunnel—a rarely studied and experimentally challenging domain. Such works are extremely limited, and corresponding datasets are virtually absent in the literature. The data generated in this study form a solid basis for future research on ablative material characterisation and on the validation and development of two-phase flow and material ablation models.

1.2 Published Content

This manuscript reports and rearranges the contents of: four articles published in first-quartile peer-reviewed journals—table 1.1 (in the table, "Year" refers to the acceptance year); three conference items presented during a workshop (WS) about re-entry organised by European Space Agency (ESA), an International Planetary Probe Workshop (IPPW) and an European Conference for Aerospace Sciences (EUCASS)—table 1.2; a patent application invented by the author, written by Rühland Constantin (Dompatent von Kreisler Selting Werner) and owned by DLR—table 1.3.

The author declares that the content is original and that there are no known competing financial interests or personal relationships that could have appeared to influence the work reported in this manuscript.

Table 1.1: Published articles in first-quartile peer-reviewed journals

Title	Journal	Year	Ref.
Velocity measurements in particle-laden high-enthalpy flow using non-intrusive techniques	Experiments in Fluids	2024	[103]
PIV in the vicinity of cork samples in particle-laden high-enthalpy flow	Experiments in Fluids	2025	[104]
Characterization of ablator recession and thermal response using non-intrusive techniques	AIAA Journal	2025	[109]
1D thickness evolution model of cork ablators, including swelling, ablation and erosion	IJHMT*	2025	[108]
Martian flow characterization using tunable diode laser absorption spectroscopy, in high-enthalpy facilities†	Acta Astronautica	2023	[110]

* *International Journal of Heat and Mass Transfer.*

† *Ref. [110] was written during the author's master's thesis and should not count toward the doctoral thesis. Nevertheless, it is mentioned as some results were used.*

Table 1.2: Conference and workshop items

Title	Event	Date	Ref.
Particle-laden flow characterization in high enthalpy ground testing facilities	ESA Re-entry WS	Jan. 2024	[107]
Recession measurements of cork samples in particle-laden arc-heated wind tunnel*	IPPW	Jun. 2025	[106]
Particle image velocimetry on cork samples in arc-heated wind tunnels†	EUCASS	Jun. 2025	[105]

* *Bernie Bienstock Best Presentation Award*

† *ASI Best Student Paper Award*

Table 1.3: Patent application

Title	Type	Date	Ref.
Optisches Oberflächenmesssystem zur Oberflächenmessung eines Objekts in einem Windkanal sowie Windkanal mit einem optischen Oberflächenmesssystem und Verfahren zur optischen Oberflächenmessung eines Objekts in einem Windkanal	Patent application	27 Mar. 2025	[102]

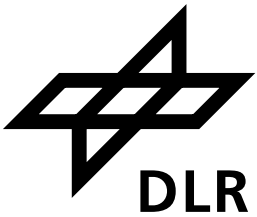
DLR

2 Fundamentals and State of the Art

Understanding the physical phenomena that govern atmospheric entry is essential to the design and qualification of future Mars missions. The extreme environment encountered during entry, descent, and landing poses significant thermal and mechanical challenges, demanding robust modelling and experimental tools for the development of reliable TPS. This chapter provides the theoretical background and a review of the state of the art necessary to frame the present research within this broader context.

2.1 Physical Processes during Martian Entry

Mars has a thin, cold atmosphere composed mainly of carbon dioxide (95.1%), with minor amounts of nitrogen (2.7%), argon (1.9%), and trace gases such as water vapour, carbon monoxide and oxygen [120]. Surface pressures average around 6.1 mbar, and temperatures typically range from 130 K to 300 K. This low-density environment creates unique challenges for atmospheric entry: although the aerodynamic heating is significant due to high entry velocities (typically 5.5 to 7.5 km/s [123]), the available atmospheric density for deceleration is limited, necessitating careful design of entry systems and thermal protection strategies. Typical entry conditions for Mars missions involve extremely high Mach numbers (> 20), strong bow shocks in front of the mostly blunt bodies, and intense convective and radiative heating [17, 52, 127].

Martian dust particles are mobilised by Martian aeolian processes [63], and can reach the upper levels of the atmosphere. Martian dust is composed of several chemical species, like silicon-, aluminium-, iron-, magnesium- and calcium- oxides [75]. Depending on the dust particles' sizes, ranging from sub-micron to tens of microns in diameter, they can pose a major threat to entry systems [3]. The presence of such particles introduces a two-phase flow regime, altering shock structure, increasing local heating, and posing risks to TPS, instrumentation, and optical navigation systems. In addition, particles generated by TPS ablation may re-enter the boundary layer and recirculate, further complicating the flow-field and requiring detailed multi-phase modelling.

Due to the rarefied nature of the Martian atmosphere—particularly at altitudes above 50 km [76]—continuum assumptions break down, and rarefied gas dynamics may become essential, both for flow and particle modelling [16, 49, 85]. Accurately predicting entry conditions requires sophisticated numerical models, whose reliability is critical to mission

safety. The lack of validation data poses an urgent need for dedicated experimental campaigns in ground-testing facilities like hypersonic wind tunnels.

The following sections provide an overview of the fundamentals needed to understand and model two-phase high-enthalpy flows, TPS, ablation and erosion processes.

2.1.1 Fundamentals of Two-Phase High-Enthalpy Flows

Two-phase high-enthalpy flows refer to fluid systems in which a gaseous phase (typically a high-temperature gas or plasma) interacts with a dispersed condensed phase, such as solid particles or liquid droplets, under conditions of extremely high total energy per unit mass (specific enthalpy). These flows are common in high-speed aero-thermodynamics, such as during atmospheric entry, high-speed propulsion, or plasma-material interactions. They require complex modelling approaches that account for gas-particle interactions, rarefied effects, and high-enthalpy conditions. The interaction between the gas and particles affects heat transfer, radiation, shock structure, and chemical non-equilibrium, necessitating a multi-phase modelling approach. In the context of Martian entry, suspended particles may originate from ambient dust or from ablation processes.

These flows are inherently multi-scale: particle diameters are in the micrometric range, while characteristic flow structures—such as shock stand-off distance and boundary layer thickness—can vary from millimetres to centimetres. The gas and particles may be in thermal and mechanical nonequilibrium, particularly in rarefied conditions where the Knudsen number is high.

Two-phase flows can be classified according to several criteria:

- **By phase type:** gas–solid, gas–liquid, or gas–droplet flows. In hypersonic and Martian entry scenarios, gas–solid systems are predominant. For instance, regarding ablated particles or the suspended regolith dust during entry.
- **By particle volumetric loading [11, 33]:**
  - *Dilute or dispersed phase*, characterised by low particle volume fraction and negligible inter-particle interactions.
  - *Dense or continuum phase*, characterised by higher concentrations where particle-particle interactions become significant.
- **By thermal and momentum coupling classes [18, 33, 121]:**
  - *One-way coupling*, valid for dilute flows: the gas has an effect on particle properties and motion, but no reverse effect is present.
  - *Two-way coupling*, valid for dilute flows: particles exchange momentum and energy with the gas, i. e. the reverse effect is present.

  - *Four-way coupling*, valid for dense flows: particles and flow interact in two-way coupling regime, while particle–particle interactions (e.g. collisions) must additionally be considered. Depending on the application, further gas-phase processes, such as diffusion, chemical reactions, or radiative heat transfer, may also need to be taken into account.

- **By equilibrium level** [121]: depending on the relaxation timescales between the phases, the system may approach thermal and chemical equilibrium, while momentum coupling may remain incomplete, leading to velocity slip (relative motion) between the phases.

A detailed summary of particle-laden flows classification is reported in figure 2.1, from [21], in terms of particle volume fraction ϕ_v (defining the particle loading) and relative Mach number between particles and gas (which is related to the relative velocity between the phases, as described in section 2.1.2). One can see that higher particle volume fractions require more detailed coupling approaches; higher relative Mach numbers necessitate considering complex phenomena such as turbulence, acoustics, and chocked flow between particles at dense regimes. These complex phenomena are introduced here but not further explained, as they fall outside the scope of the present work. In the graph, the previously mentioned dilute phase includes the *single particle*, *dusty gas*, and *intermediate* regimes.

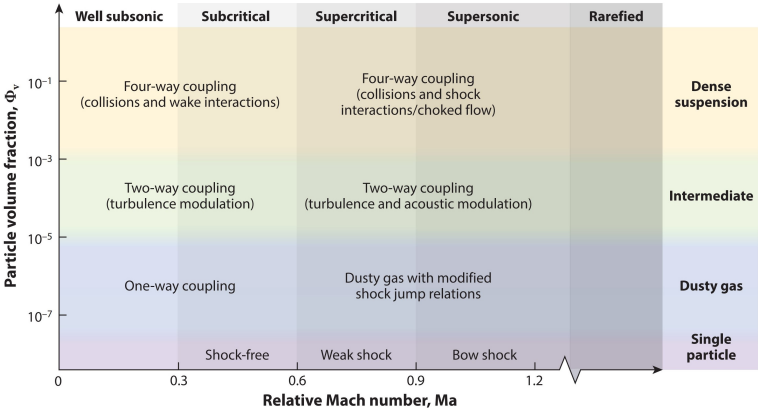

Figure 2.1: Different regimes characterising gas–particle interactions, in high Reynolds-number flows, in the continuum regime, from [21]

Compared to classical multi-phase flows, high-enthalpy two-phase hypersonic systems exhibit distinctive characteristics, such as: strong shock interactions and compressibility

effects [15, 20, 21, 48, 122]; pronounced thermal- and chemical- nonequilibrium phenomena [48]; high particle inertia, high relaxation times, and lag effects, particularly significant in the hypersonic regime [48, 122]; coupled radiative and convective heat transfer involving the particulate phase [48, 122]; possible mass transfer due to ablation, sublimation, or condensation processes [21, 48]. The dynamics of solid particles in high-enthalpy gas flows are governed by complex physical mechanisms that include aerodynamic drag, thermal response, slip behaviour, and gas–surface energy exchange. Accurate prediction of these effects is crucial in two-phase flow modelling and spacecraft design.

For these reasons, modelling two-phase high-enthalpy flows requires a coupled treatment of several physical processes [114, 122, 129], including:

- **Fluid dynamics**: viscous flow effects and compressible gas behaviour, often involving shock waves and expansion fans;
- **Particle dynamics**: inertia, drag, lift, and thermophoresis;
- **Thermodynamics**: high-temperature gas properties and particulate heating;
- **Chemical kinetics**: reactions, ablation chemistry, and nonequilibrium effects;
- **Multi-phase formalisms**: either Eulerian–Lagrangian or Eulerian–Eulerian frameworks, chosen based on particle loading and computational scale.

As mentioned in [122], additional complexity is generated when two-phase high-enthalpy flow effects on bodies need to be modelled. Several effects need to be considered, such as the different aerodynamic drag, the heat transfer, and the erosive effect of the second phase.

2.1.2 Governing Parameters of Particle–Flow Interactions

According to [4, 21, 25, 121], the governing parameters of particle-laden flows are the following.

Slip Velocity The slip velocity $\mathbf{v}_{slip}$ is the relative velocity between a particle and the surrounding gas. This quantity governs the aerodynamic forces and convective heat transfer between phases. Large slip velocities are common near shock waves or in accelerating/decelerating flows (e. g. the wind tunnel's nozzle expansion), leading to strong non-equilibrium conditions. Let $\mathbf{v}_g$ and $\mathbf{v}_p$ be the gas and particle velocities, respectively. The slip velocity is then:

$$\mathbf{v}_{slip} = \mathbf{v}_g - \mathbf{v}_p \tag{2.1}$$

Particle Mach Number (Ma_p) The particle relative Mach number relates the particle slip velocity with the local speed of sound. Peculiar physical phenomena can happen according to its values (refer for instance to figure 2.1). Let γ, R and T be the specific heat ratio, the gas constant and the gas temperature, respectively. The particle Mach number is then:

$$Ma_p = \frac{|\mathbf{v}_{slip}|}{\sqrt{\gamma R T}} \tag{2.2}$$

Particle Reynolds Number (Re_p) The particle relative Reynolds number quantifies the relative importance of inertial to viscous forces acting on the particle, and defines the flow regime around it. Being ρ_g and μ_g the gas density and dynamic viscosity, and d_p the particle diameter, the particle Reynolds number is:

$$Re_p = \frac{\rho_g |\mathbf{v}_{slip}| d_p}{\mu_g} \tag{2.3}$$

Particle Knudsen Number (Kn_p) It quantifies the level of rarefaction by comparing the mean free path of the gas λ_g to a characteristic particle length scale:

$$Kn_p = \frac{\lambda_g}{d_p} = \sqrt{\frac{\gamma\pi}{2}} Ma_p \tag{2.4}$$

Depending on Kn_p, the gas–particle interaction regime is classified as reported in table 2.1. In Martian upper atmosphere conditions, Kn_p can exceed unity for sub-micron particles, requiring modified drag and heat transfer models.

Table 2.1: Flow regime classification by particle Knudsen number [84]

Kn_p range	Flow regime
$Kn_p < 0.01$	Continuum
$0.01 < Kn_p < 0.1$	Slip
$0.1 < Kn_p < 10$	Transitional
$Kn_p > 10$	Free-molecular

Stokes Number (St) This number determines how flow and particle are inertially coupled. It represents the ratio of particle response time τ_p to the characteristic flow time scale τ_g: particles with $St < 1$ are tightly coupled to the gas flow and follow streamlines, whereas particles with $St \gg 1$ exhibit significant lag and may decouple from the flow. Different types of Stokes number exist, based on the significance of the term τ_g, which can be based on averaged motion, large-scale, or small-scale fluctuations.

$$St = \frac{\tau_p}{\tau_g} \tag{2.5}$$

For instance, τ_p can be modelled as: $\tau_p = \frac{\rho_p {d_p}^2}{18\mu_g} C(Kn_p)$, where C is the Cunningham slip correction factor, accounting for non-continuum effects when calculating drag on small particles [130].

Particle Drag Coefficient (C_D) Particles exchange momentum and energy with the surrounding flow; depending on the two-phase coupling class, the effect may alter flow properties when mass loading is significant [21]. If a single particle with mass m_p is subjected to different forces $\mathbf{F}_i$, its equation of motion is:

$$m_p \frac{d\mathbf{v}_p}{dt} = \sum_i \mathbf{F}_i \tag{2.6}$$

The forces acting on the particles can be, for instance: gravity, quasi-steady drag forces, undisturbed flow forces (as the pressure gradient or Archimedes force), inviscid unsteady forces (i. e. added mass), or viscous steady forces (Basset history force) [21]. Notably, the drag force depends on the slip velocity and the drag coefficient C_D:

$$\mathbf{F}_D = \frac{1}{2} C_D \rho_g A_p |\mathbf{v}_{slip}| \mathbf{v}_{slip} \tag{2.7}$$

The estimation of the drag coefficient C_D is non-trivial, especially if the particle shape is non-standard [4]. In case of simple geometries like the sphere, C_D depends on Re_p, Ma_p and Kn_p, as shown in figure 2.2, from [21].

Nusselt Number (Nu) and Heat Exchange Particles exchange energy by convective and radiative heating, and chemical reactions. Convective heating depends on the particle cross-sectional area A_p, on the convective heat coefficient h, and on the temperature difference between particle p and gas g:

$$q_{\text{conv}} = h A_p (T_g - T_p) \tag{2.8}$$

In this sense, the particle Nusselt number Nu is a dimensionless number that characterises convective heat transfer between particle and the surrounding gas. It can be modelled via Ranz–Marshall or slip-corrected correlations, according to [1]:

$$Nu = \frac{h d_p}{k_g} \tag{2.9}$$

where k_g is the thermal conductivity of the surrounding gas.

Radiative heating depends on the Stefan-Boltzmann constant σ, on the emissivity ε, on the particle area A_p, on the particle temperature T_p, and on the radiative temperature T_{rad} (or *effective temperature*) of the surroundings:

$$q_{\text{rad}} = \varepsilon \sigma_B A_p (T_{\text{rad}}^4 - T_p^4) \tag{2.10}$$

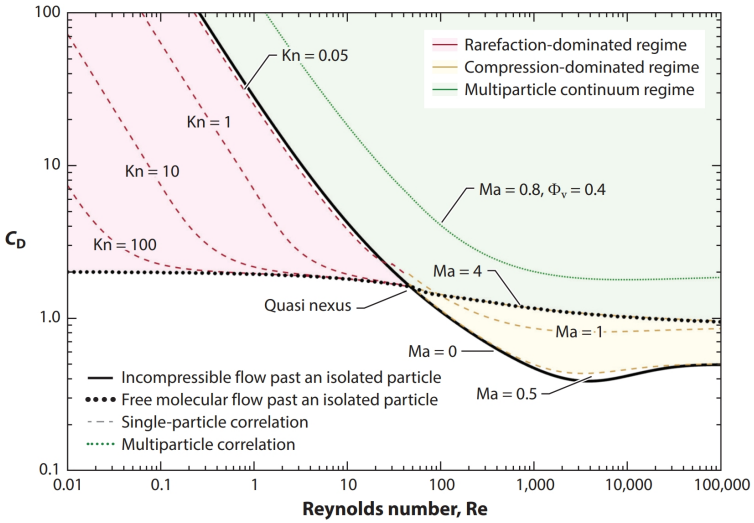

Figure 2.2: Drag coefficient C_D of a sphere, from [21]

Considering radiative and convective heat exchange, plus the heating/cooling effect during phase change (melting, solidification, ...) and the chemical heating due to reactive processes (surface reactions, oxidation, recombination), the thermal energy balance on a particle can be written as:

$$m_p c_p \frac{dT_p}{dt} = q_{\text{conv}} + q_{\text{rad}} - q_{\text{phase change}} + q_{\text{chem.}} \tag{2.11}$$

where c_p is the particle's specific heat capacity, and m_p is the particle mass.

Modelling particle–flow interactions is inherently challenging because of the complex coupling between the dispersed and carrier phases. The difficulty increases further when considering the interaction of particle-laden flows with solid surfaces, such as those of TPS, where impact, erosion, deposition, and heat transfer come into play. Capturing these effects accurately is essential to predict material response under realistic entry conditions and remains a key challenge in modelling high-enthalpy, multi-phase flows relevant to planetary entry.

2.1.3 Thermal Protection Systems

TPS are needed to protect spacecraft from the aerothermal heating encountered during atmospheric entry: the standard lightweight materials used for space structures—such as aluminium, carbon fibre-reinforced polymers, etc.—might melt, or might not be efficient in dissipating heat, leading to the destruction of spacecraft payloads and internal components. Different types of TPS exist, and they're categorised—according to their power consumption—into active, semi-passive, and passive [38, 119]. Active TPS systems include convective, film, and transpiration cooling, and require electrical power to operate. Passive systems are heat sinks, hot structures, tiles, coatings, and insulating materials. Semi-passive systems include phase change materials such as ablators and heat pipes. Passive and semi-passive systems do not require external power, unless sensors are used to observe the system's state.

When choosing the most suitable TPS for a mission, power consumption cannot be considered the only design driver. In fact, some missions may impose requirements on system controllability, while others may prioritise simplicity and reliability. For certain missions, a simple expendable TPS might be sufficient, while others may benefit from the long-term cost-effectiveness of a reusable one. In this context, active TPS solutions are typically heavier, more complex, and more expensive than passive systems, but they are usually reusable and provide thermal controllability, in contrast with passive and semi-passive ones, which are simpler and, usually, non-controllable. While some passive or semi-passive systems are reusable—for example, the heat tiles used on SpaceX's Starship and NASA's Space Shuttle [77]—others are designed for single use, such as the heat shields used on Martian landers, on the Apollo, on the Soyuz, and on the Dragon capsules [26, 34, 89, 116].

Therefore, heat shields can also be classified in two main categories: expendable and reusable [50]. This manuscript focuses on characterising the thermal response and the recession of a specific ablative material. For this reason, ablators are described in detail in the following section.

2.1.4 Ablative Materials

Ablative materials provide a simple and reliable protection from high heat fluxes for limited times. They do not require power and they are used in a wide range of applications in hypersonic flight and spaceflight, as they provide a cost-effective option for missions designed for non-reuse. In ablative systems, material recession and the release of gaseous and particulate products can modify the vehicle shape and contaminate the surrounding flow field, making the TPS response an important driver in overall system design.

An ablative heat shield works by sacrificial material removal to protect the underlying structure from extreme heating. Ablative materials are able to absorb and dissipate heat through endothermic processes, thanks to their peculiar chemical composition—the majority of ablators for re-entry application is made of a dispersed phase, bound by a matrix. Different matrices and dispersed phases confer different properties to the ablator, in terms of heat ablation efficiency, thermal conductivity, density, etc. Commonly used ablative materials are composed of:

- *Carbon fibre & phenolic resin*, such as ZURAM [96], and PICA and its variants (used in Mars Science Laboratory (MSL) [14], SpaceX Dragon [116], and Dragonfly [117]).
- *Fibreglass & epoxy resin*, such as AVCOAT (used in Apollo [89] and Artemis [111]).
- *Silica fibre & phenolic resin*, such as SLA-561V (used in Mars Pathfinder [73]), or the material used to cover ESA-IXV's antennas [23].
- *Cork & phenolic resin*, such as Norcoat Liège (used in ExoMars Schiaparelli [12]) and P50 (used in ESA-IXV [23, 101]).

The typical ablation process is based on the controlled material degradation favoured by endothermic reactions:

1. As the material is exposed to high heat fluxes, the binder in the outer layer starts decomposing through **pyrolysis**—that is the endothermic chemical breakdown of long polymeric chains [72]. The pyrolysis front moves inward, affecting the virgin material, which is gradually reduced with time.
2. Pyrolysis produces gases that blow outward. **Outgassing** generates a colder boundary layer that provides transpiration cooling effects, and pushes the shock away from the surface, reducing heat transfer. Furthermore, these gases can cause material swelling in some types of ablators.
3. The remaining—possibly swollen—solid phase after pyrolysis constitutes a **char** layer, that is a porous structure with insulating properties that slows heat conduction.
4. Finally, the surface material is subject to **ablation** caused by melting, sublimation, spallation, shear erosion and chemical reactions (e. g. oxidation) [30, 94, 98]; this process can be both exo- or endothermic and carries thermal energy away, therefore cooling the surface by hot mass loss.
5. The mass loss causes material **recession**.

The combination of endothermic reactions, surface cooling, thermal insulation, and mass loss during ablation, makes ablative materials an ideal choice for protection against high heat fluxes [13].

Terms related to ablation processes are often used inconsistently in the literature, and it is therefore important to clarify their distinct meanings:

- **Swelling** defines the expansion of the material, typically caused by outgassing, charring, and thermal expansion.
- **Ablation** describes the mass loss due to high thermal and mechanical loads. It encompasses the effects of:
  - Pyrolysis (material decomposition),
  - Phase change (melting, evaporation, sublimation),
  - Spallation (sudden mechanical removal of surface chunks due to thermomechanical stress),
  - Shear erosion (gradual removal of material by continuous shear forces),
  - Chemical reactions with the flow (for example, oxidation, or reactions with free radicals),
  - Particle-induced erosion (mechanical removal of the surface layer due to particle impact).
- **Recession** is the net backward movement of the surface, caused by the combined processes of swelling and ablation—it happens when the ablation rate is higher than the swelling rate.
- **Thickness Evolution** is the combination of swelling and ablation. According to the convention used in this manuscript, it is positive in case of overall recession, and negative in case of prevalent swelling.

In this work, the term thickness evolution is sometimes shortened to *evolution*, and particle-induced erosion is referred to simply as *erosion*—not to be confused with shear erosion.

2.1.5 Erosion Rate Modelling

A particle-laden flow impacting a surface causes particle-induced erosion. In [91, 92] erosion is described as a material-dependent process that starts with a transient and stabilises in a quasi-steady phase with constant erosion rate.

Erosion is due to the combination of multiple effects, such as the cutting wear and the deformation wear, as described in [46, 66]. The cutting wear is prominent when the impact angle is close to zero (i. e. the particle moves almost parallel to the surface), while the deformation wear gains importance when the impact angle is close to 90° (i. e. particles' trajectories are almost perpendicular to the surface). In this work's scenario,

the cutting wear is considered negligible, with respect to the deformation wear, as the wind tunnel flow is almost perpendicular to the sample surface.

The main contributions to erosion are given by particle size d_p, mass m_p, velocity $\mathbf{v}_p$, impact angle α, and material hardness H_v, as described by [46, 47]. In the mentioned works, the Oka erosion model was used [79, 80], which relates the mass loss Δm to particle and material characteristics:

$$\frac{\Delta m}{\Delta m_p} = c_1 {H_v}^{c_2} {\mathbf{v}_p}^{c_3} {d_p}^{c_4} (\sin\alpha)^{c_5} \tag{2.12}$$

valid for α close to 90°, where c_i are the model's coefficients. In specific studies related to Martian entry conditions and cork modelling, similar material-dependent erosion models were reported [53, 84, 86], highlighting the dependency of the surface erosion depth Y^e on the impact crater and penetration depth, that in turn depend on particle density ρ_p, total particle number N_p, α, $\mathbf{v}_p$, and d_p:

$$Y^e = c_6 {\mathbf{v}_p}^{c_7} {d_p}^{c_8} {\rho_p}^{c_9} N_p (\sin\alpha)^{c_5} \tag{2.13}$$

According to this equation, one could relate erosion to particle's kinetic energy or momentum.

The erosion rate can be evaluated by deriving equation (2.13). Assuming no change in particle properties (size, shape, and density), and constant velocity:

$$\frac{dY^e(t)}{dt} = c_{10} \frac{dN_p(t)}{dt} \tag{2.14}$$

where $\frac{dN_p(t)}{dt}$ is the particle flux, defining the particle number per unit time.

2.2 State of the Art

The following review summarises the current state of the art on topics relevant to the present research, encompassing both modelling and experimental efforts aimed at understanding particle-laden, high-enthalpy flows and their interaction with TPS. It first outlines the main challenges associated with the mathematical modelling of such complex environments, then reviews past experimental campaigns that have contributed to characterising particle behaviour and their effects on materials. Particular attention is given to particle flow characterisation and collection techniques, as well as to the influence of particles on TPS performance. Finally, specific studies on P50 cork swelling and recession are discussed, together with existing approaches for ablation modelling, providing a comprehensive framework for interpreting the results of the present work.

Mathematical Modelling Challenges Modelling high-speed, high-enthalpy, two-phase flows remains challenging, partly due to limited efforts in including compressibility effects [21]. The relative slip velocity between particles and gas, along with one-way, two-way, or multi-way coupling of momentum, mass, and energy, significantly increases complexity. Many Martian-dust studies assume only one-way coupling, neglecting particle feedback on the gas. Numerical frameworks such as the coupled US3D–DUST solver treat particle–fluid interactions and energy exchange with higher fidelity [99]. Key gaps remain, such as validated relations for drag, heat transfer, and mass exchange in dusty, high-enthalpy CO_2 / N_2 flows, characterisation of slip velocity distributions [128], and robust multi-way coupling, including gas–particle–surface exchange of energy and momentum. Comprehensive experimental datasets covering gas and particle phases (velocity, temperature, size distribution, and loading) under entry-relevant conditions are virtually absent in the literature. Moreover, experimental campaigns so far, are limited by partial coupling (no simultaneous gas and particle field measurements), restricted enthalpy or pressure ranges [5], and low representativeness of Martian dust aerosols.

Relevant Past Experiments Supersonic particle-laden air flows were created in the GBK and characterised by shadowgraphy and particle tracking velocimetry (PTV) [4–6]: particle velocity and size were measured and heat flux augmentation was observed on the probes inserted in the two-phase flow. Based on this knowledge, additional research is being performed in the L2K arc-heated wind tunnel to include high-enthalpy effects, thus increasing the accuracy of the Martian atmospheric entry simulation in ground testing facilities. Particle-enhanced heat flux was observed in the L2K in [27], where a particle-laden flow at supersonic/hypersonic speed was created for the first time in the L2K wind tunnel. The flow characterisation of the flow conditions studied in this work began in [110] where tunable diode laser absorption spectroscopy (TDLAS) was applied and analysed. A picture of a dusty-flow test in the L2K is shown in figure 2.3, where the sample interacts with the particle-seeded high-enthalpy flow: the presence of suspended particles is revealed by a green light-sheet and a bright red-orange bow shock, while the blue-green wake indicates ablation products.

Relevance of L2K Environment for Martian Entry The L2K arc-heated wind tunnel can operate with a simulated Martian atmosphere that can be seeded with micrometric particles. In terms of particle Knudsen number Kn_p and particle Reynolds number Re_p, the L2K reproduces the relevant ranges encountered during Martian atmospheric entry. As discussed in [85], for micrometric particles, the particle Knudsen numbers in Martian shock layers range between 0.8 and 10, corresponding to transitional flow conditions; under L2K operating conditions, particle Knudsen numbers fall within the same range, indicating a direct match in particle flow regime. Furthermore, the characteristic particle Reynolds numbers in the L2K remain below approximately 45, which is consistent with the values reported for Martian entry conditions, demonstrating that both environments

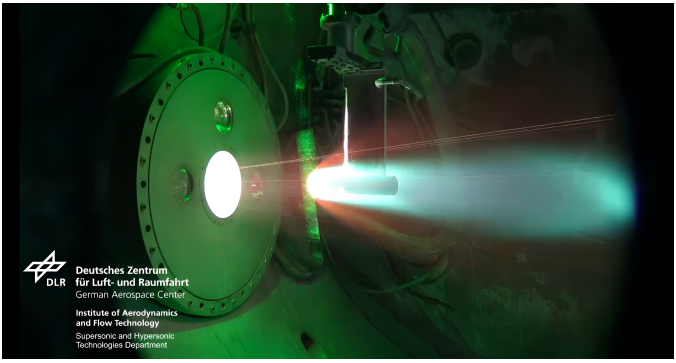

Figure 2.3: Particle-laden flow test with sample in the L2K

are characterized by rarefaction-dominated regime. As a result, the corresponding particle drag coefficients C_D are expected to be comparable, as they are governed by similar combinations of Knudsen and Reynolds numbers.

Particle Flow Characterisation Particle imaging-based techniques need to be implemented in the wind tunnel for the characterisation of the particle-laden flow: PIV was exploited in this work with the goal of measuring particles' mean velocity in the wind tunnel environment, obtaining a first important result for understanding particles' behaviour in the two-phase high-enthalpy flow, as a first step towards future experiments for TPS characterisation. PIV is a widely established experimental technique for non-reactive flow diagnostics, comprehensively described in [95], which spreads across the most diverse fields of flow visualisation. It was implemented in hypersonic wind tunnels, such as in blow-down wind tunnels [67, 78, 115] and in shock tubes [39, 57]. In [39], particle speeds of about 2500 m/s were measured, confirming that with proper hardware settings, hyper-velocities can be measured. PIV was applied in an arc-heated facility for supersonic combustion testing, where specific enthalpy of 3.5 MJ/kg were measured [62]. PIV applied to a long duration arc-heated wind tunnel dedicated to TPS testing was never performed. In such a facility, the low flow density, combined with the high temperatures of the reservoir, make particle seeding and particle imaging techniques challenging. Particle-laden flows in L2K were studied in [53] and [27], where laser-to-focus (L2F) technique was applied. Differently from L2F, PIV allows velocity measurement on a broad region of interest, though being more limited on the resolution, by the used camera objective.

Particle Collection In this work, some particles are collected inside the flow, with the goal of studying their morphology to better characterise the particle-laden flow conditions. Although conceptually simple, particle collection in high-enthalpy flows is a challenge. Particle samples were collected in high-enthalpy flows in [100], where a probe was developed ad-hoc for collecting alumina particles from solid rocket combustion, following the idea of [55]. The probe was cooled and had an internal spray system that could collect the particles in a liquid sample, which would then be analysed. Developing such a probe for particle collection in the L2K is complex, and a simpler technique is preferred at this stage of the study. In a recent publication, double-sided carbon tape was used to collect particles from a green propellant thruster plume [19], and the collected particles were then analysed with a scanning electron microscope (SEM). MgO particles were observed with a SEM in [124], confirming the feasibility of this imaging technique for the selected chemical species. This analysis can provide insights into the morphological changes of the particles after impact. However, it cannot be used to determine their shape and size through image post-processing (as demonstrated, for instance, in [60]), due to the intrusive nature of the collection technique.

Particle Effects on TPS The particle-enhanced heat flux on the heat shields is due to several different phenomena, such as: conversion of the particles kinetic energy into thermal energy through elastic or inelastic collision [37, 93], generation of additional shear layers by rebounded particles crossing the bow shock [2, 45, 58, 64], increase in boundary layer turbulence [10], change in the bow shock structure by particle accumulation in front of the probe [58], disturbance of the particles on the bow shock [32, 37], change in surface roughness and erosion [32, 82]. Note that in this heavily complex environment, the geometry of heat shields can deform: their *thickness evolution* is caused by material *swelling* and *ablation*. The complexity of the topic requires dedicated experimental campaigns in suited wind tunnels, both to enhance our understanding of the characteristic physical phenomena and to validate numerical predictions.

TPS Performance Characterisation To characterise TPS performances, several parameters can be studied, such as the surface temperature, the in-depth temperature and the sample's thickness evolution, that highly depend on the material used. Surface temperature can be measured with infrared (IR) thermography, while in-depth temperature with embedded thermocouples. The thickness evolution measurement (usually referred to as *recession-* or *erosion measurement* in the literature) has always been a challenge during tests in high-enthalpy wind tunnels, due to the difficulty of working with high-enthalpy flows, the unsuitability of intrusive techniques, and the limited optical accessibility of the facilities. In the past, several experimental techniques were carried out: digital image correlation (DIC) [29, 65, 113], laser dot-maps [83], sample profile tracking with image processing and neural network [42], and fibre optic interferometry [112] or other intrusive techniques [74]. Often, the comparison of the samples' tri-dimensional (3D) scans before

and after the tests was considered a sufficient indicator of the overall thickness evolution. 3D scans however do not provide the time resolution of the thickness evolution, which is essential to observe phenomena such as material swelling at the beginning of a long test. In this work, a new solution to the thickness evolution measurement challenge is proposed and described in section 3.3.6; this technique will be addressed to as laser-sheet profile tracking, or LPT.

P50 Cork Swelling and Recession Within the ESA QARMAN project, cork-based ablators such as P50 have been extensively investigated as candidate TPS materials for small re-entry capsules [9, 101]. These studies demonstrated that cork does not only undergo surface recession driven by ablation, but also significant swelling of the char layer, making its thickness evolution the result of a coupled ablation–swelling process. Accurately capturing both effects is crucial for predictive modelling, as neglecting swelling can lead to underestimation of the material thickness and overestimation of heat flux penetration, directly impacting the design and safety margins of TPS for Martian or Earth re-entry scenarios. As mentioned in [9, 101], cork-based ablators present a non-linear behaviour at the beginning of the test where they experience swelling: samples thickness evolves to negative values. Then, ablation processes start, and recession gains prominence over swelling. The long-term recession rate is constant, and therefore the evolution's slope is constant. The typical evolution process of cork-based ablator is reported in figure 2.4, taken from [9].

Ablation Modelling Accurate prediction of ablative material performance under hypersonic entry conditions requires an extraordinary modelling effort, due to the inherently multi-scale and coupled nature of the physical processes involved. High-fidelity ablation modelling seeks to capture the decomposition of the polymeric matrix, the generation and transport of pyrolysis gases through a dynamically evolving porous char, the interaction of these gases with the boundary layer, the radiative heat exchange within the char material, and the concurrent evolution of surface recession and material properties. These phenomena are deeply intertwined: the rate of pyrolysis influences gas production, which in turn affects internal pressures and cooling, while changes in char density and permeability feed back on both the thermal response and the surface ablation rate. Radiation, chemical non-equilibrium, and convective heat fluxes from the high-enthalpy flow further couple with the material response, making the system extraordinarily stiff and computationally demanding. Significant efforts to model these processes have seen in the past the parallel effort of several research groups in the United States [36, 69, 125] and in Europe [44, 59, 90, 97, 98], combining experimental characterisation, multidimensional simulations, and uncertainty quantification frameworks. Commonly used high-fidelity models are, for instance, the DLR's FAST tool [28], the NASA's LAURA code [51, 118], and other models [35]. Despite this progress, the complexity of the coupled phenomena, combined with uncertainties in kinetic parameters, material microstructure, and boundary conditions,

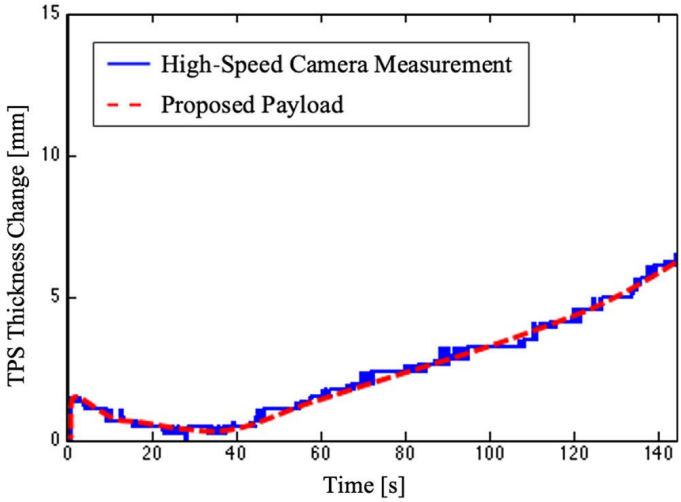

Figure 2.4: Typical cork-based ablator evolution process, from [9]

presents a persistent risk in prediction accuracy, highlighting the need for continued research, improved experimental validation, and systematic approaches to quantify and reduce uncertainty in high-fidelity ablation simulations. As an alternative to high-fidelity approaches, an ablation model could be formulated directly from experimentally observed material response under representative thermal and aerodynamic loading conditions. This strategy offers notable advantages: it is relatively straightforward to implement and it can provide reliable predictions if properly validated against experimental data. However, a significant limitation is the requirement for a sufficiently comprehensive database linking flow conditions to material response; currently, the lack of such data limits predictive accuracy for conditions different from those investigated, highlighting an important avenue for future experimental and validation efforts.

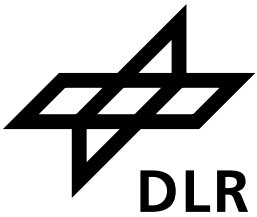
DLR

3 Experimental Setup

Before the TPS performance can be meaningfully assessed, the dusty-flow environment itself must be thoroughly characterised to ensure test repeatability and to gain a detailed understanding of its physical properties. Such flow characterisation is essential not only for the proper interpretation of experimental results but also for the validation of numerical models.

The particle-laden high-enthalpy flows in the L2K facility are defined by both *gas-phase properties* (temperature, pressure, mass flow rate, composition, velocity) and *particle properties* (size, velocity, shape, mass flow rate, temperature). Since not all these parameters can be directly measured, complementary numerical simulations are required to support the experimental data and provide a more complete description of the flow field.

This chapter presents the experimental setup and the diagnostic techniques employed in this study. It begins with an overview of the L2K arc-heated wind tunnel and its operational characteristics, followed by a description of the test samples used for demonstration. Subsequently, all diagnostic techniques used are described together with their relevant configurations. Finally, the numerical setup used for the computational fluid dynamics (CFD) computations is described.

The overall experimental design aims to measure particle properties and material ablation independently, thereby enabling the identification of correlations between particle characteristics (e.g., velocity, which is necessary to find particle kinetic energy and momentum) and the resulting erosion effects.

3.1 L2K Wind Tunnel

L2K is a long-duration arc-heated high-enthalpy wind tunnel suited for TPS materials testing and components' demisability tests, as it can provide high heat fluxes for long testing times, at the expense of aerodynamic properties characterisation: the low density environment causes the flow Reynolds number Re to be too low compared to atmospheric entry. In such conditions it is important to consider a reacting non-equilibrium flow. L2K reservoir is energised by a 1.4 MW Huels-type arc heater which grants the flow a high specific enthalpy thanks to the electrical discharge. The facility has different degrees of freedom for designing a specific flow condition (FC), such as mass flow rate, reservoir

pressure[1], nozzle exit diameter, sample position[2], and chamber background pressure. A broad selection of intrusive and non-intrusive measurement techniques can be used, such as: thermocouples, IR cameras, pyrometers, Pitot probes, TDLAS, laser-induced fluorescence (LIF), Fourier transform infrared spectroscopy (FTIR), PIV, LPT.

The analysed FCs were defined by DLR in the post-flight analysis of ESA ExoMars 2016 mission [41], and are reported in table 3.1. Here, the superscript ^{P} indicates the flow condition with particles, while the superscript ^{nP} indicates no particles in the flow. The wind tunnel flow represents a slightly simplified Martian atmosphere whose composition is 97% CO_2 and 3% N_2. The used L2K nozzle geometry is reported in figure 3.1.

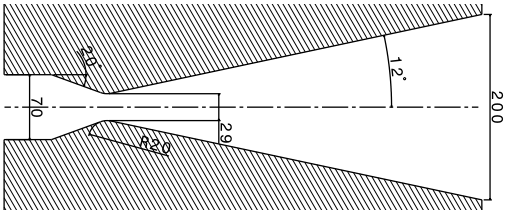

Figure 3.1: L2K nozzle geometry, 200 mm exit diameter configuration. Sizes in mm

Table 3.1: Flow conditions FCs. The superscripts ^{P} and ^{nP} indicate the FCs with and without particles respectively. The mass flow rates are equal for all FCs

Parameter	**FCI**^{nP}	**FCII**^{nP}	**FCI**^{P}	**FCII**^{P}
Reservoir pressure, [hPa]	790	930	790	930
MgO Particles	✗	✗	✓	✓
Predicted specific enthalpy*, [MJ/kg]	5.6	9.2	5.6	9.2
Predicted reservoir temperature*, [K]	2815	3283	2815	3283
Total mass flow rate, [g/s]	41.2			
Mass flow rate CO_2 (97%), [g/s]	$38^{hot}+2^{BP}$			
Mass flow rate N_2 (3%), [g/s]	1.2^{hot}			

*Estimated with quasi-1D flow solver NATA [8]

To generate the particle-laden flow, a seeding generator inserts particles in the L2K flow upstream of the nozzle expansion. The seeding generator is a pressurised vessel working with a bypass (BP): to keep the mass flow rate as specified in table 3.1, 38 g/s of CO_2

[1]Given a maximum installed power, the maximum heat flux and maximum stagnation pressure are competing parameters: to obtain high stagnation pressure, high mass flow rates must be selected, reducing the specific enthalpy of the flow, and so its temperature and heat flux on the sample.

[2]Thanks to the use of conical nozzles, the heat flux varies also on the flow axis.

are heated in the arc-heater together with 1.2 g/s of N_2 (superscript ^{hot}), while 2 g/s of CO_2 are used for collecting the particles inside the pressurised vessel (superscript ^{BP}). Particles of magnesium oxide (MgO) are stored inside the pressurised vessel.

The particles used are LUVOMAG®M SF, which the manufacturer specifies to have 95% of particles in the 1–3 μm range, according to the datasheet. According to [84, 85], this size range is valuable for generating representative data for Martian entry studies, as discussed in section 2.2. MgO particles were selected for their exceptionally high melting temperature, which, at this stage of the study, considerably simplifies wind tunnel operation by minimising melting and reducing the risk of nozzle clogging. MgO is considered suitable at this stage for investigating erosive effects, even though it does not replicate the full chemical composition of Martian dust. The primary mechanism of interest is mechanical erosion, which depends mainly on particle size and density rather than chemical makeup. Martian dust is composed primarily of silicon dioxide (density 2.65 g/cm^3) and iron oxide (density 5.24 g/cm^3), while MgO has a density of 3.58 g/cm^3, lying between these two components. This makes MgO an adequate candidate for reproducing the impact dynamics relevant to L2K experiments. To minimize aggregation due to storage, handling, humidity, or electrostatic charge, the particles were stored dry, sieved, and oven-dried for at least one hour before each experiment.

3.2 P50 Cork Samples

The samples used in this study all have the same characteristics, to address the repeatability of the tests in the L2K wind tunnel. The sample geometry and its cross section highlighting thermocouple placement are presented in figures 3.2a and 3.2b respectively. The material is P50, a phenolic-cork composite from the company Amorim Cork Solutions [7]. Three thermocouples are placed inside each sample at different distances from the front surface, namely 6 mm, 12 mm, and 18 mm. The thermocouples are slightly offset from the sample axis to be less intrusive on the heat conduction on the sample's axis. The offset is 1 mm by design.

A picture of the instrumented sample, and its installation in the wind tunnel before the test are shown in figures 3.3a and 3.3b, respectively. All tests are conducted following the same experimental procedure; the only varying parameters are the reservoir pressure and the presence of particles, as summarised in table 3.1. During a wind tunnel test the sample is positioned on the flow axis after the flow is stabilised, at a distance of $x = 300$ mm from nozzle exit. The residence time in the flow is set to 60 s. The expected cold-wall heat flux and stagnation pressure are reported in table 3.2. The heat flux values are comparable to the ones calculated in [68], for the MSL entry module. A total of 10 tests are performed, namely 2 tests per each FCs^{nP} and 3 per each FCs^{P}, to assess repeatability.

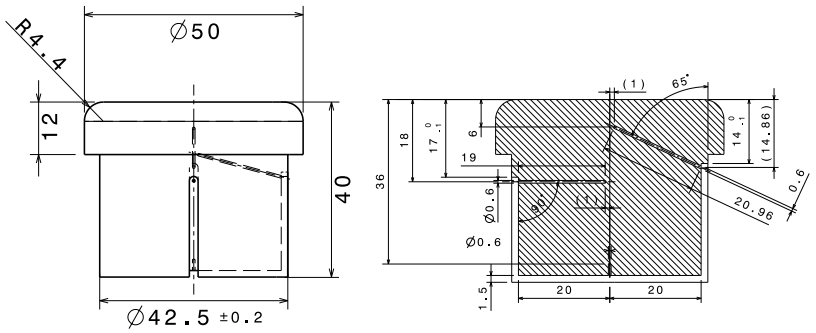

(a) Sample geometry **(b)** Sample cross section

Figure 3.2: Sample geometry and its cross section, highlighting the shallower thermocouple. The bottom thinner side is used to position the thermocouples, and to connect to the cooled support of the L2K

The campaign showed repeatable results, thus only one run per flow condition is often reported in chapter 5.

Table 3.2: Test parameters for different flow conditions

Flow condition	Sample position x	Residence time	Stagnation heat flux*†	Stagnation pressure*
FCI$^{P/nP}$	300 mm	60 s	280 kW/m^2	1280 Pa
FCII$^{P/nP}$	300 mm	60 s	490 kW/m^2	1510 Pa

* These values are computed numerically with the DLR-TAU solver assuming fully-catalytic wall, with the setup described in section 3.4.
† $1\left[kW\ m^{-2}\right] = 0.1\left[W\ cm^{-2}\right]$



(a) Instrumented sample



(b) Sample installed on the wind tunnel holder

Figure 3.3: Sample before testing. The flow will come from the left

3.3 Relevant Experimental Techniques

This section describes the configuration and operating conditions of all experimental techniques employed. The techniques used for flow and particle characterisation are: tunable diode laser absorption spectroscopy (TDLAS), particle image velocimetry (PIV), particle count, and intrusive particle collection (sections 3.3.1 to 3.3.4). The ones employed for material response characterisation include: global surface evolution measurements obtained via 3D scanning, in-situ thickness evolution monitoring using laser-sheet profile tracking (LPT), temperature measurements performed through IR thermography and embedded thermocouples, X-ray imaging, and qualitative visual observations acquired with high-resolution cameras (sections 3.3.5 to 3.3.9).

3.3.1 Tunable Diode Laser Absorption Spectroscopy (TDLAS)

TDLAS is a line-of-sight, non-intrusive diagnostic technique that enables the measurement of flow velocity and species concentration along defined paths [110]. It employs a narrow-band diode laser whose peak wavelength can be tuned by a few nanometres, allowing the scanning of narrow spectral regions around the absorption line of a target compound. By analysing the properties of these absorption lines, detailed information on the flow can be obtained. In particular, the core flow velocity can be inferred using a profile-fitting approach. In this work, the term "point measurement" refers to the core velocity obtained through this method, as detailed in [110], where the absorption line R7 of CO (centred at 2331.9 nm) was studied.

The TDLAS analysis is cited here for comparison purposes with particle velocity obtained with PIV. By comparing the results obtained with the two experimental techniques, one can have a hint on the velocity lag between particles and flow. TDLAS flow diagnostic was performed without particles, measuring velocities in three points on the flow axis, corresponding to $x = \{100, 200, 300\}$ mm downstream of the nozzle exit, at the same FCs^{nP} mentioned in table 3.1. The figures 3.4a and 3.4b show the conceptual scheme of the experimental setup, and the measured flow velocity compared with CFD, respectively, for both high- and low-enthalpy particle-free flow conditions. In this work, only the point measurement relative to $x = 100$ mm is used.

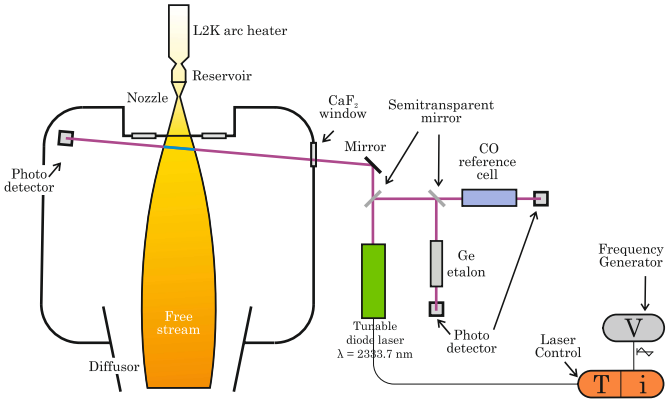

(a) TDLAS conceptual scheme

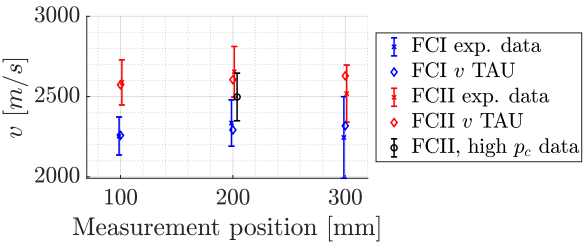

(b) Flow core velocity measured with TDLAS

Figure 3.4: TDLAS setup and results, from [110]

3.3.2 Particle Image Velocimetry (PIV)

As highlighted in [53, 84, 86], particle-induced erosion strongly depends on particle momentum and kinetic energy. Therefore, determining particle velocity represents a fundamental step toward characterising the key particle properties that govern erosion phenomena on heat-shield materials, under particle-laden, high-enthalpy flow conditions. For this purpose, a bi-dimensional (2D)-two components (2C) PIV setup was implemented. Due to the significant lag existing between particle and flow velocities[3], these measurements should not be interpreted as representing the *flow* velocity: in other words, PIV is not employed as a flow diagnostic technique, but rather as a tool to characterise the average *particle* velocity. This choice reflects the rationale behind particle selection: the seeded particles were chosen for their relevance to Martian entry conditions, rather than for their ability to perfectly follow the flow[4].

Hardware Two slightly different experimental setups were used for different purposes of this study, namely:

- The free-stream (FS) setup (figure 3.5) was used to measure L2K's free-stream flow velocity and particle velocity, and to characterise peculiar particle flow properties.
- The shock-layer (SL) setup (figure 3.6) was used to measure particle velocity in the vicinity of cork samples, and to demonstrate the feasibility of materials' thermal response studies, by means of recession measurements, IR thermography, and in-depth temperature measurements.

The results obtained with the FS setup are presented in section 4.1, while the ones obtained with the SL setup are presented in sections 4.2 and 4.4, and chapters 5 and 6.

The coordinate system is equal for both setups, and it is defined as follows: the x-axis coincides with the nozzle symmetry axis, it originates at the nozzle exit, and x-values are positive downstream (toward right, referring to the picture); the y-axis defines the transversal direction, it originates on the flow axis, and y-values increment toward the top of the wind tunnel; both axes belong to the laser sheet plane. In both cases, the scientific complementary metal–oxide–semiconductor (sCMOS) is represented on a wrong plane for schematic visualisation purposes only; same for the particle injection, which happens on the horizontal mid-plane of the settling chamber. In practice, both the seeding generator and the sCMOS camera are positioned in the xz-plane.

The seeding generator described in section 3.1 inserts particles in the L2K flow upstream of the nozzle expansion. A programmable timing unit (PTU) synchronizes the laser

[3] Velocity lag between flow ad particles is due to the flow regime, which is a rapidly accelerating/expanding nozzle flow.

[4] As demonstrated in [85], micrometric particles in the L2K facility operate within a rarefaction-dominated regime, analogous to that encountered during Martian atmospheric entry.

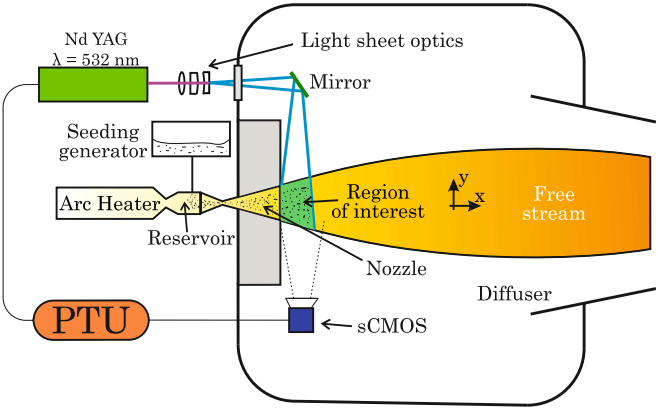

Figure 3.5: Experimental setup for free-stream studies, FS. The reported axes originate on the flow axis, at the nozzle exit location. In practice, both the seeding generator and the sCMOS camera are positioned in the xz-plane

pulses with the camera. The camera records two consecutive frames separated by a defined interframe time, while the laser pulses illuminate the particles at a specified pulse separation Δt within those frames, enabling calculation of particle displacement and velocity[5]. The process can be repeated with a frequency dependent on hardware characteristics. The two subsequent PIV images are then processed with cross-correlation algorithms to obtain an average velocity within the selected interrogation window (IW), i.e. the pixels of the PIV result. A comprehensive description of PIV experimental technique can be found in [95].

One dual-cavity neodymium-doped yttrium aluminium garnet (Nd:YAG) laser (Quantel Big Sky) was used as light source, with wavelength $\lambda = 532$ nm and 15 Hz repetition rate. The selected pulse separation time is $\Delta t = 1$ μs. With an expected particle speed of about 2 km/s from [110], and with the chosen pulse separation of 1 μs, the expected particle displacement between two frames is 2 mm. The time difference between two adjacent laser pulses was monitored with an oscilloscope, that highlighted high time stability and a variation of less than 0.1%: the average measured time difference between two pulses is (1000 ± 0.5) ns. The light beam was focused on the flow axis and transformed into a light sheet with a cylindrical lens. The light sheet crosses the L2K flow vertically, with the nozzle axis belonging to the light sheet plane. In other words, the laser sheet plane is defined by the x and y axes. Its thickness is approximately 1 mm. One LaVision imager

[5]The pulse separation is too short to take more than two subsequent pictures in these supersonic conditions, with the used hardware.

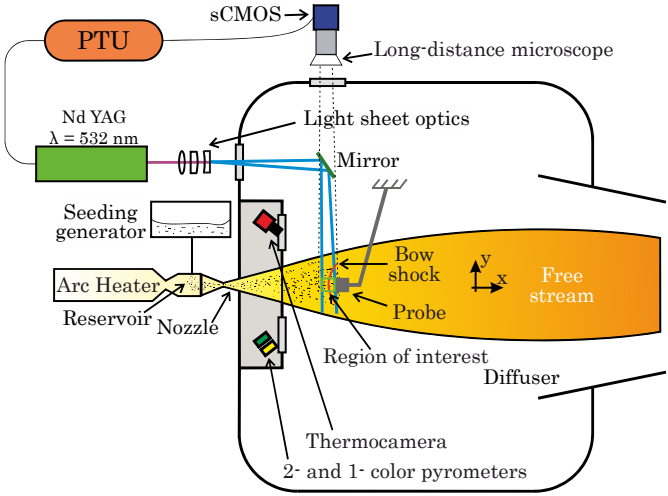

Figure 3.6: Experimental setup for shock-layer studies, SL. The reported axes originate on the flow axis, at the nozzle exit location. In practice, both the seeding generator and the sCMOS camera are positioned in the xz-plane

sCMOS camera was used, with a 6.5 μm pixel size, and a 2560 × 2160 px^2 maximum resolution. The imager observes the light sheet plane perpendicularly. The minimum achievable interframing time is 120 ns.

The hardware of the two PIV setups presented in figure 3.5 and figure 3.6 differ in camera positioning and alignment, camera optics, laser sheet location and the presence of samples in the region of interest. In particular, for FS-PIV:

1. The light sheet is generated with a cylindrical lens with f = - 50 mm. It illuminates the region downstream of the nozzle exit, from the nozzle exit to—at least—80 mm downstream.
2. The camera is positioned inside the test chamber in a cooled pressurised steel box with optical windows.
3. A narrow-band filter is positioned between the sensor and the objective, with full-width at half-maximum (FWHM) of 2 nm around 532 nm.
4. The "short side" of the camera (2160 px) was positioned parallel to the nozzle axis, to picture the widest illuminated region. Two objectives were used, providing different resolutions:

a. *50 mm objective*: the "long side" of the camera captures the entire nozzle exit diameter, allowing visualisation of the full flow field at the nozzle exit. Specifically, the long side spans 210 mm, resulting in a camera field of view of 210×177 mm^2. This setup provides a spatial resolution of 12.2 px/mm and, with the chosen pulse separation, an expected particle displacement of 24.4 px. Only a rectangular part (crop) of the image is used for PIV evaluation, since the light sheet is only approximately 80 mm large, and the laser sheet does not illuminate the whole field of view.

b. *100 mm objective*: the camera orientation is the same as with the 50 mm objective. In this case, the camera captures 90×75 mm^2, granting a resolution of 28.5 px/mm, and an expected particle displacement of 57 px with the selected pulse separation. The whole image is used for PIV evaluation.

For SL-PIV:

1. The light sheet is generated with a cylindrical lens with f = - 200 mm. It illuminates the region downstream of the nozzle exit, from approximately x = 260 mm to x = 315 mm.

2. The camera is positioned outside the test chamber for easier access.

3. A narrow-band filter is positioned in front of the objective, with FWHM = 5 nm around 532 nm.

4. A long-distance microscope (LDM) is used to provide a high resolution at a distance higher than 1.5 m. The "short side" of the camera (2160 px) is positioned parallel to the nozzle axis. In this way, the "long side" of the camera can picture 58.0 mm, being able to capture both the whole bow shock in front of the probe and the region around the shoulder of the sample. With this objective, the field of view is thus 58.0×49.1 mm^2, the image resolution is 44.0 px/mm, and the expected particle displacement is 88 px with the selected pulse separation. The whole image is used for PIV evaluation.

While the pixel sampling described above represents the nominal spatial resolution in pixels per millimetre, the true optical resolution is limited by diffraction, lens quality, and other aberrations. According to the Rayleigh criterion, the diffraction-limited resolution is approximately $0.61\,\lambda/\mathrm{NA}$, where λ denotes the laser wavelength [95]. The numerical aperture NA of the 50 mm and 100 mm objectives can be expressed as $\mathrm{NA} \approx (2f_{/\#})^{-1}$, with $f_{/\#}$ values of 2.8 and 2, respectively. For the LDM, the NA is obtained from the manufacturer's lookup tables based on the magnification M = 0.286, calculated as the ratio of the sensor pixel size (6.5 μm) to the object-space pixel size (22.7 μm/px), yielding NA = 0.0154. Based on the 532 nm laser wavelength and these numerical apertures, the diffraction-limited optical resolutions are approximately 1.81 μm, 1.30 μm, and 21 μm for the 50 mm, 100 mm, and LDM systems, respectively.

According to the Nyquist criterion, a particle must cover at least two pixels to be optically resolved. With the stated objectives, individual 1 μm particles cannot be resolved due to both digital sampling and diffraction-induced blur. Thus, the PIV system is limited by a combination of diffraction and pixel resolution, rather than by the number of pixels per millimetre alone. Nevertheless, the chosen camera sampling and optical configuration allow particle displacements to be measured with sufficient accuracy for the intended experiments.

Test Campaigns Testing times are limited by the amount of particles stored in the seeding generator before each test. The results of several test campaigns—whose main parameters are summarised in table 3.3—are reported in this work. Tests named FS and SL refer to the setups of figures 3.5 and 3.6 where free-stream particle velocity and shock-layer particle velocity were measured, respectively. The two names thus indicate a different region of interest of the PIV system. During the first campaign FS1, 1350 double-frame PIV images were taken for FCI^P, and 1500 for FCII^P, with testing times of about 90 s. A 2.8/50 mm objective was used for the sCMOS camera. In the second campaign FS2 a 2/100 mm objective was used to observe a zoomed region on the flow axis and increase spatial resolution. For the second test campaign, 2000 pictures were taken for both FCs, with testing times of approximately two minutes. In the third experimental campaign SL, a LDM was used to achieve better resolution and measure the particle velocity around cork samples for approximately one minute (i. e. 900 images). The choice of IW size was driven by seeding density. Consequently, the IW in FS2 is larger than in FS1. For SL, a narrower light sheet combined with a more magnifying objective allows visualisation of smaller particles, effectively increasing the apparent particle density. As a result, even though the field of view is smaller for SL compared to FS2, the IW size remains the same.

Table 3.3: Test matrix

Test n.	Objective	FC	N. Images	Final IW size
FS1	2.8/50 mm	I^P II^P	1350 1500	64 × 64 px^2
FS2	2/100 mm	I/II^P	2000	96 × 96 px^2
SL	LDM	I/II$^{P/nP}$	900	96 × 96 px^2

Data processing is performed with the DaVis software's built-in functions [61]. The raw images are first transformed from pixels to millimetres thanks to the calibration image taken before the experiments. While the first frame of the FS-PIV image generally has good quality, the second frame suffers from its longer exposure time, capturing higher levels of noise due to the glowing flow and the bright agglomerates. The long exposure time is physically limited by the sCMOS sensor's readout time. In SL-PIV this issue is absent. Nevertheless, all images are then pre-processed to remove the background

and normalise the particles' signals with DaVis built-in function "Image Preprocessing", based on local averaging, and normalisation: this step included background removal to eliminate stationary noise, subtraction of a sliding minimum to enhance moving particle contrast, and sharpening to improve edge definition. The two setups present significant differences regarding the next processing steps, which are explained in the following sections.

FS-PIV Processing Strategy No significant reflections were observed that could compromise the PIV processing, and no masking was required. The standard DaVis built-in multi-pass PIV algorithm was used, with window shift, thanks to the uniformity of the expected particle velocity field, and due to the large expected particle displacement (approximately 24.4 px). The initial and final IW sizes of the multi-pass algorithm were set to 256×256 px^2 and 64×64 px^2, respectively, with 50% overlap. The vector validation process was tuned to eliminate all the vectors evaluated in the non-seeded regions of the images, deleting data computed on the noise. Non-valid vectors were strongly removed and iteratively replaced for each image. An exemplary instantaneous PIV result of a single frame (frame n. 985, FS1, FCI^P) is reported in figure 3.7. The instantaneous result shows a few windows where the evaluated velocity vector is non-valid—the non-valid IW is automatically discarded by the program. The velocity field is homogeneous in the core and one can clearly observe a velocity decrease in the regions corresponding to the shear layer and boundary layer of the nozzle, in the upper and lower part of the image.

SL-PIV Processing Strategy The SL-PIV setup focuses on a region of interest that encompasses free-stream, shock layer and sample's shoulder region. The challenge of performing a PIV evaluation in this region lays in the different types of particles that can be observed and in their very high dynamic range. The particles can come from different locations, like the settling chamber of the wind tunnel (where they are inserted) or the sample itself (due to ablation phenomena). One can find:

- **Nominal particles** looking like the control sample (shown later in section 3.3.4), coming from the settling chamber: they are the fastest particles, as they have the smallest size.
- **Particle agglomerates** coming from the settling chamber: they travel at lower velocities compared to nominal particles. They have no upper limit in size, and can be big chunks.
- **Particle droplets** coming from the settling chamber: they are nominal particles which experience a phase change.
- **Agglo-molten particles** coming from the settling chamber: they are agglomerates of particles which experience a phase change.

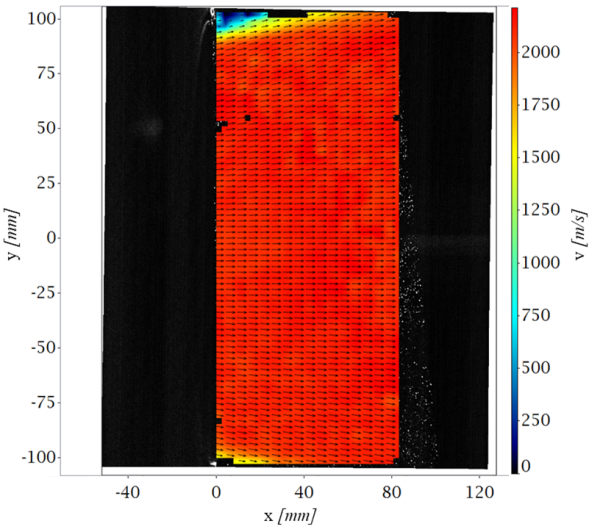

Figure 3.7: Randomly selected PIV frame (number 985) from FS1, FCI^P

- **Rebounded particles** coming from the settling chamber: they "bounce" on the sample and their size is unknown, since what happens after impact is undefined. They can be seen moving in the opposite direction of the flow, usually with low velocity, and can cross the bow shock. They can be large, dragging the PIV evaluation towards the computation of negative results.
- **Eroded particles** coming from the sample due to erosion processes.
- **Outgassed particles** coming from the sample and being pushed in the counter-flow direction by the outgassing phenomenon.

Note that the first four kinds of particles can be seen in the FS-setup as well. In addition to the different nature of the particles, different regions of the analysed images can be defined, as sketched in figure 3.8. From upstream to downstream one can find:

- *Free-stream*: it has very high velocity, and it counts mainly nominal particles, and eventually agglomerates, droplets and rebounded particles.
- *Bow shock*: it is the narrow region where a discontinuity of the flow physical properties happens, and it is where the nominal particles start to slow down. In this region a larger amount of rebounded/eroded particles can be found.

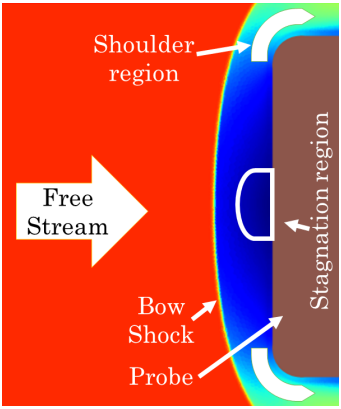

Figure 3.8: Flow field features

- *Shock layer (including boundary layer)*: it is the region downstream of the bow shock; here, all types of particles can be found. In the shock layer one can observe:
  - *Stagnation region*: it is the region right in front of the probe very close to its axis, in the vicinity of the stagnation point where the flow velocity is zero.
  - *Shoulder region*: it is the region across the corner of the sample, where the particles re-accelerate following the expanding flow.

Different zones present different characteristic velocities: a trade-off had to be made on the choice of the pulse separation Δt: the expected particle displacement in the free-stream of 2 mm between frames corresponds to roughly 88 pixels, which can be considered unnecessarily large in the PIV community; thus, the Δt could be decreased to the lower limit of the hardware (120 ns). Since large velocity gradients are expected across the bow shock (from more than 2000 m/s to subsonic velocities), a sufficiently large Δt is needed to adequately resolve the relatively low particle velocity. Therefore, the pulse separation used also for FS-PIV is selected ($\Delta t = 1$ μs).

In addition, the broad range of velocities generates regions with different particle seeding (considering constant particle mass flow rate)—i. e. dense seeding in the shock layer and sparse seeding in the free-stream. The very broad nature and characteristics of the observed particles (in terms of size, velocity and seeding density) pose a big challenge to the PIV evaluation, whose working principle is based on the cross-correlation algorithm within IWs. The most refined evaluation strategy would require a variable IW size,

window deformation, exclusion of rebounded particles in the bow shock and in the free-stream, multi-pass, tuned vector validation, and averaging. In the following, a simpler evaluation strategy is presented.

When PIV is performed in the vicinity of a surface (in this case the cork sample), the surface needs to be excluded from the result by masking. From now on, pre-masking means computing the PIV result on a grid that excludes the non-relevant regions (like the cork sample), while post-masking means evaluating the PIV result on the whole image, and only then excluding the results computed on irrelevant regions. It is observed that the PIV algorithm can break in the free-stream, due to the high particle displacements of about 90 px, and the relatively low seeding density: without adequate measures, the PIV algorithm can sometimes compute null velocities, where a 2 km/s velocity is expected. On the other hand, the shock region is easily computed, as its seeding density is higher and its particle displacement lower. To increase the algorithm's robustness in the free-stream, a constant initial window shift of 100 px in the direction of the main flow is given. However, such a high constant window shift applied to the whole flow field can create problems on the resolution of the shock layer. In fact, depending on the used computation strategy, the shock layer might shrink in the final result: the cross-correlation algorithm of PIV is influenced by the initial large window shift, that pushes the algorithm towards the computation of higher velocities in the shock layer. This effect is not observed if the post-masking strategy is chosen over the pre-masking one. For these reasons, the PIV evaluation based on *multi-pass* with *window shift* and final averaging is performed in the whole image. Subsequently, the irrelevant zones are excluded (*post-masking*), namely the zone corresponding to the probe, the zone below the probe and a small region in the bottom part of the image that is not illuminated by the laser. The initial and final IW sizes of the multi-pass algorithm are set to 512×512 px^2 and 96×96 px^2, respectively, with 50% overlap. The choice of window size is based on the seeding density of the free-stream. More resolved analysis could be performed in the shock layer where the seeding density is higher.

In addition to these measures, a strict validation strategy must be used to avoid computing non-physical results in a region that presents such high velocity gradients: all vectors with correlation values below 0.3 are excluded, and vector validation based on the 5×5 median filter with iterative replacement (implemented in DaVis [61]) is used, which is capable of rejecting groups of spurious vectors. In particular, a $2\times$ median filter with iterative replacement was applied; vectors differing from the local average by more than 2 standard deviations were removed, with re-insertion if within 3 standard deviations. Vectors outside an allowed velocity range were removed to discard non-physical negative velocities in the free stream. To avoid smoothing strong gradients introduced by the step-like velocity change over a bow shock, no interpolation is used in empty spaces. Due to the stringent criteria used by the validation algorithm, it is rare to find a picture where all vectors are computed: the results are in the end averaged over the whole dataset, to obtain a smoother result. Note that the sample geometry varies during the test, due to

expansion, charring, ablation and erosion. Thus, the average process might introduce errors on the shock-layer velocity (and geometry) determination. However, this error is considered acceptable due to the relatively short test duration, which results in a negligible thickness evolution. It is worth noting that the sample exhibits slightly greater evolution in FCII^P compared to FCI^P.

General Considerations As this is the first study reporting PIV in an arc-heated wind tunnel for TPS testing, it is worth spending some lines on general considerations and data quality. Contrarily to some experimental activities in other hypersonic wind tunnels, the depressurisation process of the test chamber does not compromise the stability or alignment of the laser line, which simplifies the calibration procedure. This is due to the robust structural design of the L2K facility and its relatively low mass flow rates. Also, the camera's focus is not affected by the chamber depressurisation and no vibrations are observed. The particle injection inside the hot reservoir did not cause any flow instability. Particle seeding was provided for up to two minutes, resulting in varying seeding quality: some images had uniform coverage, some had only localized regions of sufficient seeding, and others contained very few particles. The choice of vector validation and filtering parameters was guided by measurable quality criteria, including correlation peak height, local particle density within interrogation windows, and consistency with neighbouring vectors. Parameters were selected to ensure physically consistent velocity fields in regions with sufficient seeding, while vectors in poorly seeded regions were removed during post-processing. It should be noted that post-processing cannot recover velocity information in interrogation windows lacking sufficient particles.

The high reservoir temperature can cause the particles to melt, and stick/agglomerate together after colliding (agglo-melting). The agglomeration process is stochastic, and it can be mild (if only few micrometric particles agglomerate) or severe, if the agglomerate is big enough to keep glowing while travelling through the nozzle and test chamber: in this case, the cooling time of the agglomerate is longer than the time that the agglomerate takes to travel through the test chamber. The glowing agglomerates can be observed in the frames of the video monitoring of the wind tunnel tests (figure 3.9), as well as in the second frame of the FS-PIV acquisition (figure 3.10a, right), as they are characterised by long exposure times: the glowing agglomerates appear as bright stripes in such frames. They cannot be used for PIV evaluation and they affect data quality, since they can easily reach the same intensity of isolated particles. These stripes are not seen in the SL setup (figure 3.10b), which uses a higher f for the generation of the light sheet, causing a stronger illumination of the particles, thus a higher signal-to-noise ratio (SNR). The sample profile is highlighted by the laser sheet on the right side of the pictures; illuminated particles are visible in the free-stream and in the shoulder region. Agglomerates are not visible. Agglomerates' brightness cannot be sufficiently reduced in the pictures, but particles' SNR can be increased by: increasing laser output power; using cylindrical lenses with higher f; using higher camera aperture. In fact, differently from particles which are

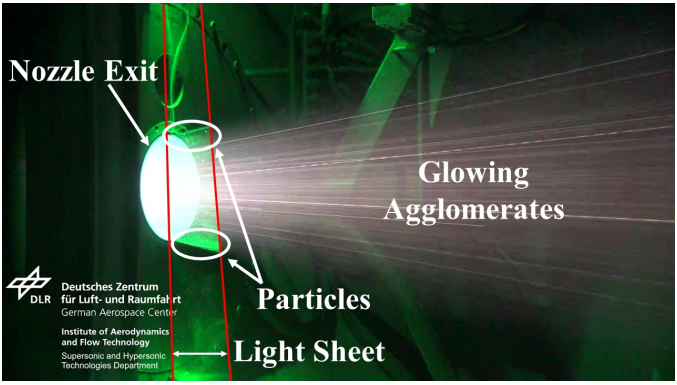

Figure 3.9: Wind tunnel test frame from video monitoring (FS setup)

visible on the light sheet plane only thanks to laser light scattering, glowing agglomerates can be seen on the whole 3D nozzle flow field; by using higher camera aperture, the depth of focus becomes shorter, thus lowering the out-of-plane agglomerates' signals.

The L2K flow is glowing itself, due to its high-enthalpy and chemical reactions. The glowing flow reduces the second frame's quality, due to its long acquisition time. Narrow-band filters centred on laser's emission wavelength must be used. The use of the LDM helps mitigate this issue.

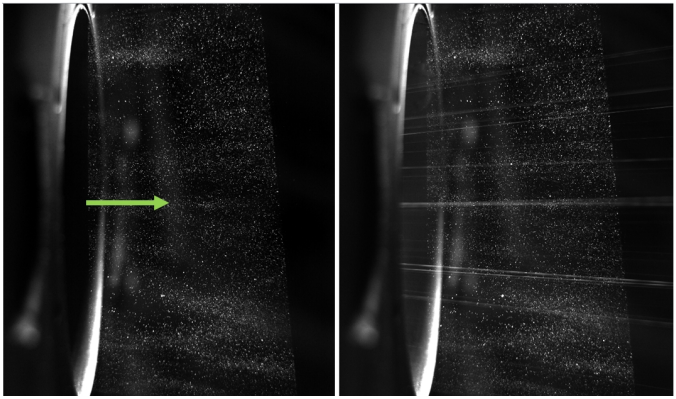

(a) FS setup

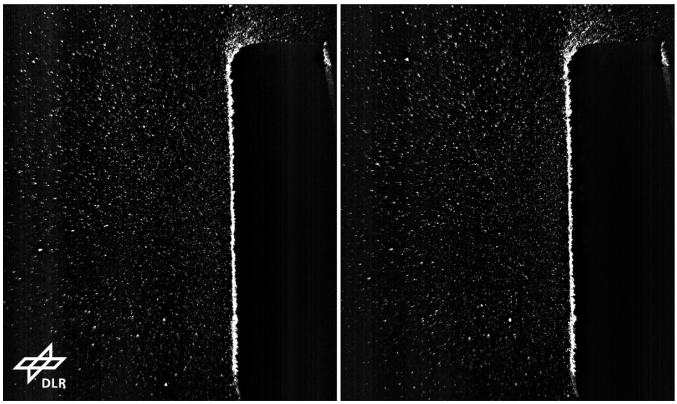

(b) SL setup

Figure 3.10: Generic PIV raw images of the two setups, showing first frame (left) and second frame (right). The flow comes from the left, as highlighted by the green arrow

3.3.3 Particle Count vs Erosion Rate

Monitoring the temporal evolution of the number of particles reaching the sample provides several advantages. In particular, it allows assessing whether the particle flux is steady or intermittent, thereby offering additional insight into particle flow characterisation, and enables correlation between particle count and time-resolved surface erosion measurements.

Counting Strategy Particle counting was performed on the first frame of the SL-PIV raw data for all FCs^P. The counting procedure was restricted to a rectangular region of interest (RoI) located upstream of the sample within the wind tunnel free stream, thereby excluding the shock layer. The RoI has a width of $\Delta x_{\mathrm{RoI}} = 17.8$ mm and a height of 34.9 mm. This region was selected based on the presence of high-quality raw images, favourable illumination conditions, and sufficient distance from the sample surface to minimise the inclusion of particles originating from material erosion. Particle detection was carried out using the built-in *Particle Counter* function in DaVis, after pre-processing the raw PIV images as follows:

1. Cropping the first PIV frame according to the selected RoI.
2. Setting all values below a threshold intensity to 0 (the threshold choice is based on the noise value).
3. Applying a 2-pixel Gaussian sliding filter to regularise particle image shapes.

In chapter 6, the particle count for each test case is analysed and used to compare the two FCs^P, as well as to relate the particle count n_{p} to the erosion rate contribution $\frac{dY^e}{dt}$. The latter is directly linked to the particle flux, assuming constant particle and material properties, as demonstrated in section 2.1.5:

$$\frac{dY^e(t)}{dt} = c_{10}\frac{dN_p(t)}{dt} \tag{2.14}$$

The particle flux $\frac{dN_p}{dt}$ can be related to n_{p} and to Δt_{RoI}, assuming homogeneous velocity field and constant $\mathbf{v}_p$; this assumption is reasonable as the RoI lays in the free-stream. Furthermore, assuming that the particle seeding is homogeneous (this is reasonable thanks to the reduced size of the RoI), the particles counted in the light sheet can be used to obtain the overall particle number in any wanted volume in front of the probe simply by scaling with a constant c_{11}, dependent on the laser sheet volume:

$$\frac{dN_p}{dt} \approx c_{11}\frac{n_{\mathrm{p}}(t)}{\Delta t_{\mathrm{RoI}}} = c_{11}|\mathbf{v}_p|\frac{n_{\mathrm{p}}(t)}{\Delta x_{\mathrm{RoI}}} \tag{3.1}$$

According to the mentioned assumptions, all quantities above except n_p are constant. Substituting equation (3.1) in equation (2.14), and collecting all constants in one single proportionality factor A, one finds:

$$\frac{dY^e}{dt} = An_\mathrm{p}(t) \tag{3.2}$$

A depends on the particle- and material-related properties, particle velocity, and laser sheet volume. Combining equation (2.13) and equation (3.2) one finds:

$$A = c_6 c_{11} \mathbf{v}_p{}^{c_7+1} d_p{}^{c_8} \rho_p{}^{c_9} (\sin\alpha)^{c_5} \Delta x_\mathrm{RoI}^{-1} \tag{3.3}$$

where c_i are the model's constants.

In summary, the erosion rate is proportional to the particle count, assuming constant and homogeneous particle velocity, constant particle properties (density and size), constant material properties, homogeneous seeding, and quasi-perpendicular impact. The proportionality factor A depends in turn on the particle momentum or kinetic energy ($\mathbf{v}_p$, d_p, ρ_p), on the sample material (c_i), and on the geometric settings (α, Δx_RoI, c_{11}).

Limitations of the Current Setup As stated in the previous section, particle images are dominated by diffraction-induced blur, with a characteristic size comparable to the Airy disk diameter, and are further undersampled by the camera sensor. Individual particles cannot therefore be optically resolved, and their recorded signatures correspond to diffuse intensity spots rather than distinct, separable objects. Consequently, the particle count must be regarded as indicative only, and its interpretation as particle flux relies on the strong assumption that each detected particle image corresponds to a single particle, rather than to agglomerates or overlapping particle images.

Moreover, the acquisition frequency needed to count all particles passing through the RoI is $\nu^* = 1/\Delta t_\mathrm{RoI}$, where Δt_RoI is the time it takes particles to traverse the whole region of interest. According to the RoI's location and its small height, it is reasonable to assume that the vertical component of particle velocity is negligible; therefore:

$$\Delta t_\mathrm{RoI} = \frac{\Delta x_\mathrm{RoI}}{|\mathbf{v}_p|} \tag{3.4}$$

Considering particles moving at approximately 2 km/s, the necessary acquisition frequency ν^* is in the order of 100 kHz. The result is therefore severely under-sampled, as the laser's repetition rate is 15 Hz. In addition, the particle count $n_\mathrm{p}(t)$ represents the particles that pass through the laser sheet only, and no information is known about particles outside the laser sheet.

The measured particle count is therefore interpreted as an indicative representative of the overall particle flux, based on the assumption of a spatially homogeneous particle

distribution and a temporally constant flux over each sampling interval, as required by the undersampled nature of the measurement. In addition, treating each detected particle image as representative of a single particle introduces further uncertainty into the methodology. Future improvements could involve the use of higher magnification optics combined with larger numerical apertures, enabling resolution at the micrometre scale. Alternatively, advanced diagnostic techniques such as phase-doppler particle analyser (PDPA) or L2F may be employed to provide more reliable measurements of particle flux at a given location without requiring optical resolution of individual particles.

3.3.4 Particle Collection

Particles are collected with the double-sided high-grade copper tape used for electron microscopes. A water-cooled stagnation probe made of copper is used as support for the copper tape strip, which is positioned inside the flow at the same location of cork samples. The cooled support has the same geometry of the cork samples described before. To collect the particles, the probe is moved inside the particle-laden flow with a shield. Once it reaches the axial position, the shield is quickly removed (tenths of a second), and the collection process begins. After a residence time of 2 seconds, the shield is positioned again in front of the sample, and the probe is then removed from the flow. The residence time inside the flow is limited by the high heat flux: it is so intense in FCII^P, that the collection tape melts if the probe is left inside for more than 2 s. The same method can be used for longer times in FCI^P, that provides lower heat flux.

Once collected, specimens are observed with SEM imaging, and energy-dispersive X-ray spectroscopy (EDX) analysis is performed on every site to understand and verify the chemical composition of the observed object. A control sample of particles before the injection in the wind tunnel is presented in Figure 3.11. The observation of the control sample is important for the comparison with the samples collected in the stagnation point, helping to understand physical phenomena that the particles are subject to, during their flight in the wind tunnel and after impact. In the control sample, one can observe the particles' uniform size of approximately 1 μm and their disk-like shape.

Particle collection is considered here a valuable and straightforward method because it provides important information on particle morphology and history (the passage in the high-temperature reservoir of the wind tunnel, the possible phase change and agglomeration, and the impact on the probe), and it is simple to implement within the current setup. However, the described technique generates a high thermal and mechanical load on particles at impact, causing a morphological change, which can be due to melting, agglomeration, sintering, or disintegration. Moreover, depending on the Stokes number of the particles, they are collected with different efficiency by the probe, depending on their size: small particles can easily follow the streamlines downstream of the bow shock and they will tend to pass over the probe, while bigger ones will most likely impact

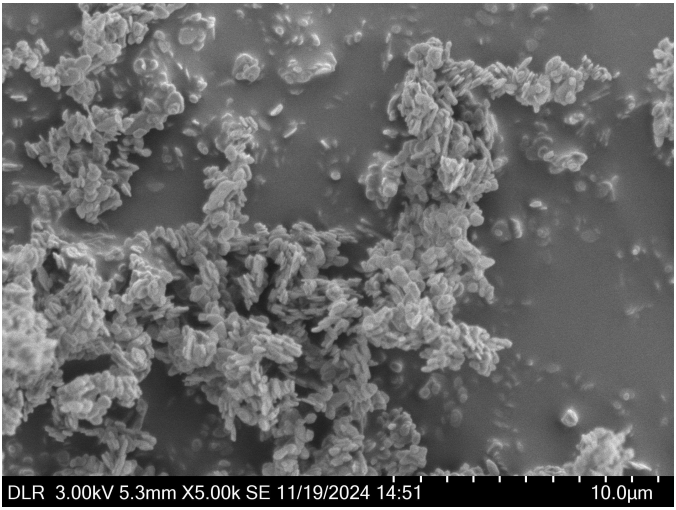

Figure 3.11: Magnesium oxide particles before testing

the probe, getting collected by the adhesive strip. For these reasons, this technique is intended for qualitative analysis only: while its intrusive nature limits the ability to perform precise estimations of particle size distribution, it still offers useful insights at this stage, requiring minimal effort while yielding meaningful information about the particles.

3.3.5 Overall Thickness Evolution Measurements

The term *thickness evolution* or simply *evolution* is used in this manuscript to address the combined effect of material swelling and surface recession caused by ablation processes. 3D scans of samples' height (or thickness) H are taken before and after each test with the 3D-profilometer *VR-5000* from Keyence [56]. The measurement is obtained by laying the sample vertically on a common reference surface[6]. The overall evolution is obtained by subtracting the sample's height after the test H_{end} to the one before the test H_0:

$$E_{end} = H_0 - H_{end} \tag{3.5}$$

In this way, the evolution value is positive if the sample recesses, and negative if it swells. This measurement does not resolve the time dependency of the evolution.

[6]According to figure 3.2a, the height—or thickness—in the centre of the sample's surface is 40 mm.

3.3.6 Laser-sheet Profile Tracking (LPT)

The samples time-resolved evolution was measured with a technique based on image processing, which was developed in this work—from serendipity—by using PIV on samples and seeing that the reflected laser sheet from their surface could be tracked along time to analyse recession. The signal exploited by this technique corresponds to the profile P_r, that is created by the intersection of the sample with the laser-sheet plane containing the sample's symmetry axis. This profile coincides with the brightest zone of the image, as it comes from laser diffusion from the sample's surface, ensuring high SNR. By comparing $P_r(t)$ with $P_{r,0} = P_r(t_0 = 0\,\mathrm{s})$, one can measure the thickness evolution on the sample's mid-plane. The mentioned technique is therefore called laser-sheet profile tracking, or LPT. In figure 3.12, the raw data from a test are shown at two different time instants. On the left, the probe is shown at $t = t_0 = 0\,\mathrm{s}$, and on the right at $t_{end} = 60\,\mathrm{s}$, in FCII^{nP}. The flow enters from the left. The sample profile, highlighted by the laser sheet, clearly shows that the profile has evolved over time.

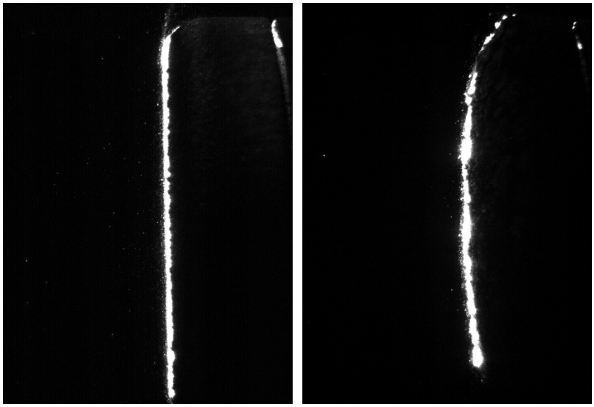

Figure 3.12: Raw images at two different time instants, $t_0 = 0\,\mathrm{s}$ (left) and $t_{end} = 60\,\mathrm{s}$ (right): one can appreciate the evolution of the reflected laser profile

Hardware The pictures collected for PIV were used for this purpose. Therefore, the hardware setup is the same used for SL-PIV[7] (section 3.3.2), including Nd:YAG laser, sCMOS camera, LDM, PTU, and narrow-band filter. Thanks to the setup geometry, the laser always illuminates the vertical mid-profile of the sample, regardless of how

[7]Note that PIV records a double frame. Only the first of the two frames is used for this analysis.

evolved its shape is, during the test. As for the considerations reported for the PIV setup, the depressurisation process of the test chamber does not compromise the stability or alignment of the laser line. The radiation from the L2K flow can reduce the raw data quality, if the camera's acquisition time is long enough to build up a bright halo on the image: the choice of a sufficiently short acquisition time (10 μs in this test series), along with a proper narrow-band filter centred on laser's emission wavelength is crucial. The camera's acquisition time needs to completely capture the laser shot, to obtain the best SNR. One should also consider that whenever particles are present in the flow, they disturb the profile's recognition algorithm as described later in section 5.3.

Execution and Processing Before the test, a calibration target is positioned on the laser-sheet plane, to allow the transformation from pixel space to metres space: the calibration target plane and the light sheet plane must coincide to transform the image correctly. During the test, the camera records multiple pictures at a defined frame rate, building up a time-series. The system's frame rate is 15 Hz, thus 900 frames per minute. Later, the images are transformed with the calibration map, and processed.

For each image, an algorithm finds the light profile P_r highlighted by the laser light sheet, and tracks it along the time series, developing a time-resolved location of P_r, as shown in figure 3.13. The laser sheet profile is determined using an intensity-weighted detection algorithm. For each pixel row in the vertical direction y, the intensity values along the horizontal direction x are considered, and values below a predefined threshold are set to zero to reduce noise. The algorithm then computes the intensity-weighted centroid of the remaining non-zero values, which is assigned as the sheet position for that row. In other words, the laser sheet's axial position is obtained as a function of vertical position and time, $x = P_\mathrm{r}(y,t)$. This method effectively captures the sheet profile while suppressing low-intensity background fluctuations.

Thanks to the experiment setup construction, the profile displacement in x coincides with the profile evolution, which is t- and y-dependent. To evaluate the local evolution E, the profile at the beginning of the test ($t_0 = 0\,\mathrm{s}$) is subtracted from each profile:

$$E(y,t) = P_\mathrm{r}(y,t) - P_\mathrm{r}(y,t_0) = P_\mathrm{r}(y,t) - P_{\mathrm{r},0} \tag{3.6}$$

$P_{\mathrm{r},0}$ is evaluated as the average of the first five recorded profiles ($t \leq \frac{1}{3}$ s, according to the frame rate of 15 Hz), on which a spline regression is performed to obtain a continuous profile function in y. This procedure makes sure that no y location of $P_{\mathrm{r},0}$ presents any blank value, or not-a-number (NaN), to avoid the generation of unnecessary holes in the results when equation (3.6) is applied to the data. Note that negative evolution values identify zones where the sample has swollen more than it has recessed, whereas positive evolution values identify zones where the sample has recessed more than it has swollen, in agreement with the overall recession measurements.

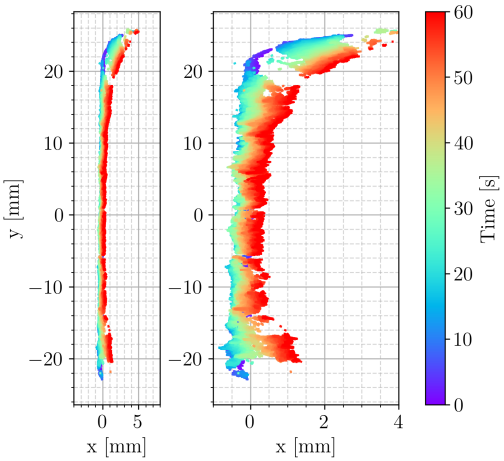

Figure 3.13: Mid-plane profile evolution, colour-ordered over time. The two pictures present the same data, one with equal axes aspect ratio (left), and one with stretched x to better appreciate the profile evolution

Discussion and Error Sources The advantages of LPT are multiple: its hardware can be used to measure different physical quantities, such as in this study; it requires one only camera, being much faster to set up with respect to DIC-based techniques; it measures evolution always on the same mid-profile of the sample surface, contrarily to laser-dot maps that experience a spatial drift of the dots; it is non-intrusive, contrarily to fibre-optic techniques. Its disadvantages are: measurement accuracy might be dependent on the laser profile thickness, it does not give spatially-resolved 2D results being limited to one-dimensional (1D) resolution, and it requires developing an algorithm for image processing to optimally track the probe profile.

The systematic error sources of this experimental technique are here described and quantified:

- *Mechanical vibrations*: the wind tunnel might generate vibrations that cause optics misalignment and image shift. To assess this, the sample support structure was monitored in the raw data for any image displacement before, during, or after the tests. Owing to the massive structure of the L2K wind tunnel and its relatively low mass flow rate, no vibrations were detected. Therefore, no systematic error is introduced by mechanical vibrations.
- *Laser and optics misalignments*: the laser line-of-sight and the optics may randomly

misalign due to mechanical vibrations and instabilities. The laser position was carefully checked before each test to ensure correct alignment with the measurement region. During the experiment, the reflected spot on the stationary sample holder was monitored to verify that the laser remained in position. Combined with the absence of mechanical vibrations, these measures ensured that no systematic errors were introduced.

- *Pixel quantisation (finite sensor resolution)*: the sCMOS sensor resolution is 44.0 px/mm for this setup section 3.3.2. The location algorithm of LPT is based on the intensity-weighted method, thereby reducing the quantisation error to 1/10 of pixel [24]. The quantisation error is therefore 1/440 mm.
- *Intrinsic calibration uncertainty*: calibration is performed with the DaVis software [61] by third-order polynomial fit, whose error is less than 1.3 pixels for all experiments (i.e. 0.030 mm).

The overall systematic error on the LPT data is therefore 0.030 mm. Beyond systematic errors, the LPT algorithm can introduce a positional uncertainty due to its intensity-weighted profile detection. To control this, any measurement with a standard deviation exceeding 0.3 mm is discarded as an outlier, ensuring that the location error remains below this threshold. The 0.3 mm threshold should be considered a conservative limit, as it is significantly larger than the estimated systematic error and typical measurement fluctuations, ensuring that only clearly anomalous readings are discarded while retaining valid data. By combining systematic error and positional uncertainty, the overall error on the LPT data is therefore less than 0.3 mm.

3.3.7 Temperature Measurements

In addition to the embedded thermocouples mentioned in section 3.2, the IR camera *Optris PI 1M* [81] monitors the whole surface temperature from the front, and one-colour and two-colour pyrometers monitor the surface temperature on the centre of the sample surface. The used one- and two-colour pyrometers are *Maurer*'s *KTRD 1485* [71] and *QKTRD 1485* [70], respectively. The emissivity is set to 1 during data processing for both the IR camera and the one-colour pyrometer, in order to avoid the complexities of material emissivity modelling. This approach provides a lower-bound estimate of the surface temperature, since real material emissivity is less than 1 and would result in higher actual temperatures.

3.3.8 X-rays

X-rays of the samples are made before and after tests to monitor the thermocouples' positions, and check for possible misplacements due to the manufacturing process, or

displacements during testing. Misplacements due to manufacturing are in the order of 1 or 2 mm in the axial direction: due to cork's insulating properties, such a value is not negligible, thus only few tests are directly compared in chapter 5 regarding in-depth temperature data. No thermocouple displacement was observed during tests. Two exemplary X-rays of the same sample before and after the test are reported in figure 3.14. One can observe that, after the test, the sample's front surface has an optically-thinner layer which is caused by the presence of charred and pyrolysed material: X-rays are therefore used to measure the char thickness with image processing.

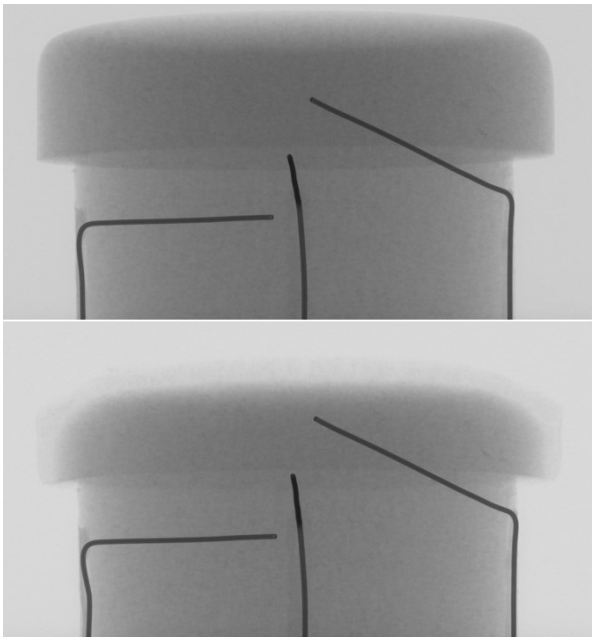

Figure 3.14: X-rays of the sample before (above) and after (below) the test

3.3.9 Qualitative Observations

Several pictures are taken before and after each test to observe the sample's qualitative evolution. Three video cameras record the test from different perspectives and with

different zooms. Pictures of the sectioned samples are taken to assess eventual differences in charring behaviours between different flow conditions and compared with X-rays.

3.4 CFD Setup

Numerical simulations of the wind-tunnel flow can support the flow-characterisation process by providing useful data in a cost-effective manner, provided they are validated against experimental measurements. In addition, the comparison between flow and particle velocity can give meaningful insights in the characteristic physical phenomena of the high-enthalpy particle-laden flow. For these reasons, CFD computations were performed with the DLR-TAU flow solver to evaluate the expected flow velocity of the particle-free flow conditions FCs^{nP}. Moreover, no material response is considered in the simulations. Note that the comparison between CFD and particle velocity field is only valid under the assumption of one-way coupling between the flow and the particles—that is, the flow influences particle motion, but the particles do not affect the flow characteristics.

High temperature effects were considered in the simulations: a chemical model with 11 species and 103 reactions is chosen for the chemical compounds CO_2, CO, O_2, O, NO, N_2, N, C, C_2, CN, NCO. The chemical reaction scheme for the Martian atmosphere is based on [22, 40, 87, 88]. Building on these studies, J. Dubois developed a comprehensive reaction mechanism within the framework of the EU project SACOMAR [31]. In the TAU code, this mechanism is implemented in a simplified form, considering only the electrically neutral species. Simulations are performed in chemical non-equilibrium and thermal equilibrium (only one temperature is considered), in a steady-state flow field and 2D axial-symmetric geometry. The convergence is assured by monitoring the density residual. The simulated flow core velocity of both flow conditions was validated in [110] with TDLAS, and the computed shock stand-off distance δ was validated in previous experimental campaigns without particles.

Two different grids were used for the undisturbed wind tunnel environment, and for the region in the vicinity of the sample. The computational strategy for obtaining both free-stream and shock-layer results is presented here:

1. Free-stream simulations (FS) of the wind tunnel's reservoir, nozzle and test chamber are performed with the structured mesh reported in figure 3.15a.
2. A different grid is used to compute results in the vicinity of samples (SL): the grid has a structured sublayer on the probe surface and three-times adapted unstructured mesh in the free-stream and shock layer. The grid before adaptation and the adapted grid used for the final result are reported in figure 3.15b and figure 3.15c, respectively.

3. The free-stream values are interpolated on the sample grid to generate an initial condition for the SL computation, as well as to define its inflow boundary condition. The interpolation process is performed with a DLR-internal tool, such that the sample surface location represents the test environment, as sketched in figure 3.15a.

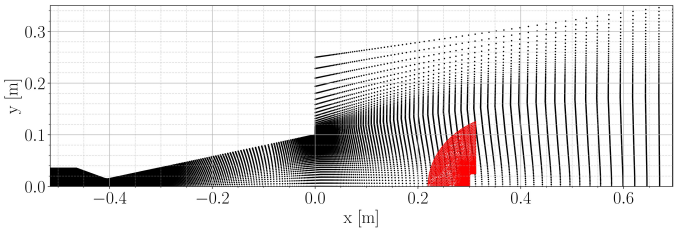

(a) FS grid superposed to SL grid

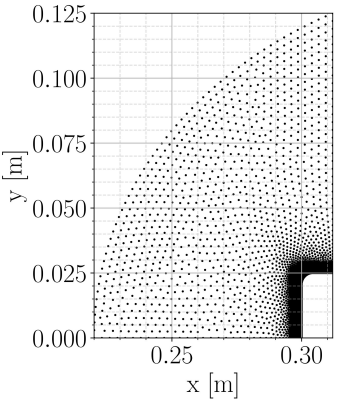

(b) SL grid before adaptation

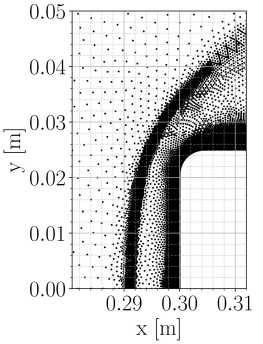

(c) SL grid after adaptation (zoom)

Figure 3.15: Grids used for CFD computations (only nodes are displayed)

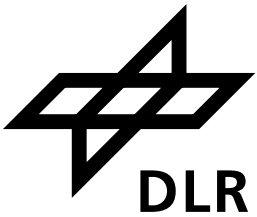
DLR

4 Flow and Particle Characterisation

In this chapter, the free-stream flow velocity and particle velocity are separately measured using TDLAS and PIV, respectively. Particle velocities within the shock layer in front of the samples are then obtained through PIV. The experimental results are subsequently compared with particle-free CFD simulations to assess the measurements accuracy and to highlight key flow phenomena. Finally, collected particles at the stagnation point are analysed using SEM and EDX to determine their morphology and composition.

4.1 Particle Velocity in the Free-Stream

The average free-stream particle velocity is shown in the following figures. Figures 4.1a and 4.1b correspond to FCI^P with two different camera objectives, 50 mm and 100 mm, respectively. Similarly, results for FCII^P are presented in Figures 4.2a and 4.2b. The data are displayed with streamlines, no smoothing, and linear interpolation. For the definitions of FS1, FS2, and SL, see table 3.3 in the previous chapter.

To better appreciate the results, the *particle velocity* profiles along the transversal direction (y-axis) are reported in figure 4.3. Each line of the same set corresponds to a different position on the x-axis. In the figure, the PIV results are compared with the CFD *flow velocity* profile[1] at the location $x = 50$ mm. The TDLAS measurements presented in figure 3.4b are reported for CFD validation purposes, along with the associated errors which are lower than 5.4%.

One should note that the TDLAS analysis is performed at $x = 100$ mm, and it is compared with the expected CFD flow velocity profile on that location. This point is located 20 mm downstream of the rightmost part of the PIV evaluation's RoI. The expected velocity increment between the axial positions of $x = 50$ mm and $x = 100$ mm is less than 0.8%, from CFD. For this reason, the TDLAS analysis is considered a valuable additional information to the PIV results, that highlights the particle velocity lag. However, the TDLAS measurements were performed without particles; in the future, the possibility of performing the same measurements in particle-laden flows should be assessed.

The particle velocity measured with PIV is considerably lower than the flow velocity obtained from TDLAS, indicating a significant lag between the particles and the gas

[1]The CFD results are described later in detail, in section 4.3.

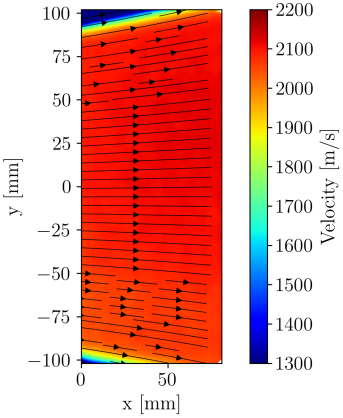

(a) Average particle velocity field, 50 mm objective (test FS1)

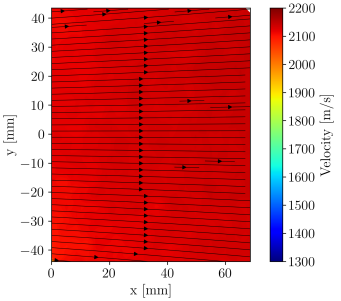

(b) Average particle velocity field, 100 mm objective (test FS2)

Figure 4.1: Free-stream PIV in FCI^P, (tests FS1, FS2)

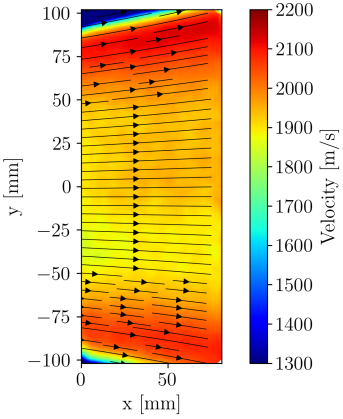

(a) Average particle velocity field, 50 mm objective (test FS1)

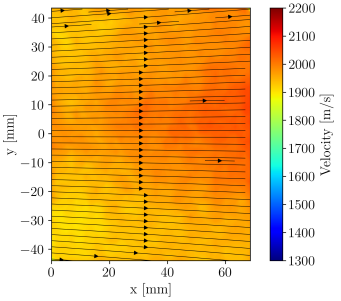

(b) Average particle velocity field, 100 mm objective (test FS2)

Figure 4.2: Free-stream PIV in FCII^P, (tests FS1, FS2)

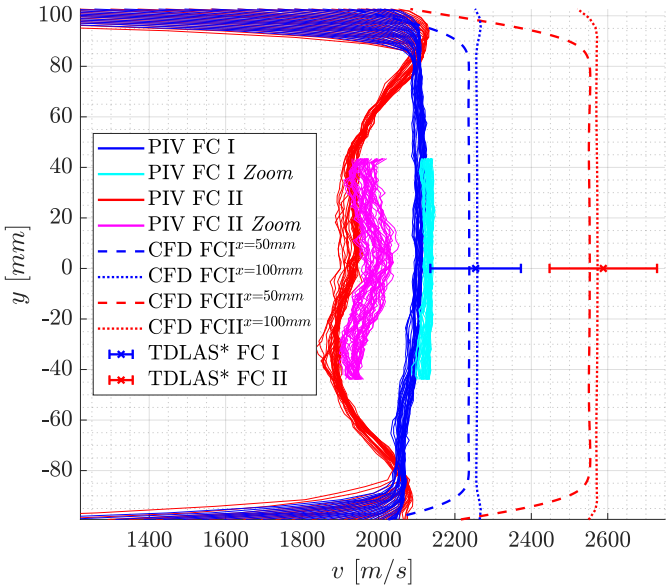

Figure 4.3: Mean particles' velocity profiles along transversal direction, compared with flow velocities from CFD results (DLR-TAU flow solver) and TDLAS. CFD transversal profiles are reported only for $x = 50$ mm and $x = 100$ mm for visualisation ease. *In the legend, " * " refers to the axial position $x = 100$ mm, where the TDLAS velocity measurements were performed*

flow. This lag is attributed to the low-density, accelerating nature of the L2K flow. Furthermore, the velocity difference between particles and gas is significantly larger in FCII^P than in FCI^P. Although the CFD-predicted flow velocities are higher for FCII^P due to its greater enthalpy level, particles in FCI^P are generally faster—except in the outer layers, for $|y| > 80$ mm. Another notable distinction between the two flow conditions lies in the qualitative distribution of particle velocity: while FCI^P exhibits a relatively homogeneous high-velocity core, FCII^P shows slower particles in the core compared to those in the outer regions.

One can observe that the velocity measured with higher zooming capabilities is slightly higher for both flow conditions. In both flow conditions, the bottom region of the flow presents averagely slower particles, suggesting that the gravitational effect could play a role in this regime: heavier and thus slower particles could be concentrated in the lower

Table 4.1: Relative uncertainty on the average velocity

FC	$\lvert y\rvert < 90$ mm	Outer Layers	Ext. IW*
FCI^P	$u_v < 0.4\%$	$u_v < 1\%$	$u_v < 10\%$
FCII^P	$u_v < 0.6\%$	$u_v < 2\%$	$u_v < 15\%$

*Ext. IW stands for extremal interrogation windows, namely the top- and bottom-left of the results

part. Both flow conditions present slower regions in correspondence with the boundary layer of the flow exiting the nozzle.

The standard deviation of the particle velocity, σ_v, is shown in figures 4.4a and 4.4b, for the two flow conditions. The uncertainty of the mean velocity is estimated by DaVis as $\sigma_v/\sqrt{N}$, where N denotes the number of valid vectors within the considered IW. The corresponding relative uncertainty is given by $u_v = \frac{\sigma_v/\sqrt{N}}{\mathbf{v}_p}$. For both flow conditions, high uncertainty is observed in the boundary-layer region ($|y| > 90$ mm), whereas the central region of the flow ($|y| < 90$ mm) exhibits lower uncertainty. The outermost IWs, located in the top-left and bottom-left portions of the evaluated region, show the highest uncertainty due to their combination of large standard deviation and a small number of valid vectors. A summary of the relative uncertainty values is provided in table 4.1.

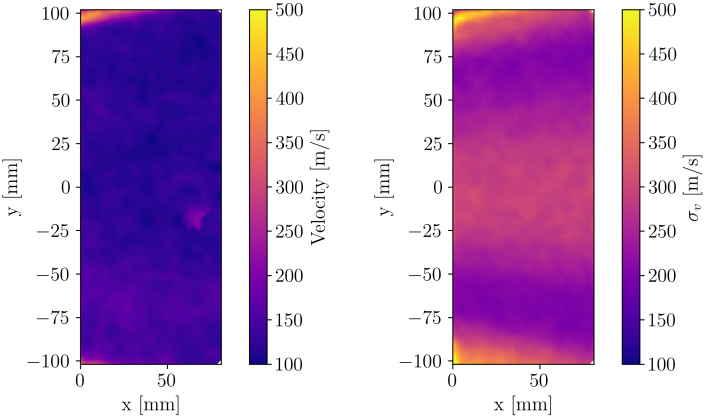

(a) FCI^P, 50 mm objective **(b)** FCII^P, 50 mm objective

Figure 4.4: Standard deviation σ_v, (test FS1)

In figure 4.5 the velocity profiles shown in figure 4.3 are reported, in comparison to the

average transversal profiles of standard deviation. For visualisation ease, the profiles have been condensed in a single transversal profile by averaging along the x-axis. A similar procedure was performed with standard deviation profiles. One can observe that

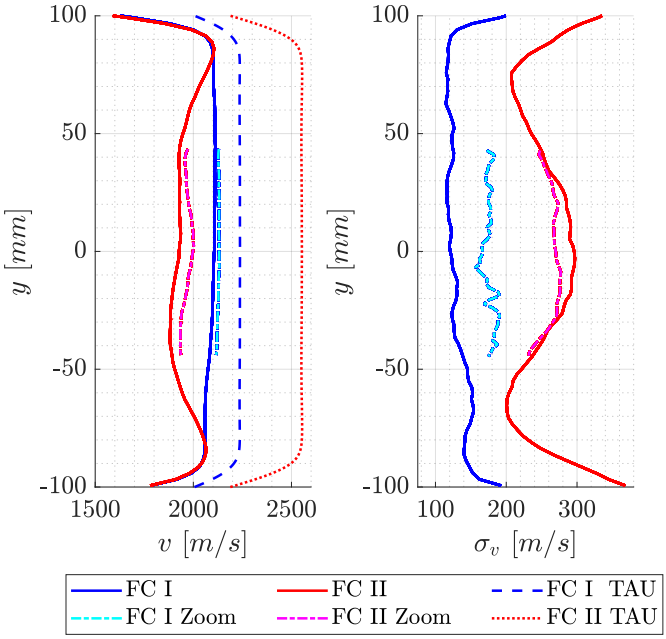

Figure 4.5: Mean velocity and standard deviation profiles along the transversal direction, averaged the along x-axis

the very outer flow regions present the highest standard deviation, in correspondence with the shear layer. Moreover, there are other zones with high statistical variations, which differ in location between the two flow conditions. In particular, FCII^P has high standard deviation in the core region, while in FCI^P the higher standard deviation zone lays right below the flow core. By comparing velocity and standard deviation in figure 4.5, it is observed that the regions with high standard deviation coincide with regions with averagely slower particles.

The reasons for the counter-intuitive results, the slight asymmetries in particles velocity flow field, the faster results of the zoomed tests, and the duality between low velocity and high standard deviation, could be due to the following possible reasons, whose relevance

is discussed in the next sections:

4.1.1) Agglomeration due to melting.

4.1.2) Difference in flow properties for different flow conditions.

4.1.3) Spatial resolution.

4.1.4) Gravity effect.

4.1.5) Change of flow features due to injection.

4.1.1 Agglomeration Due to Melting (Agglo-Melting)

The melting temperature of MgO ($T_m = 3125$ K, from [43]) is higher than the computed reservoir temperature of FCI^P and lower than the reservoir temperature of FCII^P, both reported in table 3.1. Thus, one possible reason for the difference in qualitative behaviour between flow conditions could be agglomeration due to melting, or agglo-melting; for this reason, the number of agglo-molten and heavier particles could be higher in FCII^P than in FCI^P, given the same controlled particle size distribution as input in the reservoir. Supports of the agglo-melting hypothesis are multiple; some are discussed in the next sections. Here, a summary of them is reported:

- The duality between the evaluated velocity and standard deviation (i. e. the correspondence between zones of low velocity with high standard deviation) is the first evidence. Regions with high standard deviation tell that the particle velocity value presents a high spread over testing time. The broad particle velocity range could be due to a broad range of particle sizes and shape, that get differently accelerated by the flow, due to their different drag and inertia[2]. Thus, the higher standard deviation is caused by the broad range of particle sizes, i. e. the presence of agglomerates that is caused by agglomeration processes. Since this phenomenon is not present in FCI^P, it is reasonable to assume that agglomeration is favoured by melting—which does not happen in FCI^P due to the lower reservoir temperature. Both the FS- and SL-PIV results present higher fluctuations and uncertainty in the case of FCII^P (figures 4.4b and 4.11b). Agglo-melting causes in fact a variation of the particle size distribution, which leads to a broad velocity range of different-sized particles. This results in larger fluctuations in the PIV results.

- Collected particles present signs of melting in FCII^P only, as discussed in section 4.4.

[2]For instance, one could hypothesise that bigger particles are less accelerated during the expansion along the nozzle axis due to their higher mass.

- While the cork samples at all FCs^{nP} look similar even at different enthalpy levels, the eroded cork samples presents more cells in FCII^{P} (section 5.1: figure 5.2d) than in FCI^{P} (section 5.1: figure 5.2b). This indicates that the amount of particles in FCII^{P} is reduced (as confirmed in chapter 6), eventually due to agglo-melting. In addition, the large agglo-molten particles might reside in the core part of the flow; therefore, more erosion is visible in the central area of the sample surface in FCII^{P}.
- The particle count is considerably lower in FCII^{P}, compared to FCI^{P}, as reported in chapter 6.

Agglo-melting may have a negative effect on the PIV results. In figure 4.6, one exemplary correlation map is reported for both flow conditions, at the same position on flow axis. One can observe that the PIV results' averaged correlation maps differ between FCs^{P}: FCII^{P} presents overall more stretched correlation peaks, with respect to FCI^{P}, highlighting the broader distribution of particle velocity in the higher enthalpy flow condition. This arises because the PIV technique uses the cross-correlation algorithm and it assumes a uniform velocity within each interrogation window. When particles with varying velocities are present in the same window, this assumption is violated, potentially leading to bad-quality correlation peak or unreliable vectors. The stretching seen in the averaged correlation maps thus reflects the broader dispersion of particle velocities under the higher-enthalpy condition. In addition, one should consider that elastic collisions between particles moving with different velocities can happen if the seeding density is large enough, which causes a change in the velocity direction. In addition, it should be

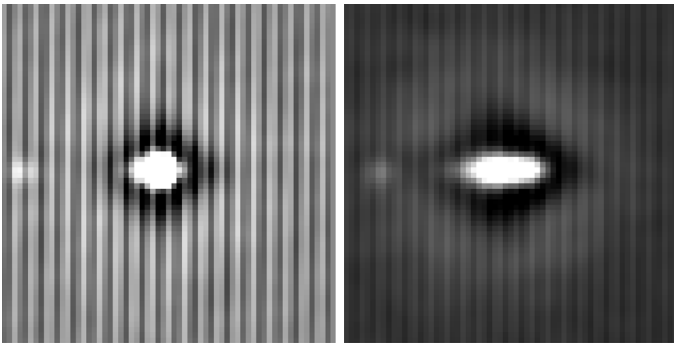

Figure 4.6: Averaged correlation maps of FCI^{P} (left) and FCII^{P} (right), at the position (x,y) = (0,40) mm

noted that larger particles[3] scatter more light, appear brighter in images, and tend to

[3]The particle's image size cannot be directly related to the particle's physical size due to the phenomenon

dominate the PIV measurements, which biases the results toward the velocities of heavier and slower particles. This explains why the FCII^P results are slower than expected in the flow core. Signal normalisation during pre-processing is crucial to mitigate this effect.

A qualitative result similar to FCII^P in terms of velocity measurements was observed in the ESA-EMAP project [100], where PIV was used to characterise alumina particles speeds at the exit of a solid rocket motor: the outer layers of the flow carry the faster (i. e. smaller) particles, while the flow core carries the slower (i. e. bigger) particles. Bigger particles, in fact, cannot follow the flow on its outer layers, in the low-density expansion regime, as visible in figure 4.7. In addition, the overall PIV results compute lower velocities than other techniques (e.g. L2F), as the PIV evaluation is dominated by bigger particles, that have higher velocity lag.

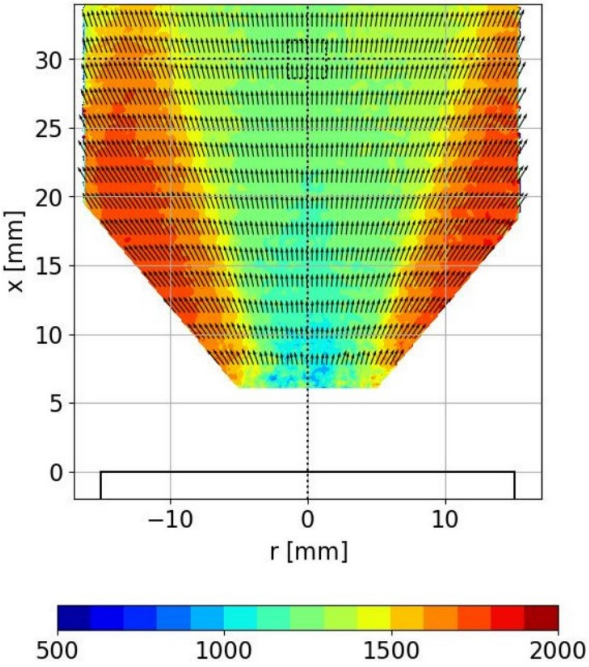

Figure 4.7: Mean velocity of test *"Ex1-P1"*, from EMAP [100]. The nozzle flow is from bottom to top

of diffraction-limited imaging, reported in [95].

Agglo-melting effects could be further verified in the future by repeating the experiments with different particles with lower melting temperatures than the reservoir temperature of FCI^P, and observing if the qualitative result of FCI^P gets more similar to the one of FCII^P. In addition, different tests with same particles and different reservoir temperatures (intermediate values between FCI^P and FCII^P) could be performed to better investigate how the average velocity profiles evolve when the reservoir temperature is changed. Moreover, particles with different chemical species could be tested to better represent Martian dust, which is mainly composed of silicon-, aluminium-, iron-, magnesium- and calcium- oxides [75]. However, the possibility of using such a mixture in the L2K still needs to be assessed, due to the much lower average melting temperature of the mentioned chemical compounds that might cause nozzle clogging and particle deposition effects inside the nozzle.

4.1.2 Difference in Flow Properties for Different Flow Conditions

Another factor contributing to the observed differences between the two flow conditions is the variation in chemical composition, evaluated with CFD simulations (section 4.3). In high-temperature flows, chemical reactions typically reduce the effective specific heat ratio γ via endothermic processes such as CO_2 dissociation. In the present cases (FCI^{nP} and FCII^{nP}), however, vibrational excitation dominates, resulting in a slightly higher γ in the higher-enthalpy condition (FCII^{nP}) compared to the lower-enthalpy case (FCI^{nP}), both in the reservoir and in the free-stream. Higher reservoir enthalpy also leads to a higher free-stream velocity $\mathbf{v}_g$, while producing lower density ρ, pressure p, and temperature T. Free-stream properties of both FCs, calculated using the quasi-1D flow solver NATA at $x = 100$ mm, are presented in table 4.2. These flow differences directly affect particle

Table 4.2: Free-stream values computed with quasi-1D flow solver NATA [8]

Flow Condition	γ	$\mathbf{v}_g$ [m/s]	ρ [kg/m^3]	p [Pa]	T [K]
FCI^{nP}	1.24	2258	4.41e-4	83	831
FCII^{nP}	1.32	2567	4.02e-4	76	705

transport through the balance of drag force and particle inertia. The drag force, which scales with the flow density ρ_g and the square of the relative velocity $\mathbf{v}_{slip}$, acts to accelerate particles along the flow, while particle inertia resists motion. In FCII^P, the higher velocity increases particle–flow interactions, but the lower density reduces the drag force, potentially leading to less uniform particle distribution. In FCI^P, the higher density increases drag relative to inertia, promoting more uniform transport along the flow, as observed in figure 4.1a for FCI^P and figure 4.2a for FCII^P. Particle morphology further complicates this balance: agglomeration and partial melting alter particle size and shape, affecting both the effective cross-sectional area, drag coefficient, and inertia, but

these changes are not captured in the current setup. Consequently, the relative transport capability of FCI^P versus FCII^P remains uncertain, and future studies should focus on quantifying how morphology and flow conditions jointly determine particle transport. Furthermore, the CFD simulations do not resolve the particles, and for this reason this whole discussion is valid in the hypothesis of one-way coupling between flow and particles, which means that the flow has an effect on particle motion, but the particles have no effect on flow properties.

4.1.3 Spatial Resolution

The higher magnification of the objective used in test FS2 provides increased spatial resolution, allowing smaller particles to be visualised. These are faster in such conditions, causing the measured velocity to be higher with higher zoom, as confirmed by experimental results. This phenomenon highlights a limitation of the PIV technique: results can vary slightly depending on the objective used. Because these smaller particles tend to move faster, the measured velocities can appear higher with higher magnification, while lower-magnification objectives capture a larger field of view but may miss the fastest, smallest particles. The L2F technique can overcome this limitation, as it employs a method based on focused lasers; however, it does not provide 2D-resolved measurements. Since the difference between PIV results with different objectives is negligible, all PIV results are considered valid.

4.1.4 Gravity Effect

The slower particle velocity observed in the lower region of the flow (in both FCs) may be related to gravitational effects; specifically, larger and heavier particles could preferentially accumulate in the lower region of the flow due to their greater susceptibility to gravity. However, given the high flow velocities in the facility, the relative importance of gravitational forces compared to aerodynamic drag is expected to be limited. Therefore, this interpretation remains a hypothesis rather than a confirmed mechanism. This effect would be expected to become more pronounced under lower flow velocity conditions, where the influence of drag is reduced relative to gravity. However, for the reasons reported in section 4.1.2, FCI^P and FCII^P cannot be directly compared in these terms due to differences in reservoir gas dissociation and flow density. Verification of this hypothesis would require future studies under controlled conditions, varying flow velocity while maintaining comparable flow density, to assess whether asymmetries between the lower and upper regions become more pronounced at lower velocities.

4.1.5 Change of Flow Features due to Injection

The hypothesis of relating flow asymmetries to the particles injection process was proved to be wrong, as it was verified that the injection of the bypass flow does not change flow properties significantly: stagnation pressure and heat flux measurements were conducted, for all particle-free flow conditions, both with and without bypassing 2 g/s from the main CO_2 flow, and keeping the overall mass flow rate of CO_2 at 40 g/s, as reported in table 3.1 (the bypass process is described in section 3.1), at a position of $x = 100$ mm. The stagnation pressure measurement was performed with a Pitot probe translating on the flow's horizontal mid-plane, on the transversal direction. The test result is reported in figure 4.8a[4]. The heat flux measurement was carried out on flow axis with a coaxial thermocouple installed in a 25 mm diameter cylinder oriented with its axis parallel to nozzle axis, and the result is reported in figure 4.8b.

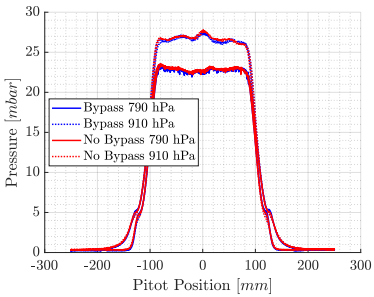

(a) Pitot measurements of FCI^P (continuous line) and FCII^P (dashed line)

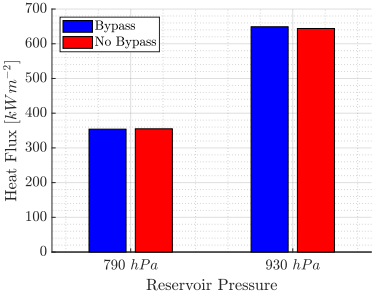

(b) Heat flux measurements

Figure 4.8: Stagnation point measurements at $x = 100$ mm

The injection of the unseeded bypass flow does not change flow thermodynamic characteristics, and it does not cause any instability or asymmetry in the flow properties. The Pitot measurements with a seeded bypass flow would be impossible, as particles would clog the probe. Non-intrusive heat flux measurements in the seeded flow are not trivial, and a dedicated study should be performed in the future to perform such experiments. In fact, particles might accumulate on the probe surface, developing a thin layer that may alter the surface emissivity, thus interfering with the measurement.

[4]The higher enthalpy condition was run with a reservoir pressure of 910 hPa because of minor problems with the arc-heater electrodes during the test. The test is still considered valid as a proof of non-intrusivity of the bypass flow.

4.2 Particle Velocity Across the Shock Layer

The average particle velocity obtained in the SL setup is presented in figures 4.9a and 4.9b, for FCI^P and FCII^P respectively. The results are presented with no smoothing, and streamlines are plotted to highlight the particle velocity field in the shock layer. The large white mask on the right is the sample profile, while the small triangular mask on the bottom left is a region that was not sufficiently illuminated by the PIV laser. One can observe different particle velocity-field features, which are—from left to right—the free-stream, the steep velocity gradient, and the shock layer, that includes a counter-flow region.

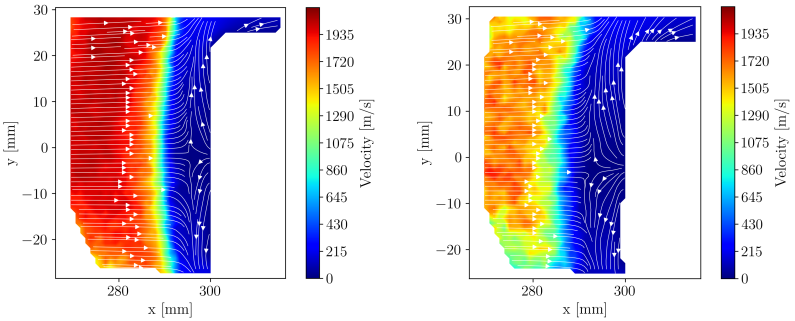

(a) FCI^P **(b)** FCII^P

Figure 4.9: SL-PIV result. The white region on the right is the cork sample. The flow comes from the left

FCI^P has generally smoother results than FCII^P. The reason lays in the seeding density, and in the agglo-melting phenomenon described before: due to agglomeration favoured by melting, less particles are present in FCII^P—the seeding density is lower. Moreover, agglomeration leads to a size distribution change of the seeded particles, causing a velocity dispersion: bigger particles are less accelerated by the flow, than smaller ones—this causes the higher enthalpy flow condition FCII^P to have a lower average particle velocity. For this reason, the PIV algorithm evaluates more fluctuating results when the particle size is not homogeneous. In both results, one can observe that the average particle velocity value in the free-stream is about 2050 m/s in FCI^P, and 1800 m/s in FCII^P. These velocities are slightly lower than the FS-PIV results. The observed mismatch may arise from slight differences in particle properties and flow parameters. The total enthalpy and temperature of the flow depend on the wind tunnel's mass flow rate and reservoir pressure. Specifically, for a given input power in the arc heater, increasing the reservoir pressure

results in higher enthalpy and temperature, whereas increasing the mass flow rate reduces both. Consequently, the reservoir conditions influence the agglo-melting phenomenon, promoting particle agglomeration when the reservoir temperature is slightly elevated. This, in turn, significantly affects the average particle velocity, potentially causing minor variations between runs, which are considered negligible. Moreover, rebounding particles present in the free-stream region of the SL-PIV measurements influence the averaged particle velocity, leading to a reduction of the mean velocity.

The shock layer's average particle velocity field is computed in both the stagnation region and in the shoulder region, where the flow expands to follow the probe's contour. It is interesting to see that, for both flow conditions, a region with counter-flow is present right on the probe surface. The counter-flow is believed to be due to different effects, namely the particles bouncing back after hitting the surface, the particles released due to probe's erosion, and the ones from probe's outgassing. For this reason, the stagnation point of the particle-flow lays few millimetres upstream of the probe's surface. The detached position of the stagnation point might misleadingly suggest that particles do not impact the surface. However, it is important to note that the results shown represent an average, and the apparent detachment of the stagnation point could be caused by rebounded particles—that is, particles that have already collided with the probe and bounced off. In other words, particle trajectories do not coincide with the plotted streamlines.

In FCI^P, the velocity gradient caused by the shock is well resolved. This region that has the highest velocity gradient is not to be interpreted as a fluid-dynamic shock, since the particles exhibit a velocity lag relative to the flow. Thus, the actual fluid-dynamic shock location may differ. In FCII^P, this region presents less smooth values, but the velocity decrease is nevertheless observed. To better visualise the steep gradient, the particle velocity profiles along the axial coordinate x are reported for both flow conditions in figures 4.10a and 4.10b, for FCI^P and FCII^P respectively.

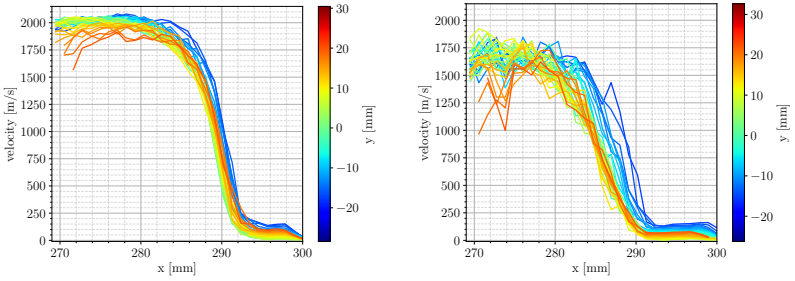

(a) FCI^P **(b)** FCII^P

Figure 4.10: Velocity profiles

It is worth to see the data from another perspective, namely the fluctuations of the results, which are evaluated through the relative uncertainty $u_v = \frac{\sigma_v/\sqrt{N}}{\mathbf{v}_p}$, where σ_v is the standard deviation of the velocity after averaging the dataset, N is the number of valid samples, and $\mathbf{v}_p$ is the particle velocity magnitude. The fluctuations are presented in figures 4.11a and 4.11b, for FCI^P and FCII^P respectively, in terms of percentage.

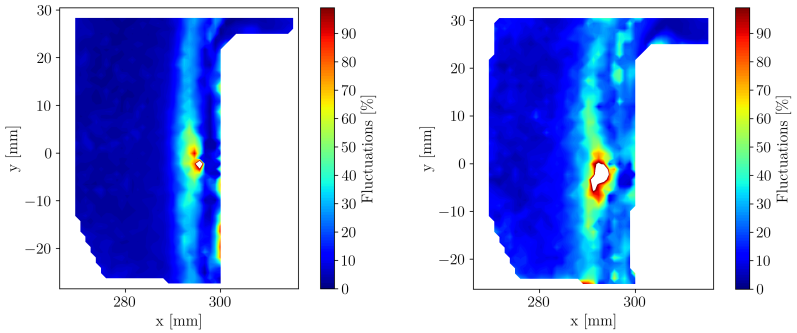

(a) FCI^P **(b)** FCII^P

Figure 4.11: Relative fluctuations

For both flow conditions, the free-stream and the part of the shock layer close to the sample present low fluctuations, which are prevalently below 10% for FCI^P and 20% for FCII^P. The region that bounds the flow and the counter-flow presents fluctuations between 20% and 40%, and the region surrounding the stagnation point can be well above 70%. Around the stagnation point, which lays few millimetres upstream of the probe's surface, the fluctuations can be higher than 100%. In this region, the computed velocity is below 15 m/s, and the particles may exhibit reverse velocity components due to outgassing, erosion, and rebounding, leading to significant fluctuations in the results.

PIV is effective only in flows where particles within each interrogation window move coherently in the same direction. Near the stagnation point, this condition is often violated due to the coexistence of free-stream particles with those that have rebounded, been eroded, or expelled by outgassing. In such regions, the fundamental PIV assumption is not satisfied, and the resulting velocity measurements can be invalid. For future studies, PTV could be employed to follow individual particles, circumventing the limitations of PIV in regions with strongly heterogeneous particle motion.

4.3 CFD Results

The CFD results obtained for both FCs^{nP} with the setup described in section 3.4 are reported in figures 4.12 and 4.13, for the undisturbed flow in the wind tunnel and the flow field around samples respectively. The Knudsen[5] number evaluated with TAU in the whole flow core is lower than 10^{-3}, as well as in the shock layer upstream of the sample, confirming that the continuum assumption is valid in these regions. Within the actual bow shock, the Knudsen number can reach values up to 0.65, thus the internal resolution of the shock is questionable. However, the relevant parameters for this analysis are the free-stream velocity, the shock-layer velocity and the shock stand-off distance δ. Thus, the uncertainty in the resolution of the shock is accepted.

One can observe that the higher enthalpy flow condition is associated to higher flow velocity, Mach number, and CO_2 dissociation, that can be quantified by the amount of carbon monoxide in the flow. The atomic oxygen mass fraction is negligible in FCI^{nP}, and it is approximately 0.07 in the free-stream of FCII^{nP}. The higher dissociation causes different flow chemistry between the flow conditions, which leads to peculiar characteristics, such as lower static pressure (not reported in the pictures) and static temperature in the higher enthalpy flow condition.

Similar flow fields are observed in terms of velocity, temperature, and Mach number distributions in the SL region. A detached bow shock slows the gas to subsonic velocities right in front of the sample surface The flow rapidly expands and accelerates to supersonic velocities around the sample's shoulders The stagnation point lays on the sample surface, as observable with the plotted streamlines. In the shock layer in front of the probe, temperature rises up to stagnation values. The carbon monoxide and atomic oxygen mass fractions do not change significantly between free-stream and shock layer, highlighting that the free-stream might be chemically frozen, and that chemical non-equilibrium needs to be taken into account; recombinations happen in the vicinity of the surface. A non-physical increase of carbon monoxide concentration is visible on the shock line, in correspondence with the high Knudsen number region. However, due to the mentioned reasons, this simulation is considered acceptable.

In figures 4.14a and 4.14b, the simulations are zoomed in the relevant RoIs for direct comparison with particle-velocity data. The comparison is valid under the assumption of one-way coupling between flow and particles.

One can observe that:

- The computed wind tunnel free-stream exhibits a high degree of homogeneity at the sample location, both in velocity magnitude and direction: the sample lies entirely within the homogeneous flow core.

[5]This section refers to the gas Knudsen number, not to be confused with the particle Knudsen number defined in section 2.1.2.

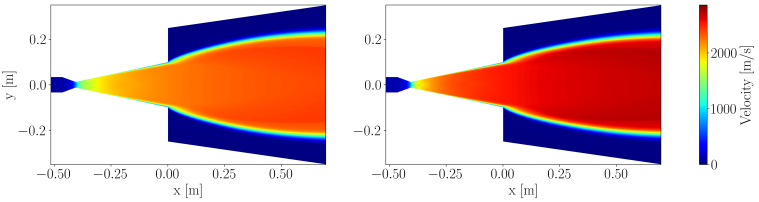

(a) Velocity of FCI^{nP} (left) and FCII^{nP} (right)

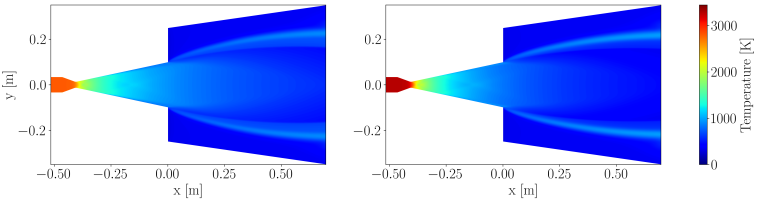

(b) Temperature of FCI^{nP} (left) and FCII^{nP} (right)

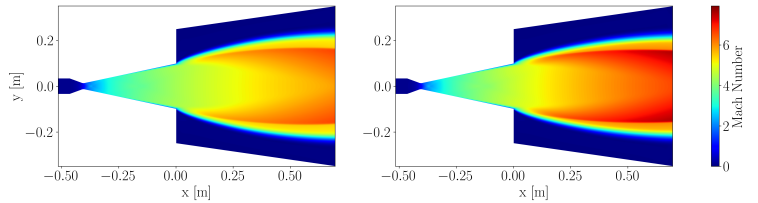

(c) Mach number of FCI^{nP} (left) and FCII^{nP} (right)

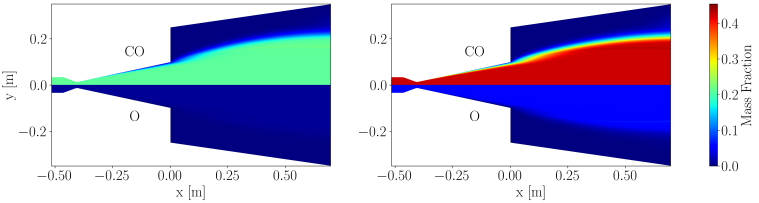

(d) CO and O mass fraction of FCI^{nP} (left) and FCII^{nP} (right)

Figure 4.12: Free-stream CFD results

- The free-stream particle velocity obtained with FS-PIV is significantly lower than the computed flow velocity, suggesting that a considerable velocity lag—on the

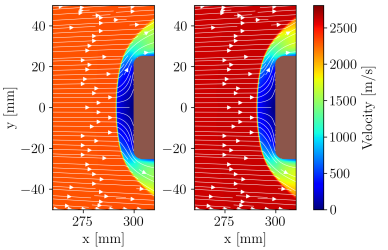

(a) Velocity and streamlines of FCI^{nP} (left) and FCII^{nP} (right)

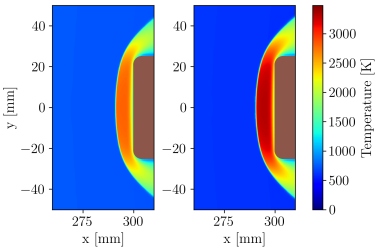

(b) Temperature of FCI^{nP} (left) and FCII^{nP} (right)

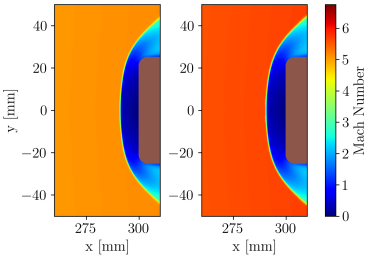

(c) Mach number of FCI^{nP} (left) and FCII^{nP} (right)

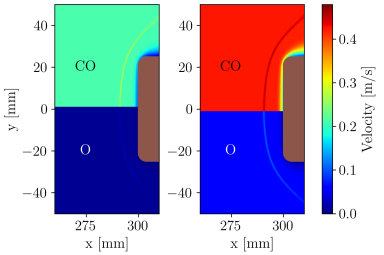

(d) CO mass fraction of FCI^{nP} (left) and FCII^{nP} (right)

Figure 4.13: Shock-layer CFD results

order of several hundred metres per second—exists between particles and flow. The same consideration is valid regarding the free-stream region of SL-PIV data.

- A comparison between CFD results (figure 4.14b) and SL-PIV measurements (figures 4.9a and 4.9b) reveals that, in the shoulder region, CFD predicts velocities up to 1500 m/s, whereas PIV measurements do not exceed 500 m/s. This suggests that the particles are either unable to keep up with the rapidly expanding flow in that region, or that outgassing has generated a thick, slower-moving layer in which the particles are entrained.

- The counter-flow seen in experimental data is not captured in the CFD simulations, as the setup does not account for outgassing or particle rebound phenomena. As a result, the stagnation point predicted by CFD differs from that observed in the PIV measurements: in the CFD, it lies on the probe surface, whereas in the PIV data, it is detached from the surface. This discrepancy suggests that the counter-flow

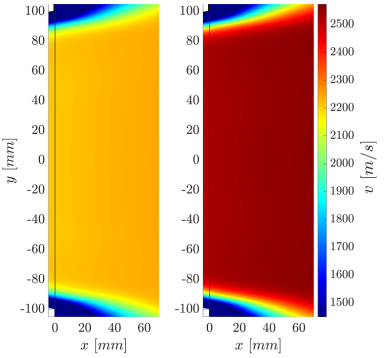

(a) Free-stream of FCI^{nP} (left) and FCII^{nP} (right). The vertical grey line represents the nozzle's exit section

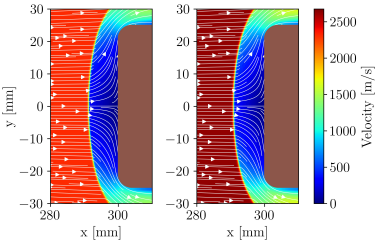

(b) Stagnation point of FCI^{nP} (left) and FCII^{nP} (right)

Figure 4.14: Numerical simulations with DLR-TAU flow solver. Note that the two sub-figures have differently scaled colour-bars

observed in the PIV results is caused by the material response or by the presence of particles.

- The CFD results show that the shock in the gas phase is located much closer to the surface than the particle "shock", which is somewhat counter-intuitive. In principle, one would expect particles to start decelerating downstream of the fluid-dynamic shock due to their velocity lag relative to the gas. However, it must be noted that the CFD simulations do not account for material response effects, such as surface outgassing. As a result, the actual fluid-dynamic shock in the experiment could be pushed back upstream by outgassing, which would position the particle "shock" downstream of it—consistent with the expected physical behaviour.

More advanced numerical simulations should aim to clarify the causes behind the discrepancy in shock stand-off distance δ observed between CFD and PIV results. Current CFD analyses typically neglect particle feedback on the gas phase (i. e. they assume one-way coupling), they do not fully capture multi-way interactions or high-enthalpy effects present in the experiments, and do not account for the material response. In PIV measurements, the observed larger and more fluctuating δ could be attributed to counter-flows generated by surface outgassing or particle rebounding, which locally modify the flow composition and energy balance, as well as to variations in the particle count. The isentropic parameter γ is strongly linked to δ, as it influences the compressibility of the gas and the resulting shock position. In turn, γ is affected by several factors—such as gas-

phase chemistry, recombination processes, and the mixing of outgassed material with the main flow—as well as by particle catalycity, which can alter the effective thermochemical state of the gas. These coupled effects may lead to local variations in γ and consequently in the shock stand-off distance. The sketches reported in figure 4.15 summarise the mentioned effects (note that the mixing effect may have an effect on γ as well). Future studies should investigate whether accounting for two-way coupling between particles and the flow is necessary to reproduce the experimentally observed δ and its fluctuations, or if the influence of such effects remains negligible. Future simulations should require the development of a setup capable of resolving particle trajectories and their rebound, and outgassing phenomena, if necessary. Particle trajectories should be accurately simulated and tracked to capture their dynamic interaction with the flow.

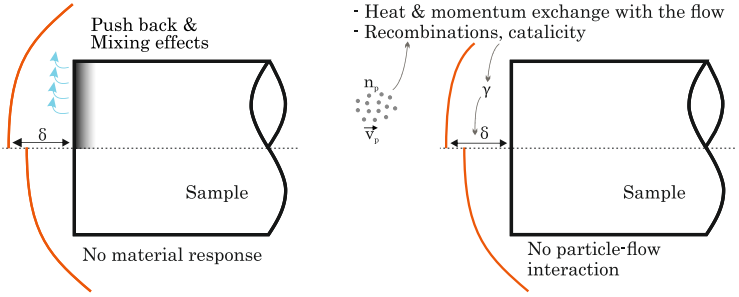

(a) Material response influence (above) **(b)** Particle influence (above)

Figure 4.15: Effects of particles and material response on shock stand-off distance δ

Furthermore, future research should aim to apply PIV around water-cooled steel (or copper) samples with the same geometry as the cork samples used in this study. This configuration eliminates the outgassing phenomenon, allowing for a direct comparison with the current results to determine whether outgassing or particle rebound plays the dominant role in the observed counter-flow behaviour. The outcome of this comparison will provide valuable insights for developing efficient and physically meaningful numerical setups.

4.4 Particle Collection

The particles collected in FCI^P are reported in figure 4.16. They form a thick layer of solid material on top of the copper tape. This is due to sintering caused by the energy released on impact combined with the high temperature in the stagnation point. It is in

fact hard to recognise particles in the reported picture, as their morphology changed on impact. However, a grainy structure of the sintered layer is visible, which supports the hypothesis that the particles did not experience a phase change during flight.

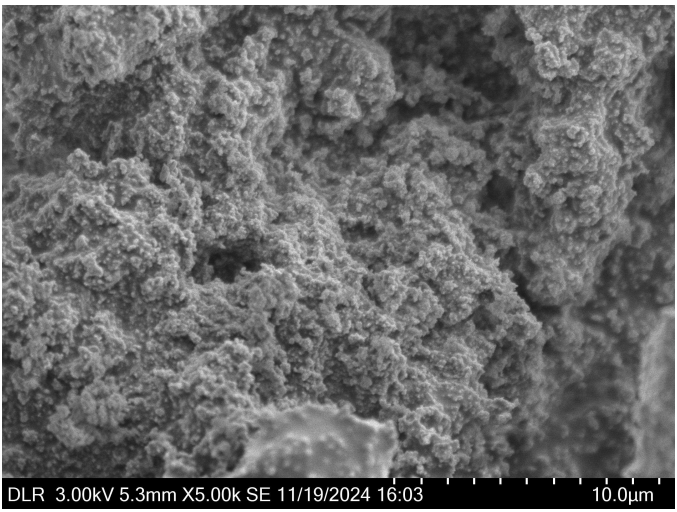

Figure 4.16: SEM image of collected particles in FCI^P

The particles collected in FCII^P, reported in figure 4.17, are instead subject to different phenomena. The picture shows different particles/chunks laying on a rough surface. The rough surface **A** is copper oxide, which is probably created after the reaction of carbon monoxide or atomic oxygen in the flow with the copper tape, whose glue layer evaporates in a fraction of a second. The big chunky structure in the middle of the image **B**, as well as the small spheres on the top left **C**, the darker small spots splashed on the copper oxide layer **D**, and the smoother regions on the bottom left and top right **E**, are made of MgO, namely the same species of the particles used during the tests. By comparing the picture with the control sample shown in section 3.3.4, one can observe that the morphology of particles has completely changed during the test, and it looks like they have melted, most likely in the reservoir, where the flow temperature is higher than the melting temperature of MgO. Probably, the big chunk **B** was either fully solid or half molten before collision, the spherical agglomerate **C** was solid before collision, while the darker spots **D** were small molten spheres that splashed on impact, and the smoother regions **E** might have been large agglo-molten particles. These results bring further evidence of the agglo-melting hypothesis presented in the previous sections, as the phase

change is observed in FCII^P only.

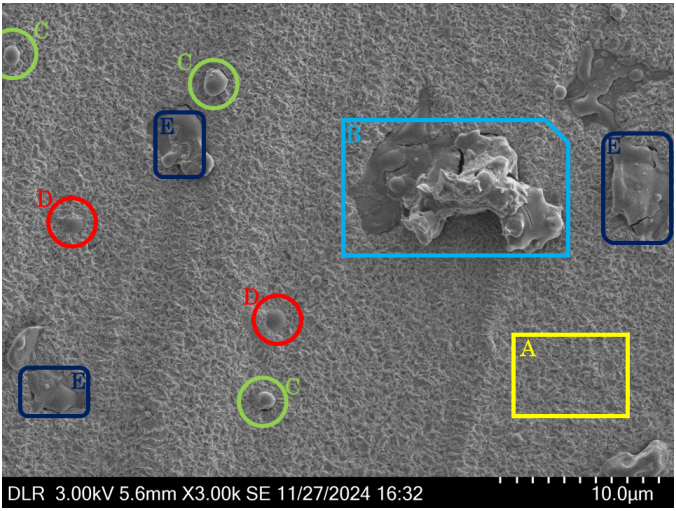

Figure 4.17: SEM image of collected particles in FCII^P

After studying several SEM pictures, it is hypothesised that the particles agglo-melt in the reservoir. Then, they cool down during the nozzle expansion and the free flight in the test chamber, probably experiencing another phase change as the free-stream cools to approximately 600 K. It is impossible to say, though, if the particles re-solidify during this colder phase, as the process highly depends on the particle size and its characteristic flight time. It is difficult to estimate these values, since the particle size distribution varies due to the agglo-melting process in the reservoir that causes also a velocity dispersion of the different-sized particles. The flight time from the nozzle throat to the sample's surface (a 700 mm long flight path) is in the order of hundreds of microseconds, if an average particle velocity between 1000 m/s and 2000 m/s is considered. Further investigation could be performed on the particles' thermal properties, to analyse the phase-change's characteristic times, and to characterise the particles' behaviour in the wind tunnel. Finally, the particles enter the hot shock layer, heating up again before colliding with the sample.

Agglo-melting can occur both within the wind tunnel's reservoir and in the region ahead of the probe (inside the shock layer), where the flow temperature exceeds the particle melting point. Although the shock layer is a very thin region, particles with a very low

Stokes number—namely, the smaller ones that closely follow the flow streamlines—may decelerate to subsonic velocities and remain within this region for a relatively long time. Their small size also implies low thermal inertia, allowing them to rapidly heat up and potentially reach their melting point. The characteristic length and residence time of the particles in these high-temperature zones have an influence on the extent of the phenomenon. Future research should focus on determining whether these two parameters are comparable between wind tunnel conditions and the flight environment, to evaluate whether the agglo-melting phenomenon plays a role during the actual flight. For example, particle trajectory simulations should be conducted for both the wind tunnel and the flight environments. The results could be used to assess the residence time of particles in high-temperature regions and to compare the behaviour between the two conditions.

Note that this analysis is to be intended as a qualitative analysis only, due to the intrusive nature of the collection technique. Nevertheless, it is considered as a valuable first insight into the highly challenging topic of particle collection in high-enthalpy flows. Future studies could focus on the development of a probe that can collect particles without altering their properties.

4.5 Summary and Future Steps

This chapter focused on characterising the used flow conditions by applying several diagnostic techniques, and by using CFD as a complementary tool. Flow and particle velocities were measured with TDLAS and PIV, respectively. PIV was used as a tool to measure the particle velocity field in two regions of interest—downstream of the nozzle exit and upstream of cork samples. Particles were collected and analysed with SEM microscopy and EDX. For the analysed flow conditions, the bypass flow used to inject particles in the main flow did not cause any change in flow properties. Higher particle velocity is measured with higher zooms, due to the higher resolution and capability of observing smaller and faster particles.

The study highlights that a significant velocity lag exists between flow and particles: PIV shall be used for particle velocity measurements only, and not for flow-diagnostic purposes. The particle velocity in the free-stream and in the shock layer ranges from 2100 m/s to a few m/s. Several particle-flow features are observed, such as the particle's steep velocity gradient across the shock, the shock layer, and a counterflow that might be due to outgassing and rebounded particles. The PIV results are compared with numerical simulations of the particle-free flow only in terms of shock stand-off distance and overall velocity, assuming one-way coupling between flow and particles: the simulated shock location is significantly different from the particle "shock"(steep particle velocity gradient) location.

Collected particles gave further insight in the L2K particle-laden flow characterisation: a considerable morphological change of the particles was attributed to the agglo-melting effect, in FCII^P, that stands for "agglomeration favoured by melting". The particles do not undergo the same phenomenon in FCI^P, as expected, since the total temperature of this flow condition is lower. Agglo-melting effects are also seen in the particle velocity field in terms of fluctuations of the velocity value.

- The most challenging aspect of this testing environment is represented by seeding a controlled amount of particles, with constant rate, being able to measure their velocities and their sizes. The high temperatures of the flow, combined with the relatively low mass flow rates, makes particle seeding very difficult to control. Further improvements on the seeding generator should aim at the realisation of a dedicated device optimised for the flow conditions' mass flow rates, able to control the particles flow rates to be given as input in the wind tunnel's reservoir.
- Future work is required for the improvement of numerical simulations, to address the reason of the stand-off distance discrepancy, and to define whether the one-way coupling assumption is valid. Particle tracking algorithms should be used to better resolve particle velocity in the highly complex region in front of the bow shock, where particles with reverse velocity components coexist. Using particle tracking techniques such as PTV could also lead to a better understanding of the particles' motion and sizes: by getting more than two frames, one could get information about the particles' trajectories and differentiate slower particles from faster particles. Another way of picturing a particle streak would be using a laser with a longer pulse time and a camera with a comparable acquisition time. An additional experimental technique to measure particles velocity (such as L2F) could be compared to PIV results. In fact, L2F results do not suffer from particle size distribution inhomogeneity, contrarily from PIV.
- The feasibility of TDLAS in particle-laden flows should be assessed, considering that this is a line-of-sight technique, that could suffer from SNR reduction due to the particles. TDLAS with a translating laser line could be implemented to measure the radial flow velocity profile, by applying the Abel transform. This result, combined with particles size measurements, could be valuable to validate drag models implemented in particle-laden flow solvers.
- To further characterise particle-laden flows in the L2K wind tunnel, particle size distribution should be measured in the future, and further experimental techniques should be developed or implemented in the L2K for this purpose. Particle collection with a simple stagnation sample, indeed, cannot be used for measuring particle size. The development of new techniques such as PDPA should be investigated. Engineering effort should be put in the construction of a probe for particle collection in such environment in order to characterise particle size and morphology.

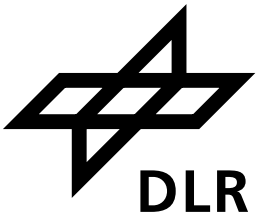
DLR

5 Sample Behaviour

Once the flow conditions were sufficiently characterised, the L2K facility was employed for material response testing. P50 cork composite probes, described in section 3.2, were exposed to dusty entry conditions, and their thermal behaviour was investigated using a comprehensive suite of diagnostics, including IR thermography, embedded thermocouples, 3D surface scans, and in-situ recession monitoring by LPT. The experiments revealed that particle loading strongly affects the thermal response of the cork material, leading to enhanced erosion rates and altered swelling behaviour. Furthermore, these tests demonstrated the feasibility of conducting long-duration, dusty, high-enthalpy experiments in the L2K facility, establishing a robust basis for future TPS investigations under Mars-relevant entry conditions.

5.1 Qualitative Analysis

Snapshots from video monitoring are shown in figure 5.1 to qualitatively show the sample behaviour during the test in the different flow conditions. The photos on the left are relative to FCs^{nP}, namely the tests without particles, while the ones on the right are relative to FCs^{P}, namely the tests with particles. One can observe the particles' erosive effect that causes the disruption of cork charring cells, and the effect of the higher enthalpy of $\text{FCII}^{P/nP}$ that makes the sample surface hotter, thus brighter.

The photographs of the samples taken after each test are presented in figure 5.2, with the same order as presented above. One can observe that, in FCs^{nP}, the sample surface develops a granular structure characterised by specific patterns, called charring cells. These tend to grow in size during the test, up to a point where their size stabilises. This is a well-known behaviour of cork-based ablators, already observed in several experimental campaigns, such as in [101]. On the other hand, when particles are present in the flow, the cells are completely absent for FCI^{P}, and present on a smaller extent in FCII^{P}. In fact, the cells are much smaller in FCII^{P} than FCII^{nP}, and they are found only on the sample surface's outer region. In the tests with particles, the surface looks rougher, and spikes are observable: particle impacts induce erosion, namely the rupture of the cells, detaching the sample surface layer and exposing the underlying virgin one. The impact location is stochastic, depending on the particle seeding density in the flow. For this reason, it is hard to recognise patterns on the eroded surface, contrarily to the case where particles are not seeded in the flow.

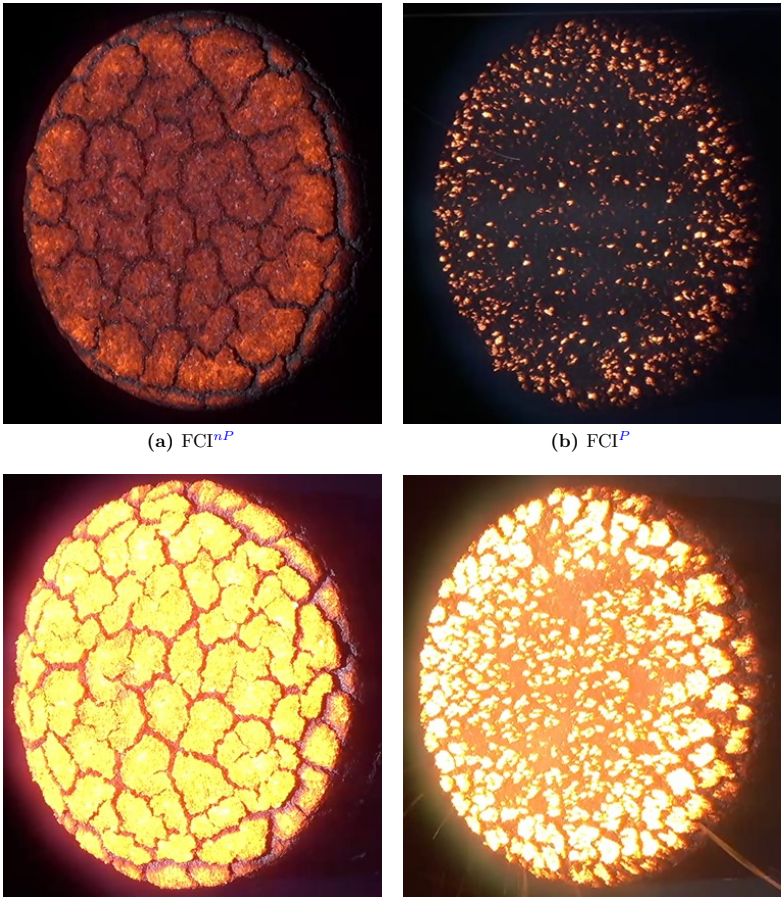

(a) FCI^{nP} **(b)** FCI^{P}

(c) FCII^{nP} **(d)** FCII^{P}

Figure 5.1: Samples during testing in different flow conditions

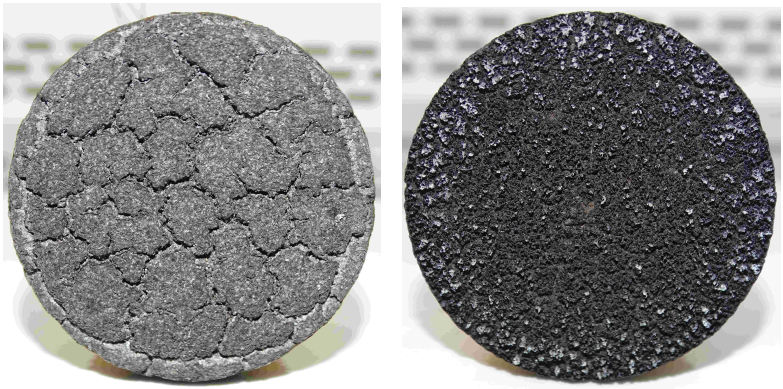

(a) FCI^{nP} **(b)** FCI^{P}

(c) FCII^{nP} **(d)** FCII^{P}

Figure 5.2: Sample surface after testing

By comparing the samples before and after the tests, with and without particles, it is observed that:

- In FCI^{nP}, samples expand more than they ablate, thus the ablation phenomenon is contained. Charring cells are visible.
- In FCII^{nP}, samples experience recession, meaning that the ablation process gains importance over swelling. In this case, the ablation is more severe on the front surface's shoulder region, than in the centre. Cells are visible.
- In FCI^{P}, the erosion phenomenon prevails overall on the whole sample surface: the presence of particles causes recession, which was not observed in FCI^{nP}. Spikes are visible.
- In FCII^{P}, the erosion phenomenon prevails overall in the sample's central region, where spikes are visible. The ablation process might prevail on the erosion process in the front surface's outer region, showing the development of cells. The cells of FCII^{P} are nevertheless smaller than FCII^{nP}, showing that the rupture process of these patterns caused by particle impacts is still playing a role.

To interpret the different distribution of cells and spikes in the different FCs, one should consider the separate coexistent effects of *flow-induced ablation* (caused by pyrolysis, phase change, spallation, shear erosion and chemical reactions, according to section 2.1.4, excluding particle effects) and *particle-induced erosion* (due to the momentum transfer to the probe caused by particle impact). One effect favours the development of charring cells, while the other favours the development of spikes. It may happen that one effect is more prominent than the other due to several reasons. For instance, the samples experience more severe recession in FCII^{P} than in FCI^{P}, especially on the sides; this causes an impact angle reduction that leads to a reduced momentum transfer, thus a reduced particle erosion contribution. In addition, the heat flux of FCII^{P} is higher due to the higher enthalpy and stagnation temperature and pressure, causing increased flow-induced ablation on the material. On top of that, particle density is reduced in FCII^{P} due to agglo-melting. For these reasons, the flow-induced mechanisms might prevail on the particle-induced erosion in FCII^{P}. This prevents the front surface of the samples from being globally eroded, with particle erosion visible only at the centre.

To better assess the material's thermal response, the charred/pyrolysed layer is studied. The samples are sectioned on one of their axial-symmetry planes and the photographs are reported in figure 5.3. FCI^{nP} and FCII^{nP} are compared side by side on the top of the figure, as well as FCI^{P} and FCII^{P}, on the bottom. The dark pyrolysed/charred layer is clearly visible, as well as the virgin material, that shows the characteristic cork composite colour. The non-virgin layer is approximately 2-3 mm thick, and it is slightly thicker in FCI^{nP} than in FCII^{nP}. On the other hand, it looks thinner in FCI^{P} than FCII^{P}. However, one should note that in FCs^{nP} the charring cells keep their structural integrity after the test, whereas the spikes created by particle erosion are very brittle and fragile, and might

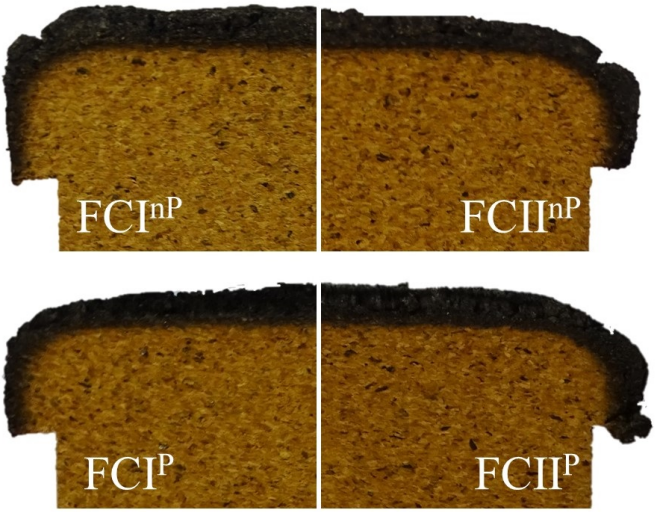

Figure 5.3: Samples' axial-symmetric sections. Pictures are translated vertically to match the location of the virgin material

have fallen off after the tests. For this reason, a quantitative analysis of the charred layer thickness can be done for FCs^{nP} only. Nevertheless, the thinner charred surface in FCI^{P} is in agreement with the previously discussed scenario, regarding figure 5.2b. In fact, higher particle density and particle velocity in FCI^{P} causes higher erosion: more spikes are created, making the surface more brittle and fragile than in FCII^{P}. By comparing samples' sides, one can also observe that the sample is more charred in FCII$^{P/nP}$ than in FCI$^{P/nP}$, due to the higher heat flux of the higher enthalpy flow condition.

The charred layer can be observed with X-rays, as shown in figure 5.4. In fact, the phenolic resin evaporation during charring leaves micro-holes in the material, reducing its optical depth. This causes more X-ray power to be transmitted by the charred layer, which appears brighter than the virgin one. In the figure, FCI^{nP} and FCII^{nP} are compared side by side. Only conditions without particles are reported due to the reasons discussed previously. The background (i. e. the region with the highest signal) was marked red, and the contrast was optimised to highlight the difference between the virgin material and the charred/pyrolysed layer, whose thickness was measured with image processing. Since the char thickness is not uniform over the whole section of the image, several measurements were taken in the central part of the sample, and averaged. FCI^{nP} has a 2.5 mm thick

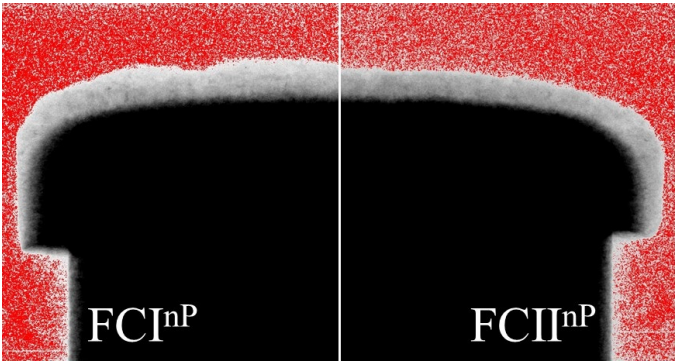

Figure 5.4: X-Rays of tested samples. Noise is marked in red, black and grey regions are virgin and non-virgin material respectively. The two pictures are translated vertically to match the location of the virgin material

charred layer, while FCII^{nP} has a 2.0 mm thick charred layer: the higher enthalpy of FCII^{nP} causes higher heat flux on the sample and higher flow velocity, which increase the ablation processes mentioned in section 2.1.4, with respect to FCI^{nP}. This causes in the end an increased recession rate.

5.2 Sample Temperatures

In this section, the aspect of surface temperature is investigated, followed by the presentation of the in-depth temperature measurements.

5.2.1 Surface Temperature

The surface temperature was measured with a one-colour pyrometer (1cP), a two-colour pyrometer (2cP), and an IR camera. The grey-body assumption is a common simplification to describe a real surface that emits and absorbs thermal radiation like a blackbody, but with an emissivity less than 1 and independent of wavelength. In reality, emissivity is a spectral property—it varies with wavelength—and it may also change with temperature. For instance, the surface oxidation processes at high temperature might be one of the causes of this variability. When examining these data, the change in surface emissivity might represent a significant criticality during analysis. In this context, one might expect the two-colour pyrometer to provide a more reliable temperature estimate, owing to its

measurement principle: it detects thermal radiation at two distinct wavelengths and computes the temperature from the ratio of the corresponding intensities. This method inherently compensates for uniform emissivity variations and partial optical obstructions, to which the one-colour pyrometer and the infrared camera are more sensitive. However, the emissivity compensation is only valid if the emissivity changes identically at both measured wavelengths—a condition that cannot be guaranteed in this high-temperature case. Therefore, given the uncertainty associated with the emissivity of the material, which was assumed as 1 to provide a lower bound for the temperature, the resulting temperature estimates carry an unknown bias. This bias would be constant if the emissivity were truly constant; however, transient phenomena cause the emissivity to vary in time and space. The magnitude of this variation is not directly measurable in the current experiments, so the exact uncertainty in the temperature cannot be quantified.

The results in FCs^{P} are characterised by peculiar behaviours in terms of surface temperature measurements. To understand the reason behind this, it is worth to observe the surface temperature evolution of the different probes recorded with the IR camera, which is reported in figures 5.5a and 5.5b, for FCI$^{P/nP}$ and FCII$^{P/nP}$, respectively. The bottom parts of the sub-figures represent the surface temperature evolution when no particles are loaded in the flow, while the top parts show conditions with particles.

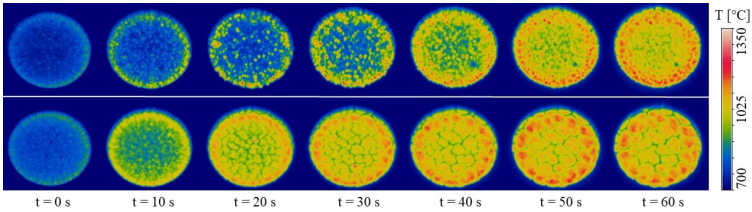

(a) FCI^{P} (above) and FCI^{nP} (below)

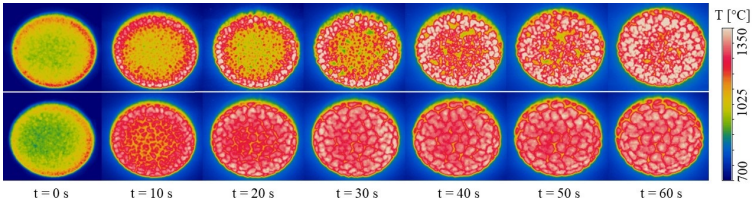

(b) FCII^{P} (above) and FCII^{nP} (below)

Figure 5.5: IR data

One can observe that the surface temperature without particles is quite uniform: the surface presents cracks that delimit the charring cells, whereas the temperature increase

follows a rather homogeneous behaviour. On the other hand, the tests with particles show less uniformity. In this case, the charring cells do not appear as clearly as in the conditions without particles. This is due to the erosion phenomenon that causes surface layer rupture and cork particles release, which are carried away by the flow. This process exposes the underlying cork layers, which are colder, as observed especially in the first part of the test.

The surface temperature of the samples' central point is reported in figures 5.6 and 5.7, for FCs^{nP} and FCs^{P} respectively. In the figures, the data from the 1cP, the 2cP, and the IR camera are reported. The IR data are extracted from each IR image at the sample centre, by taking the average value within a 5×5 px^2 window, to better compare it with pyrometry data. For FCs^{P}, an additional exemplary extraction window is selected in the IR data to highlight erosion phenomena, i. e. discontinuities in the surface temperature, and it is reported as a dotted line.

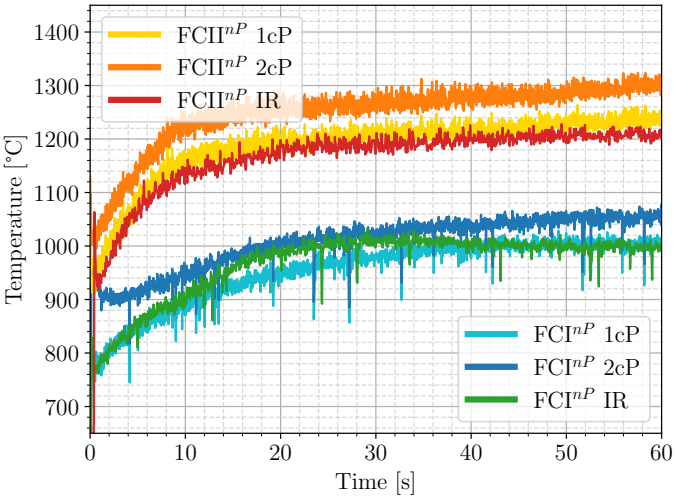

Figure 5.6: Surface temperature measurements in FCI^{nP} and FCII^{nP}: one- and two-colour pyrometers (1cP, 2cP) and infrared camera (IR)

In FCs^{nP}, one can observe that:

- The temperature measurements from the 1cP and the IR camera are in close agreement, with discrepancies within approximately 2%, which is within the instruments' noise fluctuations. The 2cP shows slightly larger differences compared to the one-colour pyrometer, with discrepancies within about 6%. These deviations are

considered acceptable, as the IR camera and 1cP data were processed assuming an emissivity of 1, providing a lower-bound estimate of the surface temperature, and the observed differences remain consistent with expected uncertainties from emissivity assumptions.

- In FCI^{nP}, the two-colour pyrometer has a peculiar overshoot at the beginning of the test. This behaviour may arise from the different spectral ranges to which the pyrometers are sensitive. One can hypothesise that the surface emissivity varies with wavelength at the beginning of the test, possibly due to oxidation or other transient surface processes, causing the two channels to record different temporal responses.
- Temperatures in FCII^{nP} are higher due to the higher flow enthalpy, as expected.
- The trends are smooth and follow an asymptotic behaviour.

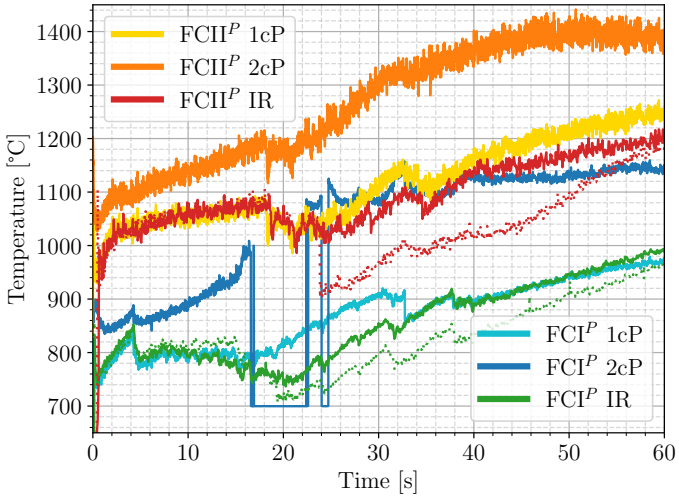

Figure 5.7: Surface temperature measurements in FCI^P and FCII^P: one- and two-colour pyrometers (1cP, 2cP) and infrared camera (IR; the dotted lines represent peculiar spots in the IR camera frames that highlight an erosion event)

In particle-laden conditions, due to the stochastic location and instant of each erosion event, it is difficult to observe perfect quantitative repeatability on the data, but it is possible to identify common phenomena: in this sense, the tests are considered qualitatively repeatable. In particular:

- The two-colour pyrometer in FCI^{P} shows a peculiar overshoot at the beginning of the test, as in FCI^{nP}. Moreover, the qualitative trends at lower temperature differ between 1cP and 2cP, possibly due to the emissivity change caused by oxidation processes.
- The surface temperature does not present the smooth behaviour observed in the FCs^{nP}, showing several discontinuities for all presented cases. The discontinuities are due to the erosion phenomena that expose the colder underlying layers, as explained before. These events are indeed always characterised by a temperature decrease in the measurement points.
- The two-colour pyrometer in FCI^{P} shows a large discontinuity after $t = 16$ s, where it records a constant temperature of 700 °C (this is the lowest measurable temperature of the pyrometer). This effect is caused by a violent erosion event, as seen also in figure 5.5a.
- The surface temperature in FCII^{P} is overall higher than in FCI^{P}, as expected due to the higher enthalpy of FCII^{P}.
- At the end of the tests, the surface temperature of FCs^{P} is overall higher than FCs^{nP}. This effect might be caused by the heat transfer enhancement provided by the rougher eroded surface, and by the heating augmentation effects described in section 2.2.

The surface temperature measurements in this case do not "match nicely" as observed in figure 5.6, meaning that both qualitative trends and quantitative agreement are less consistent. However, the temperatures measured by the 1cP and the IR camera remain consistent (discarding the dotted IR lines representative of erosion), with discrepancies within approximately 2%, which is within the expected noise fluctuations. The mismatch between one- and two- colour pyrometry is due to the fact that these types of measurement highly depend on the material's emissivity, which is affected by the following phenomena:

- Exposure to the high-temperature flow at the beginning of the test may trigger transient phenomena, such as oxidation, which can strongly affect the surface emissivity.
- The erosion process causes inhomogeneity in the surface properties, by removal of the charred material and exposure of the virgin cork. This leads to a significant emissivity variation, which might cause the two different pyrometers to lose their match.
- When particles are present in the flow, they deposit on the sample, thus forming a surface layer that changes surface properties. The deposition rate and thickness are unknown, and for this reason it is not trivial to estimate the surface emissivity, which was kept as 1 during the evaluation process.

- Particles can represent optical obstructions, which the one-colour pyrometer and the IR camera are particularly sensitive to, as they represent a signal attenuation which is interpreted as a lower temperature. For the two-colour pyrometer, if the particle-induced attenuation affects both wavelengths similarly, the evaluated temperature remains nearly unchanged. However, if particle scattering/absorption is wavelength-dependent (common for small particles, due to Mie scattering effects), then errors also occur in this measurement technique.

5.2.2 In-Depth Temperature

Only the first thermocouple records a significant temperature increase in all tests, and for this reason only its data are reported, while deeper thermocouples are disregarded. The first thermocouple lies nominally at 6 mm from the surface, while the others lie at 12 mm and 18 mm, as mentioned in section 3.2. The actual location of the thermocouples was measured by processing the X-ray pictures. It was observed that in reality thermocouples lay at different depths for all samples (from 6.4 mm to 8.6 mm), due to misplacement during manufacturing and instrumentation. Since the cork's thermal conductivity is very low, one must carefully compare the presented data, as a few tenths-of-mm misplacement could lead to significantly different measured temperature, especially with such short testing times[1]. Due to the significant misplacement, the in-depth temperature is reported for all 10 tests in figure 5.8, colour-coded by flow condition. In the legend, each thermocouple's measured depth is reported: one shall compare only thermocouples at the same depth. More tests might be required to build a significant statistical population regarding thermocouple data. It is however still possible to observe characteristic phenomena in the results.

The recorded in-depth temperatures can be compared for the following conditions:

- Test *1* (FCI^{nP}) with test *3* (FCI^{P})—thermocouple depth 7.0 mm: FCI^{nP} records a higher temperature than FCI^{P} until $t = 50$ s; then an inversion happens. The lower surface temperature observed at the beginning of tests with particles is likely due to the violent erosion of the hot surface layers, which inhibits heat conduction to the surface. Furthermore, as the underlying virgin material becomes exposed, the initiation of swelling and ablation processes—both endothermic in nature—can absorb additional heat, further contributing to the reduction of the surface temperature. The erosion process then reduces the thermocouple depth in FCI^{P}, leading to a violent temperature raise toward the end of the test. The temperature inversion is seen also by comparing test *1* with *4*, even though a depth difference of 0.2 mm was measured.

[1] Longer testing times are not possible at this stage of the study, due to the limited capability of the particle generator. Further improvements should be made on the facility to increase testing times with particles.

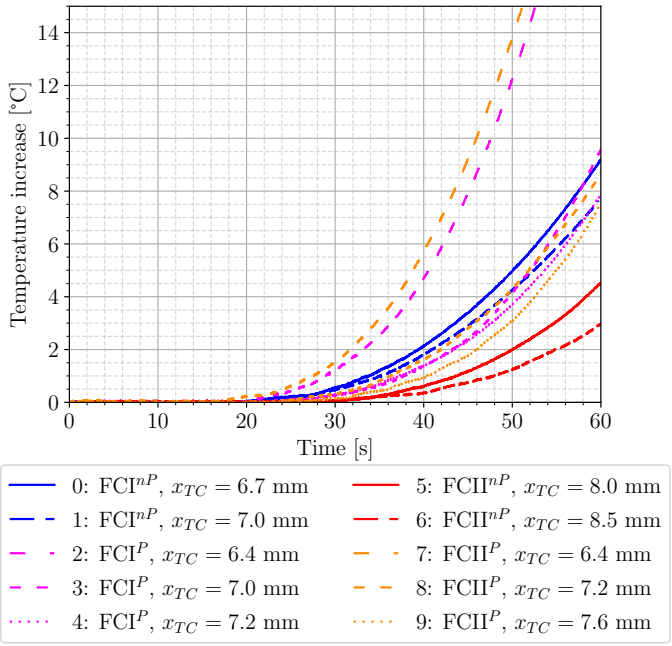

Figure 5.8: In-depth temperature increase at the shallower thermocouple for all 10 tested probes. The thermocouple depth x_{TC} is measured with X-rays. Thermocouples whose depth differ more than 0.5 mm should not be compared

- Test *2* (FCI^{P}) with test *7* (FCII^{P})—thermocouple depth 6.4 mm—and test *4* (FCI^{P}) with test *8* (FCII^{P})—thermocouple depth 7.2 mm: FCI^{P} and FCII^{P} show very similar trends at both depths; FCII^{P} is always hotter than FCI^{P}—as expected due to the higher flow enthalpy.

While Figure 5.8 might suggest a lack of repeatability, this apparent variability primarily reflects unavoidable thermocouple placement tolerances rather than differences in the physical response of the samples. To meaningfully compare the data, it is therefore necessary to consider a fixed point in time (e.g., $t_{end} = 60$ s) and plot the temperature values of the different tests versus the thermocouple depth, as shown in Figure 5.9, colour-coded by flow condition. The graph thus represents a "frozen-in-time" state, which might change depending on the selected observation time: for instance, if the observation was made at $t = 40$ s (before the temperature inversion phenomenon), the FCI^{P} conditions

would show lower temperature than FCI^{nP}. The choice of presenting the highest possible observation time reflects the fact that heat shields may survive atmospheric entry, which might last several minutes, and the end result is what matters for EDL heat shield design purposes. Note that test *8* experienced insufficient particle loading, characterized by only two isolated particle bursts, a lower overall particle count, and intervals with no particles, as evident from the results presented in chapter 6. However, it is reported here for completeness.

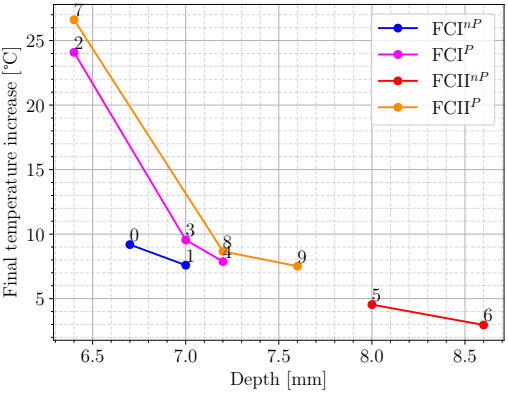

Figure 5.9: Final in-depth temperature increase at the shallower thermocouple for all 10 tested probes. The thermocouple depth x_{TC} is measured with X-rays. Thermocouples whose depth differ more than 0.5 mm should not be compared

Even though the data population is quite limited, one can appreciate few features:

- FCI^{P} records higher final temperature than FCI^{nP}.
- FCII^{P} cannot be significantly compared with FCII^{nP} due to the large thermocouple depth difference. By studying more samples, FCII^{P} would most likely record higher final temperature than FCII^{nP}, as confirmed by all evidences previously reported in this section.
- FCII^{P} records higher final temperature than FCI$^{P/nP}$.

The generation of high-enthalpy flows with constant particle flow rates is a challenge. The temperature data and the LPT data presented in the next section show that a large part of particle-induced erosion events happen in the first 30 seconds of the tests, whereas the following 30 seconds are characterised by less violent particle-induced phenomena. This is due to the non-constant particle flow rate, which is reported in chapter 6. According to the different particle flow rates between tests, the time-varying erosion effect may

differ. Thus, the insulating cork layer between the embedded thermocouples and the probe's surface can present a different time evolution for every particle-laden test. This could lead to different increase of the in-depth temperature.

5.3 Thickness Evolution Measurements

The overall thickness evolution E—a result of combined ablation and swelling—evaluated by analysing 3D scans, is reported in figure 5.10. FCI$^{P/nP}$ and FCII$^{P/nP}$ are presented in figures 5.10a and 5.10b respectively, by using the same scale for all pictures, for a clearer comparison: positive values (colour-scale) indicate overall recession, while negative values (greyscale) indicate that the sample has swollen more than it has recessed during the test. Note that these results are not time-resolved, and it is therefore impossible to characterise the sample behaviour during the test by looking at the scans only.

It is possible to observe that:

- FCs^{P} are generally more recessed than FCs^{nP}, in both the high-enthalpy and in the low-enthalpy flow condition. This is due to the particle-induced erosion effect, where momentum transfer from the particle to the sample causes removal of its surface layer, enhancing recession.
- FCII$^{P/nP}$ is generally more recessed than FCI$^{P/nP}$. This is due to the fact that the higher enthalpy of FCII$^{P/nP}$ provides a higher heat flux, that causes a more severe ablation of P50.
- FCI^{nP} has swollen more than it has recessed. The recessed regions correspond to the cracks between charring cells, which are more pronounced on the sides.
- FCII^{nP} has recessed more than it has swollen, except for the very central part.
- FCs^{P} present only positive evolution values, indicating that recession wins over swelling in the presence of particles.

The observed swelling of the ablative material can be interpreted as the combined result of thermal expansion and pressure-driven outgassing of pyrolysis products, which occur on different time scales. While thermal expansion follows the rapid temperature increase, swelling is likely dominated by gas generation within the material, where pyrolysis gases accumulate beneath the surface and locally increase pressure. This pressure buildup can mechanically "blow up" or lift the surface char layer, producing the observed swelling. Under higher heat-flux conditions, such as in FCII^{nP}, enhanced pyrolysis generates larger amounts of gaseous products; however, the earlier formation of cracks increases the effective outgassing surface area. The resulting pressure release reduces gas accumulation beneath the char layer, thereby limiting swelling despite the stronger thermal loading.

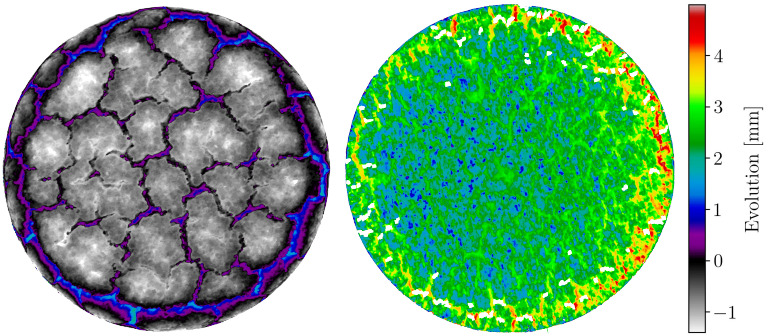

(a) FCI^{nP} (left) and FCI^{P} (right)

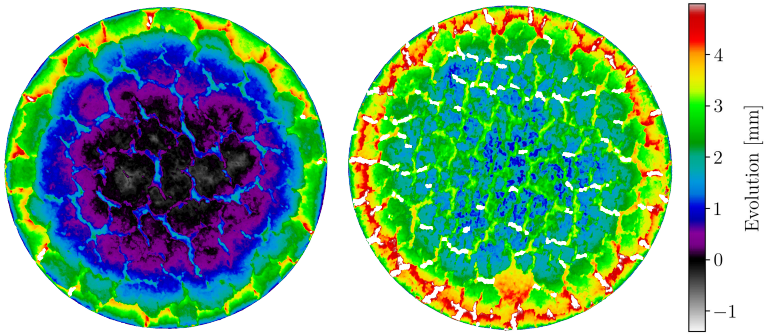

(b) FCII^{nP} (left) and FCII^{P} (right)

Figure 5.10: Sample overall evolution from 3D surface scans

Conversely, under lower heat-flux conditions (FCI^{nP}), slower crack development may confine gases for longer times, allowing pressure to build up and leading to more pronounced swelling. This interpretation suggests that swelling is governed not only by the rate of pyrolysis but also by the balance between gas production and pressure relief through cracking and surface recession.

In all tests, the probes' recession is more severe on the sides than on the centre due to the sample geometry, that causes the cold-wall heat flux to peak close to the samples' shoulder, as theorised in [54]. In this small region, the pressure gradient causes a thinning of the temperature boundary layer, resulting in an increased heat flux. In addition, the bow shock is here closer to the surface, causing an increased temperature gradient, i.e. heat flux. Finally, the higher flow speed in correspondence of the shoulder increases the shear erosion contribution to the ablation phenomenon.

The time-resolved evolution measured with LPT is reported in the y/t space, in figures 5.11a and 5.11b, for FCI$^{P/nP}$ and FCII$^{P/nP}$, respectively. The same data are reported in the E/t space in figures 5.12a and 5.12b, for FCI$^{P/nP}$ and FCII$^{P/nP}$ respectively. A large y-dependent spread of the evolution value is observed especially in the tests with particles. For this reason, only the central region of the sample ($|y| < 10$ mm) is reported in the E/t figures to better visualise the results.

The LPT measurement at $t_{end} = 60\,\text{s}$ shows good agreement with the 3D surface scans. Although a direct quantitative comparison is limited (since the 3D scans provide a 2D measurement and the LPT data are 1D), the overall trends and values match to within approximately 0.1–0.2 mm. Consequently, the observations derived from the 3D scans regarding overall surface recession at t_{end} can also be considered valid for the LPT data, as the LPT measurements capture the same final surface profile while providing additional time-resolved information. The added value of this measurement technique is the time resolution of evolution behaviour:

- In FCI^{nP}, the probe experiences swelling only.
- In FCII^{nP}, the probe swells at the beginning of the test, and after approximately 20 seconds it starts recessing.
- In FCI^{P}, the probe recesses rapidly at the beginning of the test, and it experiences swelling after approximately 30 seconds. This might be due to the non-constant particle flow rate reported in chapter 6.
- In FCII^{P}, the probe recesses rapidly at the beginning of the test, and it keeps recessing until the end.

In both the E/t and y/t graphs, some peculiar features are observed in the data:

- In the tests with particles, several outliers are observable. These are due to the processing algorithm that can recognise a bright particle as the probe's profile,

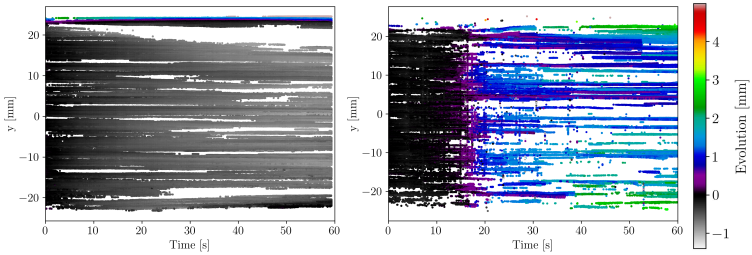

(a) FCI^{nP} (left) and FCI^{P} (right)

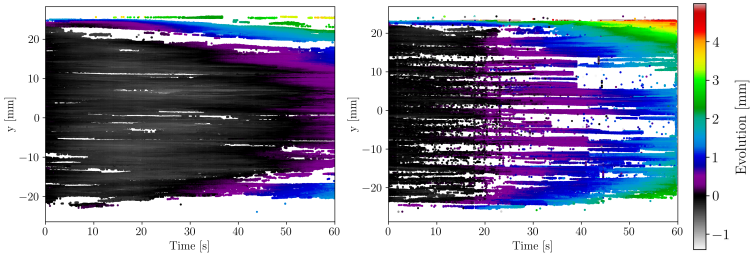

(b) FCII^{nP} (left) and FCII^{P} (right)

Figure 5.11: Time-resolved thickness evolution measurement (y/t space)

computing largely negative evolution values that do not make physical sense. In fact, the particle is upstream of the probe's surface, thus the algorithm "thinks" that the probe is expanding. This happens only with very bright particles. The outliers are not present in tests without particles.

- Due to the surface morphology, which can be characterised by cells, spikes and cracks, the data present "holes" in all tests, namely blank spots (or NaN) where the algorithm cannot identify the profile outline. In these points, the light-sheet reflection is not visible to the camera, because its sight might be blocked by surface features (for instance, a crack that delimits a cell can be hardly visible, as the cell blocks the light propagation), which cause a *shading effect*. Since this is a physical effect, no interpolation is performed between valid data, as it might introduce errors: holes give, somehow, an information.
- The large spread of the evolution in the tests with particles is due to the roughness caused by erosion. The surface spikes shown in figure 5.2b generate indeed surface levels that can differ several millimetres in the x-direction. In other words, spikes caused by particle impact make the result less smooth than in the FCs^{nP}.

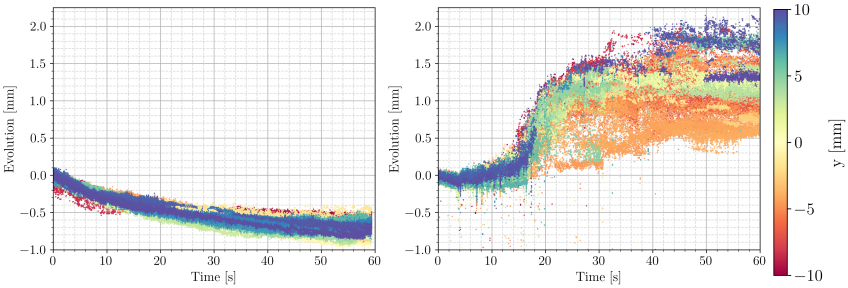

(a) FCI^{nP} (left) and FCI^{P} (right)

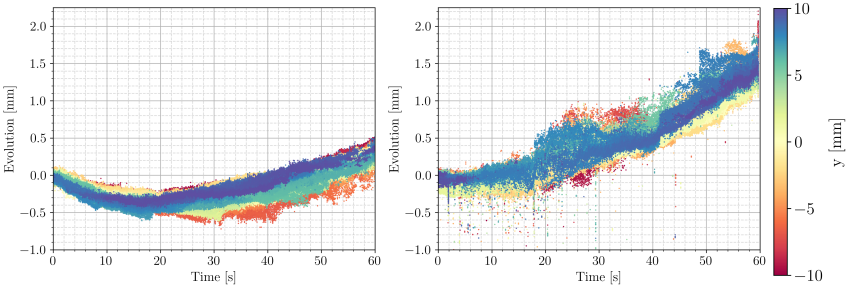

(b) FCII^{nP} (left) and FCII^{P} (right)

Figure 5.12: Time-resolved thickness evolution measurement in its central region, $|y| <$ 10 mm, (E/t space)

- The spikes of FCs^{P} also represent additional surface features which lead to more data holes, caused by shading.

By comparing the surface temperature data in figure 5.5 with the LPT data in figure 5.12 in the cases with particles, one can observe that the large recession at the beginning of the test matches with the formation of the eroded-colder patterns in the IR data.

Future developments should focus on making the algorithm more robust when particles are present in the flow. The geometry of the experimental setup could be optimised to obtain less holes in the data, for example by having the main laser propagation direction almost perpendicular to the sample surface, thus reducing the shading effect.

5.4 Summary and Future Steps

The performance of P50 cork was studied in the four flow conditions object of this study, through several measurement techniques: IR thermography (two-colour pyrometer, one-colour pyrometer and IR camera), embedded thermocouples, video monitoring, X-rays, and thickness evolution measurements (3D surface scans and LPT). The newly developed LPT technique was proved effective, by comparison with 3D scans. The presence of particles has an evident effect on the cork's ablation and swelling, and on the recorded temperature. Particles erode the samples' surfaces by momentum transfer, and their effect can be seen in both time-resolved and overall thickness evolution data.

The surface temperature data show very repeatable and smooth results in the tests without particles, and they show peculiar behaviours in the tests with particles. Several discontinuities were recorded in surface temperature data, which are caused by erosion phenomena, where the surface layers are removed exposing a colder underlying layer. The uncertainty in the modelling of the wavelength-dependent emissivity change—generated by complex transient processes, oxidation, particle impact, and material response under high-temperature conditions—lead to a mismatch between one-colour and two-colour pyrometer data. The comparison of the in-depth temperature data shows that conditions with particles might be colder at the beginning of the test with respect to particle-free conditions, but they become hotter with longer testing times. This temperature inversion is caused by the fact that erosion phenomenon removes the hotter surface layers, blocking heat conduction at the beginning of the test. In any case, the conditions with particles record the highest in-depth temperatures for testing times comparable to atmospheric entry (figure 5.9).

During tests with particles, different time-dependent thickness evolution of each sample was observed, caused by the erosion events' randomness: the presence of particles introduces a significant uncertainty in the prediction of the thickness evolution rate, caused by recession and swelling. When designing a cork-based heat shield for a Martian EDL module, one needs to provide robustness to atmospheric entry in a dust-laden atmosphere, and a proper safety factor must be used to design the shield's thickness, since particle erosion on cork-based ablators is not negligible.

- Additional campaigns should be performed for in-depth temperature characterisation, by selecting different thermocouple depths (for instance 3 mm, 5 mm and 7 mm), and by ensuring their correct placement during the manufacturing and instrumentation processes. In fact, maximum accuracy is required due to the high complexity of the topic. More tests are required to build a more significant statistical population for the comparison of the in-depth temperature.
- Further studies should be performed to assess the in-depth temperature behaviour, and in particular the temperature inversion phenomenon linked to the recession

rate. In addition, one should investigate if the temperature in FCI^{nP} becomes higher than FCII^{nP} at the beginning of the test. This might be due to the increased ablation in FCII^{nP}, that provides more efficient heat dissipation by hot mass loss.

- In the future, the seeding should be improved to increase testing times with particles.
- Regarding the LPT processing algorithm, more robustness to particle-laden flow conditions is required. The setup may be geometrically optimised to reduce the blank regions.
- Future studies should investigate different materials in the same flow conditions, such as carbon-based ablative materials like ZURAM.

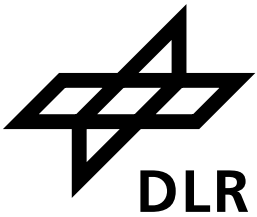
DLR

6 Data-Based Thickness Evolution Model

This chapter integrates the flow-field characterisation and material-response studies by formulating a model that reproduces the experimentally observed thickness evolution, while also providing a framework that could be extended for predictive analysis of ablator behaviour in dusty high-enthalpy environments. A 1D model capturing the coupled processes of swelling, recession, and particle-induced erosion is proposed and validated using experimental data, enabling correlation between the particle flux (measured through SL-PIV data) and the erosion rate (determined via LPT). Through this analysis, a proportional relationship between particle flux and erosion rate is established, highlighting the influence of particle loading on material response. Additionally, the study identifies a previously unreported phenomenon, termed *post-erosion swelling*, in which intermittent particle bursts enhance surface swelling under mild and unsteady seeding conditions. While the model is currently employed to describe and interpret experimental observations, the approach is designed to be extended in future work for predictive applications across different materials and flow conditions.

6.1 Mathematical Model

The sample thickness evolution can be described by the sample surface's position $Y(t)$, with $Y(t_0) = 0$ mm. In particular, negative Y is associated to swelling, while positive Y to recession—in agreement with the data presented in the previous chapter—as presented in figure 6.1. The model is 1D.

The main assumptions of the model are:

1. The recession rate $\frac{dY}{dt}$ is dependent on several components; the first is proportional to the distance between the sample surface Y from a general equilibrium surface Y_{eq}.

$$\left(\frac{dY}{dt}\right)_1 = -k\left(Y(t) - Y_{eq}(t)\right) = -k\Delta Y \tag{6.1}$$

   One can for instance visualise ΔY as directly related to the surface layer, where the virgin cork transforms to pyrolysed material and ultimately char, before being ablated away. ΔY does not necessarily coincide with the charring thickness.

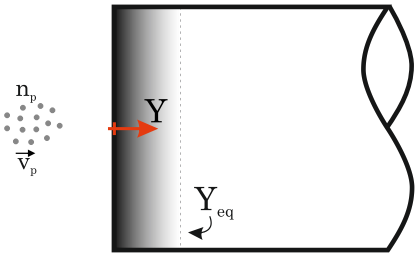

Figure 6.1: 1D surface evolution model

2. The second component of the recession rate is provided by particle-induced erosion. This effect is directly proportional to the number of particles $n_p(t)$, as demonstrated in equation (3.2), assuming constant and homogeneous particle velocity, constant particle properties (density and size), constant material properties, homogeneous seeding, and quasi-perpendicular impact.

$$\left(\frac{dY}{dt}\right)_2 = \frac{dY^e}{dt} = A\, n_p(t) \tag{6.2}$$

3. The total evolution rate is the sum of the mentioned effects, assuming linearity.

$$\frac{dY}{dt} = \left(\frac{dY}{dt}\right)_1 + \left(\frac{dY}{dt}\right)_2 = -k\,(Y(t) - Y_{eq}(t)) + A\, n_p(t) \tag{6.3}$$

With k depending on the flow condition (stagnation temperature, mass flow rate, enthalpy) and the material response (charring thickness, recession rate, swelling rate), and A depending on the particle momentum and the material properties, as for equation (3.3). Both proportionality factors are positive.

The equilibrium surface location Y_{eq} can be modelled in different ways, depending on the expected material behaviour. It is reasonable to hypothesise that Y_{eq} is time-varying, depending on the flow conditions and on the probe material. In this configuration, Y_{eq} depends mainly on swelling (^{s}), recession (^{r}), and erosion (^{e}) effects. Hypothesising linearity between these phenomena:

$$Y_{eq}(t) = {Y_{eq}}^s(t) + {Y_{eq}}^r(t) + {Y_{eq}}^e(t) \tag{6.4}$$

From [9, 101], cork-based ablators present a non-linear behaviour at the beginning of the test where they experience swelling; they then start receding with a constant recession rate on the long term. For this reason, the time evolution of the equilibrium surface can

be modelled as a straight line with positive slope and negative y-intercept: the negative starting value of Y_{eq} causes Y to move to negative values (which represents swelling with decreasing exponential trend) at the beginning of the test, and the positive constant slope leads the system to a positive constant recession rate on the long term. In this configuration:

$$Y_{eq}{}^{s}(t) + Y_{eq}{}^{r}(t) = at + b \tag{6.5}$$

where $a > 0$ and $b < 0$.

Particles were observed to have a direct effect on Y_{eq}. Their impacts drive Y to jump sharply toward positive values (i. e. particle-induced erosion, modelled by An_{p}), violently striping the surface char away, directly affecting $\Delta Y = Y$ - Y_{eq}. As the virgin layer is exposed, Y_{eq} is pushed back towards negative values, as the swelling phenomenon is favoured. In other words, the virgin material is exposed to the flow and "wants" to swell. At this stage of the study one can hypothesise that Y_{eq} is decreased by the same amount that the probe has eroded due to particles, that is:

$$Y_{eq}{}^{e}(t) = -\int_0^t A\, n_{\mathrm{p}}(\tau)\, d\tau \tag{6.6}$$

The negative sign highlights that this effect favours swelling. This phenomenon was never reported in the literature and is defined as post-erosion swelling.

In the current form, a severe particle burst can lead to a sharp decrease in ΔY, which results in a negative Y rate with large magnitude. If the effect is pronounced, the magnitude could become non-physically high, causing a swelling rate higher than the swelling rate at the beginning of the test—which is a physical limit. For this reason a constraint on Y_{eq} needs to be imposed such that $\Delta Y(t)$ can never be larger than $\Delta Y(t_0)$:

$$\Delta Y(t) \leq \Delta Y(t_0) = -b \qquad \Rightarrow \qquad Y_{eq}(t) \geq Y(t) + b \tag{6.7}$$

The model is formulated as a constrained linear, first-order, inhomogeneous ordinary differential equation (ODE) with a time-dependent forcing term involving an integral, solvable through the corresponding initial value problem (IVP):

$$\begin{cases} \frac{dY}{dt} = -k\left(Y(t) - at - b + \int_0^t A\, n_{\mathrm{p}}(\tau)\, d\tau\right) + A\, n_{\mathrm{p}}(t) \\ Y(t_0) = 0 \text{ mm} \end{cases} \tag{6.8}$$

The IVP's general solution, without the mathematical constraint proposed in equa-

tion (6.7) yields:

$$Y(t) = e^{-kt}\left[Y_0 + \int_0^t e^{ks}\left(k\left(as + b - A\int_0^s n_\mathrm{p}(\tau)d\tau\right) + An_\mathrm{p}(s)\right)ds\right] \tag{6.9}$$

$$= e^{-kt}\Bigg[\underbrace{Y_0}_{\text{initial condition}} + \underbrace{ka\int_0^t se^{ks}ds}_{\text{recession}} + \underbrace{kb\int_0^t e^{ks}ds}_{\text{swelling}} + \underbrace{-kA\int_0^t e^{ks}\left(\int_0^s n_\mathrm{p}(\tau)d\tau\right)ds}_{\text{post-erosion swelling}} + \underbrace{A\int_0^t e^{ks}n_\mathrm{p}(s)ds}_{\text{particle-induced erosion}}\Bigg] \tag{6.10}$$

In its explicit form (solving the integrals):

$$Y(t) = \underbrace{a\left(t - \frac{1-e^{-kt}}{k}\right)}_{\text{recession}} + \underbrace{b\left(1-e^{-kt}\right)}_{\text{swelling}} + \underbrace{-A\int_0^t n_\mathrm{p}(s)\left(1-e^{-k(t-s)}\right)ds}_{\text{post-erosion swelling}} + \underbrace{A\int_0^t n_\mathrm{p}(s)e^{-k(t-s)}ds}_{\text{particle-induced erosion}} \tag{6.11}$$

With this formulation, the solution depends on four terms, each associated to the four effects:

- **Recession** contributes with an exponential decay towards a linear trend with slope a, which is the long-term recession rate.
- **Swelling** contributes with an exponential decay with initial value b.
- **Post-erosion swelling** is caused by the cumulative exposure to particles and it is represented by the convolution of the particle flux $n_\mathrm{p}(t)$ with the kernel $\bar{h}_1(t) = 1 - e^{-kt}$, which accumulates particle effects over time with a saturating memory effect.
- **Particle-induced erosion** is the instantaneous reaction to the particle flux $n_\mathrm{p}(t)$ and it is represented by the convolution of $n_\mathrm{p}(t)$ with the kernel $\bar{h}_2(t) = e^{-kt}$, representing an exponentially weighted instantaneous impact of particles.

Note that the explicit solution is useful for understanding each effect's contribution, but it does not consider the constraint proposed in equation (6.7). Enforcing such constraint during the fitting process requires numerical integration. However, for applications that do not require particle modelling (e.g. Earth reentry), the explicit form can be used directly without numerical solving, by setting $A = 0$.

6.2 Model Discussion

In figure 6.2, qualitative simulations of the described 1D model are presented, with the aim of guiding the reader toward a clearer understanding of its behaviour. In figure 6.2a, the model response is shown for a generic configuration without particles ($n_p = 0$). The dark grey line represents the equilibrium surface evolution, $Y_{eq}(t) = at + b$ from equation (6.5); the red line represents the model solution, $Y(t)$; and the shaded region corresponds to ΔY, which—according to equation (6.1)—is proportional (through the factor $-k$) to the first derivative of Y when no particles are present. In case of no particles:

- Since $-\Delta Y(t_0) = b < 0$, at $t_0 = 0$ s the surface Y is pulled towards negative values (this represents the swelling behaviour).
- In the following few seconds, $-\Delta Y$ is negative, with decreasing magnitude: the first derivative of Y is negative-increasing.
- At the inversion point, when ΔY is zero, Y has a stationary point.
- After the stationary point, $-\Delta Y$ increases up to a constant: combining the explicit solution presented in equation (6.11) with equation (6.5), one finds that the first derivative of Y tends to a, for long testing times. In other words, the long-term slope of the red line (the long-term recession rate) is equal to a. This aspect is convenient while fitting the mathematical model to the data, as the recession rate is easily retrieved during the process.

In figure 6.2b, a generic simulation with particles is presented, for which particles are randomly generated and shown as a green line. In this case, $Y_{eq}(t)$ includes the post-erosion swelling contribution, as reported in equation (6.6):

- $Y_{eq}(t)$ is not a straight line as in the case without particles, as its value is pulled toward negative values—thus favouring swelling—due to the post-erosion swelling effect.
- At the same time, particles give a positive contribution to the derivative of Y, according to equation (6.2). For this reason, Y increases in the presence of particle bursts.
- Particle-induced erosion and post-erosion swelling are two counteracting phenomena: depending on the particle number, one effect may prevail. In fact, the derivative of Y is not always positive in the presence of particles, even though erosion takes place.
- The constraint presented in equation (6.7) forces ΔY—the grey region—below $\Delta Y(t_0)$, to avoid representing a too-high non-physical swelling value.

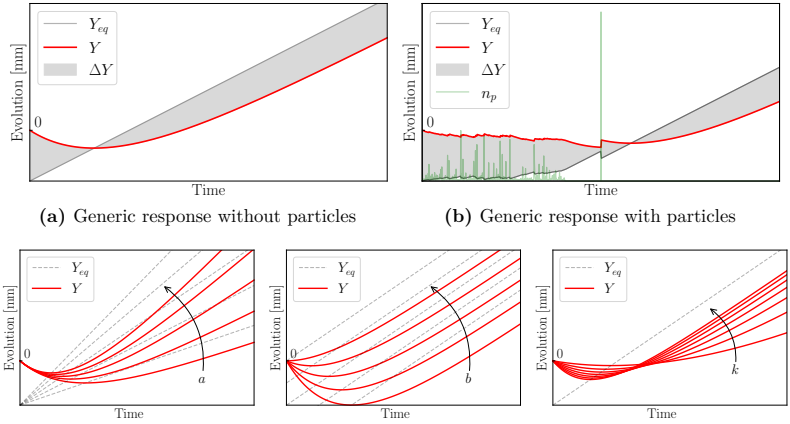

(a) Generic response without particles

(b) Generic response with particles

(c) Influence of a in FCs^{nP}

(d) Influence of b in FCs^{nP}

(e) Influence of k in FCs^{nP}

Figure 6.2: Qualitative model response, influenced by the parameters a, b, and k, and depending on the presence of particles

- After the particle flow is terminated, $Y_{eq}(t)$ resumes its linear behaviour, and Y responds nominally as in the case without particles.

The model parameters a, b, and k have a specific influence on the system response, and they depend on material properties and flow condition. Their effects are illustrated in figures 6.2c to 6.2e, where each parameter is varied individually, considering the particle-free case for simplicity:

- The parameter a is the slope of Y_{eq} and the long-term recession rate, thus defining the slope of Y at the end of the test.

- The parameter b is the Y-intercept of Y_{eq}, and it has a direct effect on the swelling amount, i. e. to what extent the surface Y moves toward negative values at the beginning of the test.

- The parameter k is the system's stiffness and it represents how fast the material reacts to the imposed forcing term ΔY. Response time and swelling amount depend on this parameter.

6.3 Data Fit

The described mathematical model was fitted to bounded LPT data ($|y| \leq 5$ mm)[1], with the particle number n_p measured as mentioned in section 3.3.3, for each run of the experimental campaign. Fitting was performed by numerical integration of equation (6.8), with the following strategy:

1. The model is fitted to LPT data of FCs^{nP} with $n_p(t) = 0$, to retrieve $k = k^{nP}$, $a = a^{nP}$ and $b = b^{nP}$.
2. The model is then fitted to LPT data of FCs^{P}, with the measured $n_p(t)$. During the fitting process, k, a, and b, are bounded such that: $(k, a, b) = (k, a, b)^{nP} \pm 5\%$. The proportionality factor A is thus retrieved for each run with particles.

All 6 runs with particles are reported in figures 6.3 and 6.4, along with one exemplary run without particles. The figures present the raw LPT data, along with their respective fits describing the thickness evolution. Blue colours indicate conditions without particles, and red colours indicate conditions with particles. Additionally, the particle count n_p is shown using green colour scales in three forms: the raw n_p, the Gaussian-smoothed n_p, and regions identified as particle bursts. These are areas where the smoothed n_p exceeds a threshold defined as the mean value of the smoothed n_p plus 1.2 times its standard deviation.

The parameters obtained after fitting in FCs^{nP} are presented in Table 6.1. By comparing the two flow conditions, one can see that the higher heat load provided by FCII^{nP} affects the parameters' values: in the higher enthalpy flow condition, the long-term recession rate a^{nP} is higher, the swelling amount b^{nP} is lower in magnitude, and the system stiffness k^{nP} is higher—meaning that the response to the forcing term $Y_{eq}(t)$ is faster. The evaluated values of a^{nP} are in agreement with the typical recession rates of cork-based ablators. However, at this stage of the study there is a considerable uncertainty on the determination of a^{nP} in the lower-enthalpy flow condition, due to the short test times that did not allow the observation of the constant long-term recession rate, characteristic of cork-based ablators. Future investigations should include longer-duration tests to enable a more accurate evaluation of the governing parameters.

Table 6.1: Fitted model parameters for FCs^{nP}

	FCI^{nP}	FCII^{nP}
a^{nP} [mm/s]	0.024	0.038
b^{nP} [mm]	-2.08	-1.17
k^{nP} [s^{-1}]	0.015	0.030

[1] LPT measurements were restricted to the central region of the sample surface, where physical quantities remain uniform, allowing the thickness evolution to be considered effectively one-dimensional.

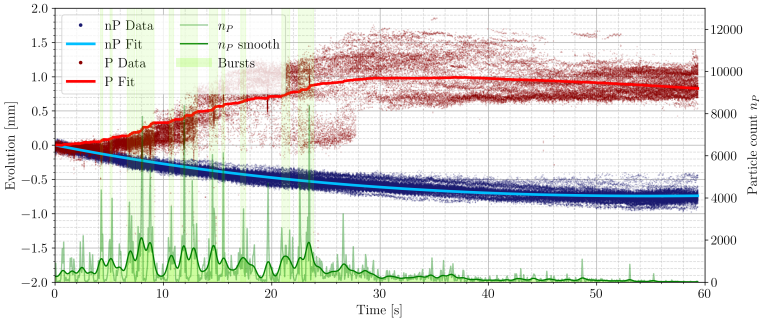

(a) FCI^{P} (Run *2*, A = 5.468e-5) and FCI^{nP} (Run *1*)

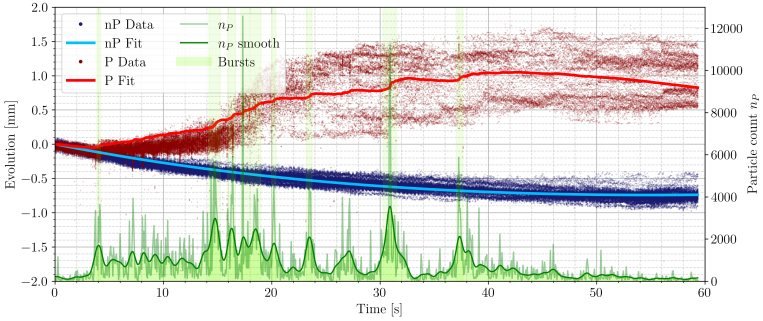

(b) FCI^{P} (Run *3*, A = 5.078e-5) and FCI^{nP} (Run *1*)

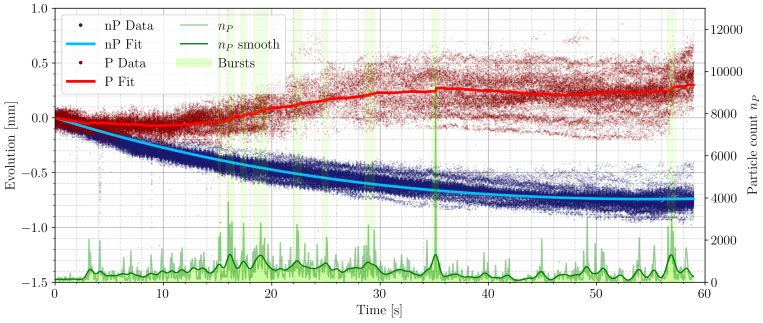

(c) FCI^{P} (Run *4*, A = 5.086e-5) and FCI^{nP} (Run *1*)

Figure 6.3: Results at lower enthalpy, FCI$^{P/nP}$: blue colours indicate conditions without particles and red colours indicate conditions with particles. The particles counted within the light sheet are presented in green, through raw data, Gaussian-smoothed results, and burst regions

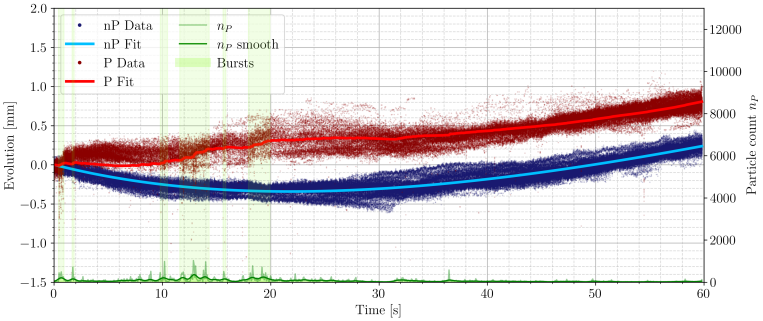

(a) FCII^{P} (Run *7*, A = 3.191e-4) and FCII^{nP} (Run *5*)

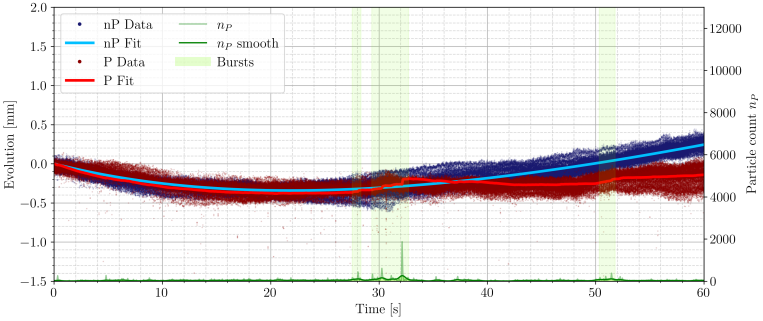

(b) FCII^{P} (Run *8*, A = 4.761e-4) and FCII^{nP} (Run *5*)

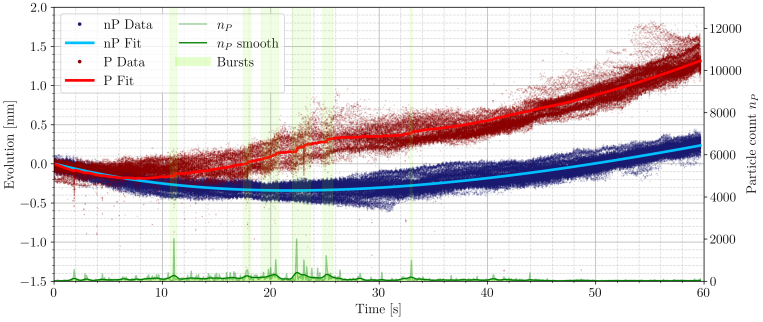

(c) FCII^{P} (Run *9*, A = 2.540e-4) and FCII^{nP} (Run *5*)

Figure 6.4: Results at higher enthalpy, FCII$^{P/nP}$: blue colours indicate conditions without particles and red colours indicate conditions with particles. The particles counted within the light sheet are presented in green, through raw data, Gaussian-smoothed results, and burst regions

By comparing figure 6.3 with figure 6.4, one can observe that the particle count is notably lower in the higher-enthalpy flow condition. This might be an additional evidence of the agglo-melting phenomenon described in section 4.1.1. Moreover, all n_p profiles are not homogeneous and present significant variations: particle flow might be characterised by bursts and it is significantly influenced by the particle seeding generator dynamics. Future studies should aim to improve this hardware component. Given the significant uncertainty in the particle count n_p resulting from the limited optical resolution and sampling frequency, as discussed in section 3.3.3, the results in FCs^P should be interpreted with caution and regarded as qualitative, primarily serving to compare the different flow conditions.

As can be seen in figure 6.3, run *4* had less violent particle bursts, causing a less-pronounced thickness evolution, compared to runs *2* and *3*. In runs *2* and *3*, on the other hand, the first 20 seconds were highly loaded with particles that caused violent erosion. This phenomenon did not start at the beginning of the highly loaded phase due to the fact that the material requires a start-up time to develop a brittle char layer. The model fits well to run *4* and has a slight error at the beginning of runs *2* and *3*. This might be due to the fact that the current mathematical model considers no start-up processes in terms material properties, which are hypothesised constant throughout the test. Nevertheless, it well represents the erosion events recorded with LPT, such as for example the one in run *3* at $t = 31$ s. Values of A are coherent between FCI^P runs, with an average value of $A = 5.211\text{e-}5 \pm 3.5\%$.

In figure 6.4, the model well represents runs *8* and *9*, while it has a slight deviation at the beginning of run *7*, probably for the same reason mentioned for the previous figure (start-up processes). Most notably, run *8* had a very small particle flux, that did not cause any pronounced erosion effect, except for $t = 31$ s and $t = 51$ s. On the contrary, post-erosion swelling caused the probe to be more swollen than in the case without particles. The model well represents this behaviour and is thus a confirmation that post-erosion swelling may be a physical effect, which was never mentioned in the literature regarding two-phase high-enthalpy flows effects on materials. Values of A are not coherent between FCII^P runs: $A = 3.497\text{e-}4 \pm 26.7\%$. The high standard deviation between values of A can be another evidence of agglo-melting: the change in particle size distributions requires dropping the hypotheses which the mathematical model is based on, and the analysis can be considered only qualitative for FCII^P.

$$\boxed{\text{FCI}^P\text{:}\quad A = 5.211 \times 10^{-5} \pm 3.5\%} \qquad \boxed{\text{FCII}^P\text{:}\quad A = 3.497 \times 10^{-4} \pm 26.7\%}$$

Further campaigns are needed to study these parameters across a wide range of wind tunnel conditions and cork materials to assess their variability. While the current model is primarily descriptive, calibrated on a limited dataset to capture the observed behaviour, its parametric structure is designed with predictive potential: with a sufficiently broad and diverse dataset, it could be extended to predict ablation across different materials and

flow conditions, providing a basis for simple and fast predictive models for the scientific community. The proposed analysis has potential for broad application in upcoming experimental campaigns, as it can be employed for configurations both with and without particles and under different atmospheric conditions (e.g., Earth). The framework can also be extended to carbon-based ablators that do not exhibit swelling, by imposing $b = 0$ and omitting the post-erosion swelling term. Ongoing studies on the DLR-developed carbon-based ablator ZURAM further support the applicability of this methodology.

6.4 Summary and Future Steps

This work provides a foundation for future parametric extensions aimed at predictive modelling of material response in high-enthalpy flow environments, including scenarios relevant to Martian atmospheric entry during dust storms. A 1D mathematical model has been proposed to describe the thickness evolution of cork-based ablators in particle-laden two-phase high-enthalpy flows, explicitly accounting for swelling, recession, particle-induced erosion, and the newly identified post-erosion swelling phenomenon. The thickness evolution is described by a constrained IVP, as defined and discussed in section 6.1, whose solution explicitly depends on the four terms related to recession, swelling, post-erosion swelling and particle-induced erosion.

Fitting against time-resolved thickness evolution data demonstrated that the model reliably reproduces experimental results within acceptable accuracy, thereby confirming the existence of post-erosion swelling. Depending on the heat flux condition, the long-term recession rate a ranges from 0.024 mm/s to 0.038 mm/s, the swelling parameter b from -2.08 mm to -1.17 mm, and the system's stiffness k from 0.015 s^{-1} to 0.030 s^{-1}. The particle-induced erosion parameter A has physical significance under the assumptions of constant and homogeneous particle velocity, constant particle and material properties, homogeneous seeding, and quasi-perpendicular impact. These conditions are satisfied only in FCI^P, where $A = 5.211 \times 10^{-5} \pm 3.5\%$. However, in $FCII^P$, particles undergo agglomeration and melting, violating the assumption of constant particle properties. In addition, the limited optical resolution of the setup introduces a large uncertainty in the measured particle count. As a result, the analysis of particle-laden cases can only be regarded as qualitative.

- Future experimental campaigns should explore a wider range of materials and operating conditions, including carbon-based ablators. The goal is to establish representative parameter sets that enable predicting how different materials respond to varying flow conditions using the model developed in this work. This approach also allows for a systematic sensitivity analysis of the model parameters with respect to flow conditions and heat flux. The strategy can be applied to both Earth and Martian atmospheric entry scenarios.

- Further developments should focus on measuring the particle mass flow rate to evaluate the link between particle momentum flux and sample erosion. This step is crucial for modelling two-phase high-enthalpy flows in Martian atmospheric entry, as it could provide experimental validation of existing numerical models. Since the current particle count measurements are not fully reliable, techniques such as PDPA and L2F could be tested to obtain more accurate particle flux data.
- Future work should investigate the possibility of extending the model to 2D or 3D.

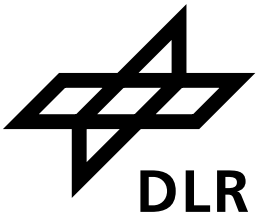
DLR

7 Conclusions and Outlook

This work focused on developing an experimental framework capable of characterising both the particle-laden flow within the L2K arc-heated wind tunnel, and the material behaviour under flow conditions used to simulate Martian entry during dust storms, in ground testing facilities. In the first place, several relevant particle-laden flow conditions were studied and characterised to establish a solid experimental foundation and knowledge necessary for material characterisation tests. Then, the diagnostic capabilities of the facility were enhanced through the development of an innovative technique for in-situ thickness evolution measurements, aimed to precisely determine the material response under the previously-characterised conditions. This effort ultimately resulted in the collection of unique experimental data on particle-laden high-enthalpy flows and in the development of a mathematical model for predicting material behaviour based on the experimental evidence.

The Martian "dusty" entry conditions were simulated by inserting micrometric MgO particles in the high-temperature CO_2 / N_2 flow inside the wind tunnel reservoir. Four wind tunnel flow conditions (FC) were studied, namely the low-/high-enthalpy ones (I/II) and the ones with/without particles ($^{P/nP}$), as reported in chapter 3. Two different experimental setups were used, one for undisturbed free-stream analysis (FS) and one with a cork probe inserted in the flow field for shock-layer analysis (SL).

With the aim of characterising the particle and flow velocities, PIV and TDLAS were respectively applied and compared. CFD simulations of the flow conditions without particles were performed. The results presented in chapter 4 highlighted peculiar high-enthalpy two-phase flow characteristics, such as a significant velocity lag between flow and particles, particle agglomeration favoured by melting ("agglo-melting"), and gravitational effect. Several particle flow-field features were observed, such as a steep velocity gradient between the free-stream and the shock layer, and a counterflow due to particle rebounding and probe outgassing. Particles were collected and analysed with SEM microscopy and EDX.

The behaviour of cork-based ablators was analysed in chapter 5 for the characterised flow conditions, by means of IR thermography (two-colour pyrometer, one-colour pyrometer and IR camera), embedded thermocouples, video monitoring, X-rays, and thickness evolution measurements such as 3D surface scans and LPT—a newly developed technique for in-situ evolution measurements. In this work, the term *thickness evolution*, or *evolution*, refers to the combined effect of probe ablation and swelling. The SL setup was

used for this analysis. Particle-induced effects were observed on the material response, such as recession and heat transfer enhancement. Peculiar effects on thermography data were observed and discussed, such as rapid drops of surface temperature due to erosion events, and emissivity discrepancies, that cause mismatches between different measurement techniques.

Finally, a 1D mathematical model based on experimental evidence was developed in chapter 6, to efficiently describe the sample thickness evolution. The model accounts for swelling, a constant long-term recession rate, particle-induced erosion, and post-erosion swelling—a phenomenon never described previously. Good agreement with experimental data was achieved, providing a solid foundation for future experimental campaigns aimed at building a database for predictive applications. The approach is flexible with respect to flow conditions (including different atmospheres, such as those of Earth and Mars) and material types, extending even to carbon-based ablators that do not exhibit swelling. Ongoing investigations on the DLR-developed carbon-based ablator ZURAM further confirm the feasibility of this methodology.

This study presents a comprehensive analysis conducted in an arc-heated wind tunnel for TPS testing under conditions representative of the Martian environment, demonstrating the efficiency and reliability of the experimental design while paving the way for future investigations into the complex interactions between particle-laden high-enthalpy flows and thermal protection systems. Ultimately, such advancements bring us one step closer to ensuring the success and safety of the next generation of Martian entry missions, bridging today's laboratory experiments with tomorrow's journeys across the Red Planet.

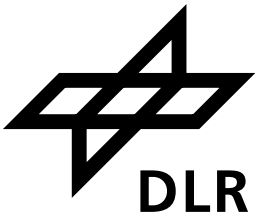
DLR

8 Bibliography

[1] Aissa, A., M. Abdelouahab, A. Noureddine, M. E. Ganaoui, and B. Pateyron, "Ranz and Marshall Correlations Limits on Heat Flow Between a Sphere and its Surrounding Gas at High Temperature", *Thermal Science*, vol. 19, no. 5, pp. 1521–1528, 2015. DOI: 10.2298/TSCI120912090A

[2] Alkhimov, A. P., N. I. Nesterovich, and A. N. Papyrin, "Experimental investigation of supersonic two-phase flow over bodies", *Journal of Applied Mechanics and Technical Physics*, vol. 23, pp. 219–226, 1982. DOI: 10.1007/BF00911002

[3] Allofs, D., "Experimental Investigation of Particle-Induced Heating Augmentation in Supersonic Flows", Ph.D. thesis, DLR – RWTH University, Köln, Germany, 2024. DOI: 10.57676/r2e9-w211

[4] Allofs, D., D. Neeb, and A. Gülhan, "Simultaneous determination of particle size, velocity, and mass flow in dust-laden supersonic flows", *Experiments in Fluids*, vol. 63, no. 64, 2022. DOI: 10.1007/s00348-022-03402-z

[5] Allofs, D., D. Neeb, and A. Gülhan, "Experimental investigation of heating augmentation by particle kinetic energy conversion in dust-laden supersonic flows", *Experiments in Fluids*, vol. 64, no. 179, 2023. DOI: 10.1007/s00348-023-03718-4

[6] Allofs, D., D. Neeb, and A. Gülhan, "Particle mass flow determination in dust-laden supersonic flows by means of simultaneous application of optical measurement techniques", *Experiments in Fluids*, vol. 64, no. 49, 2023. DOI: 10.1007/s00348-022-03567-7

[7] Amorim, *Amorim Cork Solutions*. Accessed: Feb. 27, 2026. [Online]. Available: https://amorimcorksolutions.com/en-us/

[8] Bade, W. L. and J. M. Yos, "The NATA Code – Theory and Analysis", NASA, Technical Report CR-2547, 1975.

[9] Bailet, G., A. Denis, A. Bourgoing, C. O. Laux, and T. E. Magin, "Nonintrusive Instrument for Thermal Protection System to Measure Recession and Swelling", *Journal of Spacecraft and Rockets*, vol. 59, no. 1, pp. 6–18, 2022. DOI: 10.2514/1.A34968

[10] Bakum, B. I. and G. S. Komarova, "The effect of dust in the working stream of hypersonic wind tunnels on the results of heat-transfer measurements", *Journal of Engineering Physics*, vol. 21, pp. 1361–1363, 1971. DOI: 10.1007/BF01271345

[11] Balachandar, S. and J. K. Eaton, "Turbulent Dispersed Multiphase Flow", *Annual Review of Fluid Mechanics*, vol. 42, pp. 111–133, 2010. DOI: 10.1146/annurev.fluid.010908.165243

[12] Ball, A. J., T. Blancquaert, O. Bayle, L. V. Lorenzoni, A. F. Haldemann, and Schiaparelli EDM Team, "The ExoMars Schiaparelli Entry, Descent and Landing Demonstrator Module (EDM) System Design", *Space Science Reviews*, vol. 218, no. 44, 2022. DOI: 10.1007/s11214-022-00898-z

[13] Beck, R. A. S., "Ablative Thermal Protection System Fundamentals", in *IPPW*, San Jose, California, 15–21 Jun., 2013. Accessed: Feb. 27, 2026. [Online]. Available: https://ntrs.nasa.gov/citations/20140000874

[14] Beck, R. A. S., D. M. Driver, M. J. Wright, H. H. Hwang, K. T. Edquist, and S. A. Sepka, "Development of the Mars Science Laboratory Heatshield Thermal Protection System", *Journal of Spacecraft and Rockets*, vol. 51, no. 4, pp. 1139–1150, 2014. DOI: 10.2514/1.A32635

[15] Ben-Dor, G., "Dusty shock waves – an update", *Applied Mechanics Review*, vol. 49, no. 10S, S141–S146, 1996. DOI: 10.1115/1.3101965

[16] Bird, G. A., *Molecular Gas Dynamics and the Direct Simulation of Gas Flows*. Oxford, UK: Oxford University Press, 1994, ISBN: 9781383028911. DOI: 10.1093/oso/9780198561958.001.0001

[17] Boubert, P. and C. Rond, "Nonequilibrium Radiation in Shocked Martian Mixtures", *Journal of Thermophysics and Heat Transfer*, vol. 24, no. 1, pp. 40–49, 2010. DOI: 10.2514/1.45385

[18] Brandt, L. and F. Coletti, "Particle-Laden Turbulence: Progress and Perspectives", *Annual Review of Fluid Mechanics*, vol. 54, pp. 159–189, 2022. DOI: 10.1146/annurev-fluid-030121-021103

[19] Buntrock, L. J., M. Grabe, and H. Fischer, "Contamination assessment of a freely expanding green propellant thruster plume", *IOP Conf. Series: Materials Science and Engineering*, vol. 1287, no. 012044, 2023. DOI: 10.1088/1757-899X/1287/1/012004

[20] Capecelatro, J., "Modeling high-speed gas–particle flows relevant to spacecraft landings", *International Journal of Multiphase Flow*, vol. 150, no. 104008, 2022. DOI: 10.1016/j.ijmultiphaseflow.2022.104008

[21] Capecelatro, J. and J. L. Wagner, "Gas–Particle Dynamics in High-Speed Flows", *Annual Review of Fluid Mechanics*, vol. 56, pp. 379–403, 2024. DOI: 10.1146/annurev-fluid-121021-015818

[22] Capitelli, M., G. Colonna, D. Giordano, L. Marraffa, A. Casavola, P. Minelli, D. Pagano, L. D. Pietanza, and F. Taccogna, "Tables of Internal Partition Functions and Thermodynamic Properties of High-Temperature Mars-Atmosphere Species from 50 K to 50000 K", European Space Agency, Technical Report ESA STR 246, 2005.

[23] Cioeta, M., G. Di Vita, T. Signorelli Maria, G. Bianco, M. Cutroni, F. Damiani, V. Ferretti, and A. Rotondo, "Design, qualification, manufacturing and integration of IXV ablative thermal protection system", *Acta Astronautica*, vol. 124, pp. 90–101, 2016. DOI: 10.1016/j.actaastro.2015.12.026

[24] Cox, J. A., "Evaluation Of Peak Location Algorithms With Subpixel Accuracy For Mosaic Focal Planes", in *Processing of Images and Data from Optical Sensors*, vol. 0292, 1981, pp. 288–299. DOI: 10.1117/12.932843

[25] Crowe, C. T., T. R. Troutt, and J. N. Chung, "Numerical models for two-phase turbulent flows", *Annual Review of Fluid Mechanics*, vol. 28, pp. 11–43, 1996. DOI: 10.1146/annurev.fl.28.010196.000303

[26] Davis, B. A., E. L. Christiansen, D. M. Lear, and T. Prior, "International Space Station (ISS) Soyuz Vehicle Descent Module Evaluation of Thermal Protection System (TPS) Penetration Characteristics", NASA Lyndon B. Johnson Space Center, Houston, Texas, Technical Report NASA JSC-66527, 2013.

[27] DLR and ESA, "Experimental and Theoretical Study of Mars Dust Effects, Heat Transfer Measurement Report", Supersonic and Hypersonic Technologies Department, DLR, Köln, Report MDUST-DLR-TN-032, 2006.

[28] Dominik, S. R., "Development of a Thermal Ablation Model with Experimental Validation in an Arc-Heated Wind Tunnel", Master's Thesis, RWTH Aachen, DLR, 2023.

[29] Dong, Y. and B. Pan, "In-situ 3D shape and recession measurements of ablative materials in an arc-heated wind tunnel by UV stereo-digital image correlation", *Optics and Lasers in Engineering*, vol. 116, pp. 75–81, 2019. DOI: 10.1016/j.optlaseng.2018.10.022

[30] Driver, D. M., M. W. Olson, M. D. Bernhardt, and M. MacLean, "Understanding High Recession Rates of Carbon Ablators Seen in Shear Tests in an Arc Jet", in *48th AIAA Aerospace Sciences Meeting*, Orlando, Florida, 4–7 Jan., 2010. DOI: 10.2514/6.2010-1177

[31] Dubois, J., "CFD Validation in CO_2 Environment – Review of CO_2 Modelling and Recommendations for Improvement through Experiment", Fluid Gravity Engineering Ltd, Technical Report CR055/06, 2006.

[32] Dunbar, L. E., J. F. Courtney, and L. D. Mcmillen, "Heating augmentation in erosive hypersonic environments", *AIAA Journal*, vol. 13, no. 7, pp. 908–912, 1975. DOI: 10.2514/3.60468

[33] Elghobashi, S., "On predicting particle-laden turbulent flows", *Applied Scientific Research*, vol. 52, pp. 309–329, 1994. DOI: 10.1007/BF00936835

[34] ESA, *Heat shields for the Schiaparelli capsule*. Accessed: Feb. 27, 2026. [Online]. Available: https://exploration.esa.int/web/mars/-/54509-heat-shields-for-the-schiaparelli-capsule

[35] Farbar, E., H. Alkandry, J. Wiebenga, and I. D. Boyd, "Simulation of Ablating Hypersonic Vehicles with Finite-Rate Surface Chemistry", in *11th AIAA/ASME Joint Thermophysics and Heat Transfer Conference*, Atlanta, Georgia, 16–20 Jun., 2014. DOI: 10.2514/6.2014-2124

[36] Farbar, E., I. D. Boyd, and A. Martin, "Modeling Ablation of Charring Heat Shield Materials For Non-Continuum Hypersonic Flow", in *50th AIAA Aerospace Sciences Meeting*, Nashville, Tennessee, 9–12 Jan., 2012. DOI: 10.2514/6.2012-532

[37] Fleener, W. and R. Watson, "Convective heating in dust-laden hypersonic flows", in *8th Thermophysics Conference*, Palm Springs, California, 16–18 Jul., 1973. DOI: 10.2514/6.1973-761

[38] Glass, D. E., "Ceramic Matrix Composite (CMC) Thermal Protection Systems (TPS) and Hot Structures for Hypersonic Vehicles", in *15th AIAA Space Planes and Hypersonic Systems and Technologies Conference*, Dayton, Ohio, 28 Apr.–1 May, 2008. DOI: 10.2514/6.2008-2682

[39] Gnemmi, P., C. Rey, J. Srulijes, F. Seiler, and J. Haertig, "Hypersonic Flow-Field Measurements by PIV", in *14th International Symposium on Flow Visualization*, Daegu, Korea, 21–24 Jun., 2010. DOI: 10.13140/2.1.4919.9041

[40] Gökcen, T., "N_2–CH_4–Ar Chemical Kinetic Model for Simulations of Atmospheric Entry to Titan", *Journal of Thermophysics and Heat Transfer*, vol. 21, no. 1, pp. 9–18, 2007. DOI: 10.2514/1.22095

[41] Gülhan, A., T. Thiele, F. Siebe, R. Kronen, and T. Schleutker, "Aerothermal Measurements from the ExoMars Schiaparelli", *Journal of Spacecrafts ad Rockets*, vol. 56, no. 1, pp. 68–81, 2019. DOI: 10.2514/1.A34228

[42] Haw, M., "Measurement of material recession and shock standoff in plasma wind tunnel using neural nets", in *APS Division of Plasma Physics Annual Meeting*, Virtual meeting, 2020. Accessed: Feb. 27, 2026. [Online]. Available: https://ntrs.nasa.gov/citations/20205009236

[43] Haynes, W. M., *CRC Handbook of Chemistry and Physics (92nd ed.)* Boca Raton: CRC Press, 2011, ISBN: 9781439855119.

[44] Helber, B., A. Turchi, J. B. Scoggins, A. Hubin, and T. E. Magin, "Experimental investigation of ablation and pyrolysis processes of carbon-phenolic ablators in atmospheric entry plasmas", *International Journal of Heat and Mass Transfer*, vol. 100, pp. 810–824, 2016. DOI: 10.1016/j.ijheatmasstransfer.2016.04.072

[45] Holden, M., G. Duryea, G. Gustafson, and L. Hudack, "An experimental study of particle-induced convective heating augmentation", in *9th Fluid and Plasma Dynamics Conference*, San Diego, California, 14–16 Jul., 1976. DOI: 10.2514/6.1976-320

[46] Hufnagel, M., S. Staudacher, and C. Koch, "Experimental and Numerical Investigation of the Mechanical and Aerodynamic Particle Size Effect in High-Speed Erosive Flows", *Journal of Engineering for Gas Turbines and Power*, vol. 140, no. 102604, 2018. DOI: 10.1115/1.4039830

[47] Hufnagel, M., C. Werner-Spatz, C. Koch, and S. Staudacher, "High-Speed Shadowgraphy Measurements of an Erosive Particle-Laden Jet Under High-Pressure Compressor Conditions", *Journal of Engineering for Gas Turbines and Power*, vol. 140, no. 012604, 2018. DOI: 10.1115/1.4037689

[48] Igra, O. and G. Ben-Dor, "Dusty shock waves", *Applied Mechanics Review*, vol. 41, no. 11, pp. 379–437, 1988. DOI: 10.1115/1.3151872

[49] Ivanov, M., G. Markelov, D. Levin, and S. Gimelshein, "Modeling of Rarefied Hypersonic Flows Over Spacecraft in Martian Atmosphere Using the DSMC Method", in *8th AIAA/ASME Joint Thermophysics and Heat Transfer Conference*, St. Louis, Missouri, 24–26 Jun., 2002. DOI: 10.2514/6.2002-2759

[50] Johnson, S. M., "Thermal Protection Materials: Development, Characterization and Evaluation", in *HiTemp Conference*, Munich, Germany, 11–13 Sep., 2012. Accessed: Feb. 27, 2026. [Online]. Available: https://ntrs.nasa.gov/citations/20120016878

[51] Johnston, C. O., P. A. Gnoffo, and A. Mazaheri, "Study of Ablation-Flowfield Coupling Relevant to the Orion Heatshield", *AIAA Journal of Thermophysics and Heat Transfer*, vol. 26, no. 2, pp. 213–221, 2012. DOI: 10.2514/1.T3769

[52] Karlgaard, C. D., A. M. Korzun, M. Schoenenberge, E. P. Bonfiglio, D. M. Kass, and M. R. Grover, "Mars InSight Entry, Descent, and Landing Trajectory and Atmosphere Reconstruction", *Journal of Spacecraft and Rockets*, vol. 58, no. 3, pp. 865–878, 2021. DOI: 10.2514/1.A34913

[53] Keller, K., P. Lindenmaier, E. K. Pfeiffer, B. Esser, A. Gülhan, P. Omaly, and M. Desjean, "Dust Particle Erosion during Mars Entry", in *40th International Conference on Environmental Systems*, Barcelona, Spain, 11–15 Jul., 2010. DOI: 10.2514/6.2010-6283

[54] Kemp, N. H., P. H. Rose, and R. W. Detra, "Laminar Heat Transfer Around Blunt Bodies in Dissociated Air", *Aerospace Sciences*, vol. 26, no. 7, pp. 421–430, 1959. DOI: 10.2514/8.8128

[55] Kessel, P. A., "Rocket Exhaust Probe", US Patent 4,662,216, 1987.

[56] Keyence, *Keyence 3D-Profilometer VR-5000*. Accessed: Feb. 27, 2026. [Online]. Available: https://www.keyence.de/landing/lpc/3d-profilometer-vr.jsp

[57] Kirmse, T., J. Agocs, A. S. J., M. Schramm, S. Karl, and K. Hannemann, "Application of particle image velocimetry and the background-oriented schlieren technique in the high-enthalpy shock tunnel Göttingen", *Shock Waves*, vol. 21, pp. 233–241, 2011. DOI: 10.1007/s00193-011-0314-2

[58] Kudin, O. K., Y. N. Nesterov, O. D. Tokarev, and Y. S. Flaksman, "Experimental investigations of a high-temperature dust-laden gas jet impinging on an obstacle", *TsAGI Science Journal*, vol. 44, no. 6, pp. 869–884, 2013. DOI: 10.1615/TsAGISciJ.2014011135

[59] Lachaud, J., T. v. Eekelen, J. B. Scoggins, T. E. Magin, and N. N. Mansour, "Detailed chemical equilibrium model for porous ablative materials", *International Journal of Heat and Mass Transfer*, vol. 90, pp. 1034–1045, 2015. DOI: 10.1016/j.ijheatmasstransfer.2015.05.106

[60] Langton, M. and A. Hermansson, "Image analysis determination of particle size distribution", *Food Hydrocolloids*, vol. 7, no. 1, pp. 11–22, 1973. DOI: 10.1016/S0268-005X(09)80021-0

[61] LaVision, *DaVis*. Accessed: Feb. 27, 2026. [Online]. Available: https://www.lavision.de/en/products/davis-software/

[62] Lee, G. S., P. Sakkos, I. Gessman, J. Lim, N. Kato, B. M. Kirchner, G. Elliott, and T. Lee, "PIV Measurements and Total Temperature Thermometry of a Mach 4.5 Arc-heated Nozzle Flow", in *AIAA SciTech Forum*, San Diego, California, 3–7 Jan., 2022. DOI: 10.2514/6.2022-2337

[63] Lemmon, M. T., M. J. Wolff, M. D. Smith, R. T. Clancy, D. Banfield, G. A. Landis, A. Ghosh, P. H. Smith, N. Spanovich, B. Whitney, P. Whelley, R. Greeley, S. Thompson, J. F. Bell III, and S. W. Squyres, "Atmospheric Imaging Results from the Mars Exploration Rovers: Spirit and Opportunity", *Science*, vol. 306, no. 5702, pp. 1753–1756, 2004. DOI: 10.1126/science.1104474

[64] Levin, A. L., "Heat exchange near the critical point of a body within a supersonic two-phase jet", *Journal of Applied Mechanics and Technical Physics*, vol. 34, pp. 694–700, 1993. DOI: 10.1007/BF00859837

[65] Löhle, S. and T. Riehmer, "Experimental Investigation of Photogrammetric Surface Analysis of Heat Shield Materials during Plasma Wind Tunnel Testing", in *7th European Workshop on Thermal Protection Systems and Hot Structures*, Noordwijk, Netherlands, 8–10 Apr., 2013. Accessed: Feb. 27, 2026. [Online]. Available: https://elib.dlr.de/87097/

[66] Lorenz, G. C., "Simulation of the Erosive Effects of Multiple Particle Impacts in Hypersonic Flow", *Journal of Spacecraft*, vol. 7, no. 2, pp. 119–125, 1970. DOI: 10.2514/3.29885

[67] Lu, J., H. Yang, Q. Zhang, and Z. Yin, "PIV measurements of hypersonic laminar flow over a compression ramp", in *13th International Symposium on Particle Image Velocimetry*, Munich, Germany, 22–24 Jul., 2019. Accessed: Feb. 27, 2026. [Online]. Available: https://athene-forschung.unibw.de/128813

[68] Mahzari, M., R. D. Braun, T. R. White, and D. Bose, "Inverse Estimation of the Mars Science Laboratory Entry Aeroheating and Heatshield Response", *Journal of Spacecraft and Rockets*, vol. 52, no. 4, pp. 1203–1216, 2015. DOI: 10.2514/1.A33053

[69] Martin, A., I. D. Boyd, I. Cozmuta, and M. J. Wright, "Chemistry model for ablating carbon-phenolic material during atmospheric re-entry", in *48th AIAA Aerospace Sciences Meeting*, Orlando, Florida, 4–7 Jan., 2010. DOI: 10.2514/6.2010-1175

[70] Maurer, *Maurer Digital Infrared 2-Color Pyrometer – Series QKTRD 1485*. Accessed: Feb. 27, 2026. [Online]. Available: https://www.maurer-ir.com/produkt/universalpyrometer-qktrd-1485/

[71] Maurer, *Maurer Digital Infrared Pyrometer – Series KTRD 1485*. Accessed: Feb. 27, 2026. [Online]. Available: https://www.maurer-ir.com/produkt/universalpyrometer-ktrd-1485/

[72] Mazzaracchio, A., "One-Dimensional Thermal Analysis Model for Charring Ablative Materials", *Journal of Aerospace Technologies and Management*, vol. 10, no. e0418, 2018. DOI: 10.5028/jatm.v10.965

[73] Milos, F. S., Y. K. Chen, W. M. Congdon, and J. M. Thornton, "Mars Pathfinder Entry Temperature Data, Aerothermal Heating, and Heatshield Material Response", *Journal of Spacecraft and Rockets*, vol. 36, no. 3, pp. 380–391, 1999. DOI: 10.2514/2.3457

[74] Milos, F. S. and Y. Chen, "Ablation and Thermal Response Property Model Validation for Phenolic Impregnated Carbon Ablator", *Journal of Spacecraft and Rockets*, vol. 47, no. 5, pp. 786–805, 2010. DOI: 10.2514/1.42949

[75] Ming, D. W. and R. V. Morris, "Chemical, Mineralogical, and Physical Properties of Martian Dust and Soil", in *Dust in the Atmosphere of Mars and Its Impact on Human Exploration*, Levine, J. S., Ed., University of Cambridge, UK: Cambridge Scholars Publishing, 2017, pp. 31–48, ISBN: 9781527511729.

[76] Mitcheltree, R. A., J. N. Moss, F. M. Cheatwood, F. A. Greene, and R. D. Braun, "Aerodynamics of the Mars Microprobe Entry Vehicles", *Journal of Spacecraft and Rockets*, vol. 36, no. 3, pp. 392–398, 1999. DOI: 10.2514/2.3458

[77] NASA and Aeronautics Research Mission Directorate, *Space Shuttle Tiles*. Accessed: Feb. 27, 2026. [Online]. Available: https://www.nasa.gov/wp-content/uploads/2023/06/shuttle-tiles-9-12v2.pdf

[78] Neeb, D., D. Saile, and A. Gülhan, "Experiments on a smooth wall hypersonic boundary layer at Mach 6", *Experiments in Fluids*, vol. 59, no. 68, 2018. DOI: 10.1007/s00348-018-2518-z

[79] Oka, Y. I., K. Okamura, and T. Yoshida, "Practical estimation of erosion damage caused by solid particle impact. Part 1: Effects of impact parameters on a predictive equation", *Wear*, vol. 259, no. 1, pp. 95–101, 2005. DOI: 10.1016/j.wear.2005.01.039

[80] Oka, Y. I. and T. Yoshida, "Practical estimation of erosion damage caused by solid particle impact. Part 2: Mechanical properties of materials directly associated with erosion damage", *Wear*, vol. 259, no. 1, pp. 102–109, 2005. DOI: 10.1016/j.wear.2005.01.040

[81] Optris, *PI 1M – Optris (EU)*. Accessed: Feb. 27, 2026. [Online]. Available: https://optris.com/products/infrared-cameras/precision-line/pi-1m/

[82] Osipov, M. I., K. A. Gladoshchuk, and A. N. Arbekov, "Heat transfer processes in high-temperature flows of two-phase media", *Heat Transfer Research*, vol. 32, no. 7-8, pp. 402–408, 2001. DOI: 10.1615/HeatTransRes.v32.i7-8.90

[83] Pagan, A. S., B. Massuti-Ballester, T. Mayer, G. Herdrich, S. Fasoulas, R. Ogawa, Y. Kubota, K. Yasuo, and H. Hatta, "Laser-based surface recession measurements of ablating heat shield materials in high-enthalpy flows", in *8th European Symposium on Aerothermodynamics for Space Vehicles*, Lisbon, Portugal, 2–6 Mar., 2015. Accessed: Feb. 27, 2026. [Online]. Available: https://www.researchgate.net/publication/280085105

[84] Palmer, G., E. Ching, M. Ihme, D. Allofs, and A. Gülhan, "Modeling Heat-Shield Erosion due to Dust Particle Impacts for Martian Entries", *Journal of Spacecraft and Rockets*, vol. 57, no. 5, pp. 857–875, 2020. DOI: 10.2514/1.A34744

[85] Palmer, G., A. Sahai, D. Allofs, and A. Gülhan, "Comparing Particle Flow Regimes in the L2K Arcjet with Martian Entry Conditions", in *2nd International Conference on Flight Vehicles, Aerothermodynamics and Re-entry Missions and Engineering*, Heilbronn, Germany, 19–23 Jun., 2022. Accessed: Feb. 27, 2026. [Online]. Available: https://ntrs.nasa.gov/citations/20220007187

[86] Papadopoulos, P., M. E. Tauber, and I. Chang, "Heatshield erosion in a dusty Martian atmosphere", *Journal of Spacecraft and Rockets*, vol. 30, no. 2, pp. 140–151, 1993. DOI: 10.2514/3.11522

[87] Park, C., J. T. Howe, R. L. Jaffe, and G. V. Candler, "Review of Chemical-Kinetic Problems of Future NASA Missions, II: Mars Entries", *Journal of Thermophysics and Heat Transfer*, vol. 8, no. 1, pp. 9–23, 1994. DOI: 10.2514/3.496

[88] Park, C., R. L. Jaffe, and H. Partridge, "Chemical-Kinetic Parameters of Hyperbolic Earth Entry", *Journal of Thermophysics and Heat Transfer*, vol. 15, no. 1, pp. 76–90, 2001. DOI: 10.2514/2.6582

[89] Pavlosky, J. E. and L. G. S. Leger, "Apollo experience report – thermal protection subsystem", NASA Lyndon B. Johnson Space Center, Houston, Texas, Technical Note NASA TN D-7564, 1974.

[90] Pinaud, G. and A. Gülhan, "ABLAMOD: Advanced Ablation Characterization and Modelling European Project Description", in *6th Ablation Workshop*, Champaign, Illinois, 10–11 Apr., 2014. Accessed: Feb. 27, 2026. [Online]. Available: https://uknowledge.uky.edu/ablation/2014/Modeling/1/

[91] Polezhaev, Y. V., "Stabilization of the erosion process affecting the material of a barrier under repetitive impact by particles", *Journal of Engineering Physics, translated from Inzhenerno-Fizicheskii Zhurnal*, vol. 37, pp. 1007–1011, 1979. DOI: 10.1007/BF00861670

[92] Polezhaev, Y. V. and V. I. Panchenko, "Fundamental relations of erosion kinetics", *Journal of Engineering Physics*, vol. 52, pp. 507–512, 1987. DOI: 10.1007/BF00873301

[93] Polezhaev, Y. V., I. V. Repin, and D. S. Mikhatulin, "Heat transfer in a heterogeneous supersonic flow", *Teplofizika Vysokikh Temperatur*, vol. 30, pp. 1147–1153, 1992.

[94] Price, K., S. Bailey, and A. Martin, "Characterization and Modeling of Spallation in Thermal Protection Systems", in *11th International Conference on Computational Fluid Dynamics*, Maui, Hawaii, 11–15 Jul., 2022. Accessed: Feb. 27, 2026. [Online]. Available: https://www.iccfd.org/iccfd11/assets/pdf/papers/ICCFD11_Paper-3203.pdf

[95] Raffel, M., C. E. Willert, F. Scarano, C. J. Kähler, S. T. Wereley, and J. Kompenhans, *Particle Image Velocimetry – A Practical Guide, Third Edition*. Cham, Switzerland: Springer International Publishing AG, 2018, ISBN: 9783319688527. DOI: 10.1007/978-3-319-68852-7

[96] Reimer, T., C. Zuber, J. Rieser, and T. Rothermel, "Determination of the Mechanical Properties of the Lightweight Ablative Material Zuram", in *Processing, Properties, and Design of Advanced Ceramics and Composites II: Ceramic Transactions*, Bansal, N. P., R. H. Castro, M. Jenkins, A. Bandyopadhyay, S. Bose, A. Bhalla, J. P. Singh, M. M. Mahmoud, G. Pickrell, and S. Johnson, Eds., The American Ceramic Society: Cambridge Scholars Publishing, 2017, ch. 28, pp. 311–326, ISBN: 9781119423805. DOI: 10.1002/9781119423829.ch28

[97] Renato, V., C. White, and T. Scanlon, "ABLAMOD: Advanced Ablation Characterization and Modelling", DLR, Strathclyde University, Technical Report D54.1, D55.1, 2015.

[98] Rivier, M., J. Lachaud, and P. Congedo, "Ablative thermal protection system under uncertainties including pyrolysis gas composition", *Aerospace Science and Technology*, vol. 84, pp. 1059–1069, 2019. DOI: 10.1016/j.ast.2018.11.048

[99] Sahai, A. and G. Palmer, "Dust Particle Aeroheating Calculations for Mars Entry Hypersonic Flows", in *18th IPPW*, Glasgow, England, 8 Jul., 2021. Accessed: Feb. 27, 2026. [Online]. Available: https://ntrs.nasa.gov/citations/20210018073

[100] Saile, D., D. Allofs, V. Kühl, J. Riehmer, L. Steffens, A. Gülhan, M. Beversdorff, W. Förster, C. Willert, S. Carlotti, F. Maggi, M. Liljedahl, and N. Wingbor, "Experimental Modeling of Alumina Particulate in Solid Booster: Final Report", DLR, Department of Supersonic and Hypersonic Technologies, Köln, DE, Report ESA Contract No. 4000114698/15/NL/SFe, 2020.

[101] Sakraker, I., O. Chazot, and J. P. Carvalho, "Performance of cork-based thermal protection material P50 exposed to air plasma", *CEAS Space Journal*, vol. 15, pp. 377–393, 2022. DOI: 10.1007/s12567-021-00395-z

[102] Salvi, C., "Optisches Oberflächenmesssystem zur Oberflächenmessung eines Objekts in einem Windkanal sowie Windkanal mit einem optischen Oberflächenmesssystem und Verfahren zur optischen Oberflächenmessung eines Objekts in einem Windkanal", Deutsches Patent- und Markenamt, 202503271042546 2DE, 27 Mar. 2025.

[103] Salvi, C. and A. Gülhan, "Velocity measurements in particle-laden high-enthalpy flow using non-intrusive techniques", *Experiments in Fluids*, vol. 65, no. 39, 2024. DOI: 10.1007/s00348-024-03776-2

[104] Salvi, C. and A. Gülhan, "PIV in the vicinity of cork samples in particle-laden high-enthalpy flow", *Experiments in Fluids*, vol. 66, no. 160, 2025. DOI: 10.1007/s00348-025-04083-0

[105] Salvi, C. and A. Gülhan, "Particle image velocimetry on cork samples in arc-heated wind tunnels", in *11th EUCASS*, Roma, Italy, 30 Jun.–4 Jul. 2025. Accessed: Feb. 27, 2026. [Online]. Available: https://elib.dlr.de/213998/

[106] Salvi, C. and A. Gülhan, "Recession measurements of cork samples in particle-laden arc-heated wind tunnel", in *IPPW*, Stuttgart, Germany, 23–27 Jun. 2025. Accessed: Feb. 27, 2026. [Online]. Available: https://elib.dlr.de/214000/

[107] Salvi, C. and O. H. A. Gülhan, "Particle-laden flow characterization in high enthalpy ground testing facilities", in *Understanding the Atmospheric Effects of Re-entry (Workshop)*, ESTEC, Noordwijk, Netherlands, 10–11 Jan. 2024. Accessed: Feb. 27, 2026. [Online]. Available: https://elib.dlr.de/201094/

[108] Salvi, C., O. Hohn, and A. Gülhan, "1D thickness evolution model of cork ablators, including swelling, ablation and erosion", *International Journal of Heat and Mass Transfer*, vol. 256, no. 128033, 2026. DOI: 10.1016/j.ijheatmasstransfer.2025.128033

[109] Salvi, C., O. Hohn, and A. Gülhan, "Characterization of ablator recession and thermal response using non-intrusive techniques", *AIAA Journal*, vol. 64, no. 6, pp. 3127–3138, 2026. DOI: 10.2514/1.J065731

[110] Salvi, C., L. Steffens, O. Hohn, A. Gülhan, and F. Maggi, "Martian flow characterization using tunable diode laser absorption spectroscopy, in high enthalpy facilities", *Acta Astronautica*, vol. 213, pp. 204–214, 2023. DOI: 10.1016/j.actaastro.2023.08.043

[111] Santos, A. P., L. J. Abbott, and J. B. Haskins, "Fracture of Charring Avcoat With Meshfree Material Response-Coupled Fracture Approach", in *13th Ablation Workshop*, Mountain View, California, 7–9 Nov., 2023. Accessed: Feb. 27, 2026. [Online]. Available: https://ntrs.nasa.gov/citations/20230013745

[112] SBIR-STTR, *Nonintrusive fiber interferometer for ablative TPS recession measurement*. Accessed: Feb. 27, 2026. [Online]. Available: https://www.sbir.gov/awards/133939

[113] Schairer, E. T. and J. T. Heineck, "Photogrammetric recession measurements of ablative materials in arcjets", *Measurement Science and Technology*, vol. 21, no. 2: 025304, 2010. DOI: 10.1088/0957-0233/21/2/025304

[114] Schneiderbauer, S., "Continuum modeling of gas–particle flows: an overview", *Acta Mechanica*, vol. 235, pp. 6959–7001, 2024. DOI: 10.1007/s00707-024-04104-9

[115] Schrijer, F. F. J., F. Scarano, and B. W. v. Oudheusden, "Application of PIV in a Mach 7 double-ramp flow", *Experiments in Fluids*, vol. 41, pp. 353–363, 2006. DOI: 10.1007/s00348-006-0140-y

[116] Stackpole, M., D. Kao, V. Qu, and G. Gonzales, "Post-Flight Evaluation of PICA and PICA-X – Comparisons of the Stardust SRC and Space-X Dragon 1 Forebody Heatshield Materials", in *IPPW*, San Jose, California, 18–21 Jun., 2013. Accessed: Feb. 27, 2026. [Online]. Available: https://ntrs.nasa.gov/citations/20140005558

[117] Stern, E. and M. Mahzari, "Dragonfly TPS Sizing and Analysis", in *AIAA SciTech*, National Harbor, Maryland, 23–27 Jan., 2023. DOI: 10.2514/6.2023-0603

[118] Thompson, K. B., C. O. Johnston, B. Kleb, A. Mazaheri, T. K. West, and W. A. Wood, "LAURA Users Manual: 5.7", NASA Langley, Hampton, Technical Report TM-2020-220566, 2024.

[119] Uyanna, O. and H. Najafi, "Thermal protection systems for space vehicles: A review on technology development, current challenges and future prospects", *Acta Astronautica*, vol. 176, pp. 341–356, 2020. DOI: 10.1016/j.actaastro.2020.06.047

[120] Vandaele, A. C. et al., "Composition and Chemistry of the Martian Atmosphere as Observed by Mars Express and ExoMars Trace Gas Orbiter", *Space Science Reviews*, vol. 220, no. 75, 2024. DOI: 10.1007/s11214-024-01109-7

[121] Varaksin, A. Y. and S. V. Ryzhkov, "Mathematical Modeling of Gas–Solid Two-Phase Flows: Problems, Achievements and Perspectives (A Review)", *Mathematics*, vol. 11, no. 15: 3290, 2023. DOI: 10.3390/math11153290

[122] Varaksin, A. Y. and S. V. Ryzhkov, "Particle-Laden and Droplet-Laden Two-Phase Flows Past Bodies (a Review)", *Symmetry*, vol. 15, no. 2: 388, 2023. DOI: 10.3390/sym15020388

[123] Vaughan, D., H. Miller, B. Griffin, B. James, and M. Munk, "A Comparative Study of Aerocapture Missions with a Mars Destination", in *41st Joint Propulsion conference and Exhibit*, Tucson, Arizona, 10–13 Jul., 2005. DOI: 10.2514/6.2005-4110

[124] Wang, S., Y. Wang, Q. Ramasse, and Z. Fan, "The Nature of Native MgO in Mg and Its Alloys", *Metallurgical and Materials Transactions A*, vol. 51, pp. 2957–2974, 2020. DOI: 10.1007/s11661-020-05740-1

[125] Weng, H. and A. Martin, "Numerical Investigation of Pyrolysis Gas Blowing Pattern and Thermal Response using Orthotropic Charring Ablative Material", in *11th AIAA/ASME Joint Thermophysics and Heat Transfer Conference*, Atlanta, Georgia, 16–20 Jun., 2014. DOI: 10.2514/6.2014-2121

[126] Williams, D. R., *Chronology of Mars Exploration*. Accessed: Jan. 1, 2025. [Online]. Available: https://nssdc.gsfc.nasa.gov/planetary/chronology_mars.html

[127] Wright, M., K. Edquist, C. Tang, B. Hollis, P. Krasa, and C. Campbell, "A Review of Aerothermal Modeling for Mars Entry Missions", in *48th AIAA Aerospace Sciences Meeting*, Orlando, Florida, 4–7 Jan., 2010. DOI: 10.2514/6.2010-443

[128] Zhang, G., H. D. Kim, and Y. Z. Jin, "Analysis of choked two-phase flows of gas and particle in a C-D nozzle", *Theoretical and Applied Mechanics Letters*, vol. 7, no. 6, pp. 331–338, 2017. DOI: 10.1016/j.taml.2017.11.005

[129] Zhang, J., B. John, M. Pfeiffer, F. Fei, and D.Wen, "Particle-based hybrid and multiscale methods for nonequilibrium gas flows", *Advances in Aerodynamics*, vol. 1, no. 12, 2019. DOI: 10.1186/s42774-019-0014-7

[130] Zhang, J. and Y. Shao, "A new parameterization of particle dry deposition over rough surfaces", *Atmospheric Chemistry and Physics*, vol. 14, no. 22, pp. 12 429–12 440, 2014. DOI: 10.5194/acp-14-12429-2014